

Identification of genes required for host-cell  
adhesion and antibiotic persistence of uropathogenic  
*Escherichia coli* (UPEC) via high-content screening

Présentée le 18 mars 2022

Faculté des sciences de la vie  
Unité du Prof. McKinney  
Programme doctoral en biotechnologie et génie biologique

pour l'obtention du grade de Docteur ès Sciences

par

**Thomas Marie SIMONET**

Acceptée sur proposition du jury

Prof. A. L. A. Persat, président du jury  
Prof. J. McKinney, directeur de thèse  
Prof. L. Van Melderén, rapporteuse  
Prof. A. Egli, rapporteur  
Prof. M. Blokesch, rapporteuse





« Eragon resta silencieux le temps que dura le Rimgar. Après quoi, en allant à la rivière pour se baigner, il demanda :

- Maître ?
- Oui, Eragon.
- Pourquoi dois-je endurer ce supplice ? Vous pourriez utiliser la magie pour me donner les talents que je dois acquérir, et pour façonner mon corps à la manière des arbres et des plantes.
- Je le pourrais. Mais, si je le faisais, tu ne comprendrais pas comment ce corps est devenu le tien, d'où te viennent tes capacités, ni comment les entretenir. Il n'y a pas de raccourci sur le chemin où tu marches, Eragon. »

« Eragon fit quelques pas en silence, puis dit :

- Quand on refuse de me livrer certains renseignements, je n'en suis que plus déterminé à découvrir la vérité. Je déteste rester dans l'ignorance. Pour moi, une question sans réponse est une épine dans le pied qui me torture au moindre mouvement tant que je ne l'ai pas enlevée.
- Je compatis.
- Pourquoi ?
- Parce que tu dois souffrir mille morts en permanence. La vie est un océan de questions sans réponse. »

*Eragon, C. Paolini*



## Acknowledgements / Remerciements

As this nearly-six-year endeavor draws to an end, I cannot help but reflect on how much of a rollercoaster this has been, and how thankful I am to all the people who shared a bit of this journey with me, giving me a hand when I needed one, walking along with me for a while, or simply being there to enjoy good moments and get over less good ones.

I first would like to express my gratitude to Profs. **Alexandre Persat**, **Melanie Blokesch**, **Laurence van Melder** and **Adrian Egli**, for having accepted to review and evaluate this work. I fondly anticipate our scientific discussion. Thank you **John** for turning me into an independent scientist, and for teaching me to think critically about dogmas and preconceived ideas in science. These are valuable tools that I keep with me for my future undertakings. Thank you **Neeraj** for getting me up to speed with microbiology and molecular cloning as I began this journey, and for always being available to discuss fresh results, suggest new ideas, or answer any burning question I had. Thank you **François** for teaching me the nuts and bolts of bacterial and cell culture, and sharing an occasional “Oh yééé” when things were not working 😊 Thank you **Suzanne** for your swift and efficient administrative support throughout all steps of this PhD, and for our passionate conversations about music and theatre.

An immense and heartfelt thank you to all the UPKINites for creating and nurturing this amazing lab atmosphere, where people truly care for each other. I can honestly say there were times when you guys were my only motivation to come to the lab! Thank you **Vivek** (the Chancellor) for bringing this incredible energy and momentum

to the whole team. Thank you **Chiara** (blot blot Western baby) for sharing your protein tricks with me and always being open for discussion. Thank you **Richa** (the panettone girl) for your appreciation of Kugelhopf and Männele ☺ Thank you **Kunal** (master of the PEC PEC federation) for our great UPEC collaboration, and for suggesting the idea of the epithelial cell-based screen. I would not have reached this end-product without your input! Thank you **Fred** (l'étoile du Québec) for all your help with the persistence project, and for sharing my taste for Alsatian wines ☺ Thank you **Ophélie** ("Oh no, I need to go to the P3...") for your tremendous help with the adhesion project and your most appreciated moral support during rough patches. Thank you **Gaëlle, Joëlle, Sofia, Gauri, Dibya, Mélanie, Esther, Alex, Katrin, Amanda, Matthieu, Zela, Paul** and **Yoshiko** for all the good moments we shared in and outside the lab, this was a lot of fun! Many thanks also go to the students I had the opportunity to coach throughout this PhD: **Niko, Simon, Clélia, Anaïs, Gabriel, Lydia, Théo** and **Anouk**. This was unarguably one of my favorite parts of the job, and I learnt a ton while working with you. Thanks in particular to **Théo**, without whom the adhesion project would never have reached completion, and to **Anouk**, who definitely rescued the persistence project and turned it into something I can be proud of!

During these six years at EPFL, I also had the opportunity to interact with many brilliant scientists in the different core facilities of the faculty, and whom I would like to thank for the exceptional service they provide. Thanks to **Arne, Thierry, José, Romain, Olivier, Nicolas** and **Claire** from the BiOP facility for giving SV collaborators the opportunity to work with such cutting-edge and well-maintained microscopes, and for also helping out with the image analysis process, which God knows can be tedious. Thanks to **Graham, Anaëlle, Marie, Stéphanie** and **Arnault** from the BioEM facility

for taking beautiful images of UPEC and their pili. Thanks in particular to **Anaëlle** for developing the Ilastik image analysis pipeline, and producing this amazing bacterial artwork! Thanks to **Maria, Florence, Romain** and **Jonathan** from the proteomics facility, for helping me optimize the MS protocol and making me discover the fantastic world of proteins. Thanks to **Julien** and **Kaspar** from the CMI facility, for teaching me the rudiments of microfabrication. Finally, I would like to thank all the professors and collaborators of the Global Health Institute and the SV faculty in general, for offering this stimulating work environment, where ideas can be conceived, exchanged, discussed and improved with great support at all steps.

Merci également à toutes les personnes qui m'ont accompagné à côté du labo durant ces six dernières années. Merci notamment aux musiciennes et aux musiciens qui partagent ma passion de l'orchestre et que j'ai eu l'occasion de côtoyer au sein de l'Orchestre Symphonique et Universitaire de Lausanne, de l'Orchestre de Chambre des Etudiant·e·s de Lausanne, de l'Orchestre QuiPasseParLà, de l'Association Universitaire de Musique de Chambre et de l'Ensemble Evochia. Un merci tout particulier à l'incroyable équipe d'altistes de l'OQPPL : **Rosa, Philou, Lulu, Rachel, Frou, Mathieu, Max, Olivia, Marie, Élise** et **Estelle**. On joue moins de notes que les violons mais tcheu qu'est-ce qu'on se marre ! Un grand merci aussi à **Flo, Aline** et **Xavier** pour avoir partagé avec moi l'aventure du quatuor Fire Geder, alias Feu & Fromage, ainsi qu'à **Cécile** pour avoir ajouté un peu de piquant dans cette affaire ☺ Merci à l'équipe de l'OChE – **Giuseppe, Clem, Manu, Isa, Liz, Daria, Jeanne, Sam, Eugène** et **Lila** – pour nos randos et nos sorties ski organisées entre deux notes de musique. Merci à **Anaïs** pour ses cours de violon et d'alto au top qui faisaient un bien fou après le boulot !

Merci à vous toutes et tous que j'ai rencontrés au fil des ans en Alsace, en France et en Suisse, et sans qui toutes ces années d'études n'auraient de loin pas été aussi agréables. Merci en particulier à l'équipe EDBB (**Erik, Timo, Xavier, Romain, Colas et Sylvain**), à l'équipe de PC (**Thomas et Oriane, François, Sarah, Aurélien et Mélanie, Marc et Camille, Rodolphe et Amandine, Guillaume et Charlotte, Nico et Cerise, Vitor et Lydia**) ainsi qu'à l'équipe de Kléber (**Laulau, Jérèm, Florent et Kata, Julie et Raphaël**) pour tous ces bons moments passés ensemble.

Merci du fond du cœur à ma famille pour son soutien constant et sans faille depuis le tout début. Merci à mes parents sans qui je n'aurais jamais eu la chance de mener à bien ces longues études, et sur qui je peux compter quoi qu'il arrive. Merci à mes deux frangins qui sont toujours là pour me redonner le smile ☺ Merci vielmols à ma grand-mère pour son incroyable soutien moral et gastronomique ! Merci enfin à ma chère Alsace, et à Eschentzwiller en particulier, d'être cet endroit si chaleureux où il fait bon se ressourcer, et merci à Lausanne, d'être cette ville si dynamique où il fait bon vivre. Il paraît que les Alsaciens sont des Belges qui n'ont pas trouvé le chemin de la Suisse... Je crois que j'ai dérogé à la règle et je m'en félicite ;-)

Thomas

## **Table of contents**

<b>List of figures</b>	<b>12</b>
<b>List of tables</b>	<b>16</b>
<b>List of abbreviations</b>	<b>18</b>
<b>Abstract and keywords</b>	<b>20</b>
<b>Résumé et mots-clés</b>	<b>22</b>
<b>1. Introduction</b>	<b>25</b>
1.1. Uropathogenic <i>Escherichia coli</i> and recurrent urinary tract infections	25
1.2. Persistence of UPEC within the bladder	26
1.2.1. Pathogenesis of UTIs in the bladder	26
1.2.2. Adhesion of UPEC to bladder cells	27
1.2.3. Contribution of chaperone-usher pili to UPEC adhesion	29
1.3. Persistence of UPEC to antibiotic treatment	31
1.3.1. Bacterial persistence to antibiotics	31
1.3.2. Cellular signaling involved in persister generation	33
1.3.3. Antibiotic treatment of UTIs	35
1.4. Automated microscopy and high-content screening	36
1.5. Microfluidic-based screening	37
1.6. Aims of the thesis	38

## **2. General considerations on the construction of a transposon insertion library**

### **suitable for high-content UPEC imaging 39**

#### **2.1. Results 39**

##### **2.1.1. Construction of a non-flagellated UPEC strain 39**

##### **2.1.2. Construction of an ATP reporter UPEC strain 41**

##### **2.1.3. Integration of the fluorescent protein into the UPEC chromosome 45**

##### **2.1.4. Characterization of reference UPEC strains used in this work 47**

##### **2.1.5. Short conclusion and outlook 50**

#### **2.2. Materials and methods 50**

## **3. High-content screening identifies a critical role for P pili in early adhesion of**

### **UPEC to bladder cells 55**

#### **3.1. Results 55**

##### **3.1.1. A fluorescence microscopy-based assay to measure early adhesion of UPEC to bladder cells 55**

##### **3.1.2. High-content screening identifies UPEC mutants with altered adhesion to bladder cells 58**

##### **3.1.3. Genes that contribute positively or negatively to early adhesion of UPEC to bladder cells 61**

##### **3.1.4. P pili are key mediators of early adhesion to bladder cells 63**

##### **3.1.5. Type 1 pili are not essential for early adhesion to bladder cells 68**

##### **3.1.6. P pili expression is upregulated in F1C pili-deficient UPEC mutants 69**

##### **3.1.7. Quantification of single-cell piliation of pili-deficient UPEC mutants 73**

#### **3.2. Discussion and outlook 75**

#### **3.3. Materials and methods 79**



<b>4. High-content microfluidic screening identifies UPEC mutants with decreased persistence to fosfomycin in synthetic human urine</b>	<b>92</b>
4.1. Results	92
4.1.1. Design of the microfluidic screening platform	92
4.1.2. Optimization of the live UPEC spotting procedure	95
4.1.3. Selection of conditions for the study of UPEC antibiotic persistence	98
4.1.4. SHU provides a good model for persistence to FOS treatment	99
4.1.5. Time-lapse microscopy allows single-cell observation of UPEC persisters to FOS in SHU	102
4.1.6. High-content microfluidic screening identifies UPEC mutants with altered persistence to FOS in SHU	105
4.1.7. Characterization of UPEC mutants with decreased persistence to FOS in SHU	109
4.1.8. LPS core synthesis plays a key role in persistence to FOS in SHU	113
4.1.9. LPS synthesis is upregulated upon FOS treatment in SHU	115
4.2. Discussion and outlook	117
4.3. Materials and methods	120
<b>5. Appendices</b>	<b>131</b>
<b>6. References</b>	<b>138</b>
<b>7. Curriculum vitae</b>	<b>152</b>

## List of figures

Figure 1.1: Overview of UPEC pathogenesis in the bladder

Figure 1.2: Biogenesis of CUP pili

Figure 1.3: The dynamics of bacterial survival during antibiotic treatment

Figure 1.4: Single-cell visualization of *E. coli* persisters

Figure 2.1: *fliC* deletion from CFT073 improves microscopic imaging quality

Figure 2.2: Proof-of-work of the ATeam ATP biosensors in CFT073

Figure 2.3: Decrease in FRET efficiency of the ATeam biosensors in CFT073 can be recorded by fluorescence microscopy

Figure 2.4: Driving fluorescent protein expression from the chromosome of CFT073 decreases cell-to-cell fluorescence heterogeneity

Figure 2.5: Characterization of UPEC strains used in this work

Figure 3.1: A high-content screening assay to measure early adhesion of UPEC to bladder epithelial cells

Figure 3.2: 5637 bladder epithelial cells express markers specific to umbrella cells

Figure 3.3: Characterization of control UPEC strains used in the screen

Figure 3.4: Screening procedure and data analysis pipeline

Figure 3.5: Examples of UPEC mutants with altered adhesion to bladder epithelial cells identified through the screen

Figure 3.6: Chromosomal transposon insertion sites of UPEC mutants with altered adhesion to bladder epithelial cells

Figure 3.7: Early adhesion of UPEC to bladder epithelial cells is differentially regulated by multiple genes

Figure 3.8: Assignment of P pili transposon insertions to the *pap1* or *pap2* operons

Figure 3.9: Adhesion phenotypes of P pili transposon mutants

Figure 3.10: P pili are key mediators of early adhesion of UPEC to bladder epithelial cells

Figure 3.11: Type 1 pili are not essential for early adhesion of UPEC to bladder epithelial cells

Figure 3.12: Adhesion phenotypes of F1C pili transposon mutants

Figure 3.13: Adhesion phenotypes of unmarked F1C pili operon deletion mutants

Figure 3.14: P pili expression is upregulated in F1C pili-deficient high-adhesion UPEC mutants

Figure 3.15: Quantification of single-cell piliation of pili-deficient UPEC mutants

Figure 3.16: Automated quantification of UPEC single-cell piliation on SEM images using Ilastik

Figure 4.1: A microfluidic screening platform for high-content UPEC imaging

Figure 4.2: Schematic of the live UPEC spotting procedure

Figure 4.3: Increasing the ethanol washing time prevents UPEC cross-contamination between microchambers

Figure 4.4: SHU mimics the physiology and FOS response of UPEC in real urine

Figure 4.5: SHU provides a good model for UPEC persistence to FOS treatment

Figure 4.6: FOS treatment dynamics of UPEC in SHU can be followed by time-lapse microscopy using the microfluidic screening platform

Figure 4.7: UPEC can convert to cell-wall-deficient bacterial forms upon FOS treatment in SHU but not in LB

Figure 4.8: Microfluidic high-content screening identifies UPEC mutants with altered persistence to FOS in SHU

Figure 4.9: Examples of UPEC mutants with altered persistence identified during primary screen

Figure 4.10: Validation of UPEC mutants with altered persistence identified during primary screen

Figure 4.11: Characterization of UPEC mutants with confirmed decreased persistence to FOS in SHU

Figure 4.12: FOS treatment dynamics of UPEC mutants with confirmed decreased persistence in SHU

Figure 4.13: Persistence phenotypes of transposon UPEC mutants with impaired LPS core, O-antigen or capsule synthesis

Figure 4.14: LPS synthesis is upregulated in UPEC upon FOS treatment in SHU

## List of tables

Table 1.1: Sequence similarity between CFT073 chaperone-usher pili (CUP) operons

Table 2.1: Apparent ATP dissociation constants of the ATeam biosensors

Table 2.2: Characterization of reference UPEC strains used in this work

Table 3.1: Sequence similarity between *pap1* and *pap2* operons

Table 4.1: Growth and killing characteristics of CFT073  $\Delta fliC$  sfGFP in different media

Table 4.2: Growth and killing characteristics of UPEC mutants with confirmed decreased persistence to FOS in SHU

Table 4.3: Composition of Composite SHU medium

Table 4.4: Details of the flow and control wafer fabrication steps

Table 4.5: Optimization of the PDMS-to-glass bonding protocol

Table 5.1: Genes that contribute positively or negatively to early adhesion of UPEC to bladder epithelial cells

Table 5.2: Plasmids used in this work

Table 5.3: Primers used in this work

Table 5.4: Primer pairs used for assignment of P pili transposon insertions to the *pap1* or *pap2* operons

Table 5.5: qRT-PCR primers used in this work

## List of abbreviations

aa: amino acid  
AMP: ampicillin  
APTES: 3-aminopropyltriethoxysilane  
ATP: adenosine triphosphate  
bp: base pair  
CCCP: carbonyl cyanide m-chlorophenyl hydrazone  
CFP: cyan fluorescent protein  
CFU: colony-forming unit  
CHL: chloramphenicol  
CK8: cytokeratin 8  
CUP: chaperone-usher pili  
DAPI: 4',6-diamidino-2-phenylindole  
FBS: fetal bovine serum  
FRET: Förster resonance energy transfer  
FOS: fosfomicin  
G3P: glycerol-3-phosphate  
G6P: glucose-6-phosphate  
GPTES: 3-glycidoxypentyltriethoxysilane  
HCS: high-content screening  
HMDS: hexamethyldisilazane  
IBC: biofilm-like intracellular bacterial community  
gDNA: genomic DNA  
KAN: kanamycin  
 $K_d$ : apparent dissociation constant  
KEGG: Kyoto Encyclopedia of Genes and Genomes  
KO: KEGG orthology  
LB: Luria-Bertani broth  
LM: L-form medium  
LPS: lipopolysaccharide  
MIC: minimum inhibitory concentration  
MLSI: microfluidic large-scale integration



MOI: multiplicity-of-infection  
MS: mass spectrometry  
NIT: nitrofurantoin  
OD<sub>600</sub>: optical density at 600 nm  
pap: pyelonephritis-associated pili  
PBS: phosphate-buffered saline  
PDMS: polydimethylsiloxane  
PG: peptidoglycan  
PGMEA: propylene glycol methyl ether acetate  
QIR: quiescent intracellular reservoir  
qRT-PCR: quantitative real-time polymerase chain reaction  
RATE: rapid amplification of transposon ends  
rpm: revolutions per minute  
SEM: scanning electron microscopy  
sfGFP: superfolder green fluorescent protein  
SHU: synthetic human urine  
SXT: cotrimoxazole (trimethoprim:sulfamethoxazole 1:5)  
TA: toxin-antitoxin  
TMCS: trimethylchlorosilane  
Tn: transposon  
UDP-GlcNAc: uridine diphosphate N-acetylglucosamine  
UPEC: uropathogenic *Escherichia coli*  
UPK3A: uroplakin IIIa  
UTI: urinary tract infection  
WGS: whole-genome sequencing  
wt: wild-type  
YFP: yellow fluorescent protein

## Abstract and keywords

Uropathogenic *Escherichia coli* (UPEC) are the most common bacterial pathogens causing urinary tract infections (UTIs). Driven by the development of antibiotic-resistant UPEC strains, UTIs have become a major public health issue and generate substantial healthcare costs. Even in the absence of antibiotic resistance, UTIs are notoriously difficult to treat and have high rates of recurrence, mostly due to:

1. the ability of UPEC to adhere to and invade bladder epithelial cells, which protects them from the action of antimicrobial agents and the immune system
2. the presence in antibiotic-susceptible UPEC populations of a small fraction of so-called persister cells, which are killed at a slower rate than the bulk of the population and can therefore survive prolonged antibiotic exposure

These two features allow some bacteria to remain viable in a protected niche for the whole duration of the antibiotic treatment, potentially leading to infection relapse when the treatment is terminated.

High-content screening (HCS), which uses microscopy as a screening tool, allows the visualization of bacterial phenotypes at the single-cell level and can therefore provide a powerful and unbiased tool to understand the genetic basis of these phenotypes. The present thesis describes two complementary high-content screening approaches aimed at identifying UPEC mutants with altered adhesion to bladder cells and with altered antibiotic persistence respectively.

In a first chapter, we report preparatory steps that led to the construction of a transposon insertion library of UPEC mutants that is suitable for high-content imaging, using the CFT073 clinical UTI isolate as background strain.

In the second chapter, we performed fluorescence microscopy-based high-content screening to identify mutants with defects in early adhesion to bladder epithelial cells. We recovered 82 mutants with decreased adhesion and 54 mutants with increased adhesion. Unexpectedly, nine low-adhesion “hits” mapped to the two P pili operons encoded by CFT073, which are thought to mediate adhesion to kidney cells rather than bladder cells. Additionally, six high-adhesion “hits” mapped to the operon coding for F1C pili, and we show that this phenotype is linked to increased P pili synthesis. These results therefore reveal a critical role for P pili in UPEC adhesion to bladder epithelial cells, which may inform the development of novel anti-adhesion therapies to prevent UTI recurrence.

In the third chapter, we combined microfluidics with time-lapse microscopy to identify mutants with altered persistence to fosfomycin (FOS) – a cell-wall inhibitor used as first-line agent in the treatment of UTIs – in synthetic human urine (SHU), which mimics the physiology of UPEC in real urine. We recovered four mutants with decreased persistence, three of which had defects in lipopolysaccharide (LPS) synthesis. These results identify the outer membrane of UPEC as a key component for survival to FOS treatment, thus opening up new avenues in the fight against antibiotic persistence.

Keywords: uropathogenic *Escherichia coli* (UPEC); urinary tract infections (UTIs); transposon insertion library; high-content screening (HCS); bladder epithelial cells; bacterial adhesion; antibiotic persistence; microfluidics; time-lapse microscopy

## Résumé et mots-clés

Les *Escherichia coli* uropathogènes (UPEC) sont les principales bactéries responsables des infections des voies urinaires (IVU). En raison du développement de souches résistantes aux antibiotiques, les infections urinaires sont devenues un problème majeur de santé publique et génèrent des coûts de santé importants. Même en l'absence d'antibiorésistance avérée, les infections urinaires sont souvent difficiles à traiter et présentent des taux de récurrence élevés, principalement en raison de :

1. la capacité des UPEC à adhérer aux cellules épithéliales de la vessie et à les envahir, ce qui les protège ensuite de l'action des agents antimicrobiens et du système immunitaire
2. la présence, dans les populations d'UPEC sensibles aux antibiotiques, d'une petite fraction de bactéries dites persistantes, qui sont tuées à un taux inférieur à celui du reste de la population et peuvent donc survivre à une exposition prolongée aux antibiotiques

Ces deux caractéristiques permettent ainsi à certaines bactéries de rester en vie durant toute la durée du traitement antibiotique, ce qui peut entraîner une rechute de l'infection à l'arrêt du traitement.

Le criblage à haut contenu, qui utilise la microscopie comme outil de criblage, permet de visualiser les phénotypes bactériens directement au niveau des cellules et constitue donc un outil puissant pour comprendre l'origine génétique de ces phénotypes. La présente thèse décrit deux approches complémentaires de criblage à haut contenu visant à identifier des mutants d'UPEC présentant respectivement une adhésion altérée aux cellules de la vessie et une persistance altérée aux antibiotiques.

Dans un premier chapitre, nous détaillons les étapes préparatoires qui ont conduit à la construction d'une bibliothèque d'insertions de transposon adaptée à l'imagerie à haut contenu, en utilisant l'isolat clinique CFT073 comme souche de base.

Dans le deuxième chapitre, nous avons effectué un criblage à haut contenu basé sur la microscopie à fluorescence afin d'identifier des mutants présentant des défauts d'adhésion aux cellules épithéliales de la vessie. Nous avons identifié 82 mutants ayant une adhésion réduite et 54 mutants ayant une adhésion accrue. De manière inattendue, neuf mutants à faible adhésion ont été localisés dans les deux opérons de CFT073 codant pour les pili P, supposés être les vecteurs de l'adhésion aux cellules rénales plutôt qu'aux cellules de la vessie. De plus, six mutants à forte adhésion ont été identifiés dans l'opéron codant pour les pili F1C, et nous montrons que ce phénotype est lié à une augmentation de la synthèse des pili P. Ces résultats révèlent le rôle critique des pili P dans l'adhésion des UPEC aux cellules de la vessie, ce qui pourrait contribuer au développement de nouvelles thérapies anti-adhésion pour prévenir les récurrences d'infections urinaires.

Dans le troisième chapitre, nous avons combiné la microfluidique et la microscopie time-lapse afin d'identifier des mutants présentant une persistance altérée à la fosfomycine – un inhibiteur de la paroi cellulaire utilisé comme agent de première ligne dans le traitement des infections urinaires – dans un milieu synthétique imitant la physiologie des UPEC dans l'urine humaine. Nous avons découvert quatre mutants présentant une persistance réduite, dont trois présentant des défauts dans la synthèse du lipopolysaccharide (LPS). Ces résultats identifient donc la membrane externe des UPEC comme un élément clé de leur survie au traitement par la fosfomycine, ouvrant ainsi de nouvelles voies dans la lutte contre la persistance aux antibiotiques.

Mots-clés : *Escherichia coli* uropathogènes (UPEC) ; infections des voies urinaires (IVU) ; bibliothèque d'insertions de transposon ; criblage à haut contenu ; cellules épithéliales de vessie ; adhésion bactérienne ; persistance aux antibiotiques ; microfluidique ; microscopie time-lapse

# 1. Introduction

## 1.1. Uropathogenic *Escherichia coli* (UPEC) and recurrent urinary tract infections

Urinary tract infections (UTIs) are among the most frequent infections in humans, with about 60% of women developing a UTI at least once in their lifetime ([Foxman et al., 2000](#); [Foxman, 2002](#)). Most community-acquired UTIs are initiated when bacteria originating from the fecal flora ascend up the urethra and colonize the bladder lumen and tissue, leading to acute cystitis ([Klein and Hultgren, 2020](#)). In a small number of cases, bacteria ascend further through the ureters into the kidney, a condition known as pyelonephritis, which can quickly evolve into life-threatening urosepsis ([Katchman et al., 2005](#); [Scholes et al., 2005](#); [Nicolle, 2008](#)). About 80% of community-acquired UTIs are caused by a heterogeneous group of *Escherichia coli* strains that are specifically adapted to colonizing the urinary tract, and that are collectively termed uropathogenic *E. coli* (UPEC) ([Foxman, 2010](#); [Flores-Mireles et al., 2015](#)). Due to the rapid development and spread of antimicrobial resistance among UPEC strains, UTIs have become increasingly difficult to treat, imposing a high economic burden on healthcare systems ([Simmering et al., 2017](#)). Even in the absence of clinically detectable antibiotic resistance, UTIs are characterized by high rates of recurrence, and it is estimated that 30% of women will experience a second infection within one year of resolution of their initial episode, despite receiving appropriate antibiotic treatment ([Foxman, 2014](#); [Lacerda Mariano et al., 2020](#)). In the vast majority of cases, this second infection is caused by the same UPEC strain as the initial episode, suggesting UPEC persistence within the urinary tract ([Ejrnaes et al., 2006](#)).

## 1.2. Persistence of UPEC within the bladder

### 1.2.1. Pathogenesis of UTIs in the bladder

To gain a foothold in the urinary tract, UPEC have evolved the ability to form biofilms and to invade urothelial cells, which protects bacteria from clearance by antimicrobial agents and the host immune system ([Wiles et al., 2008](#); [Lewis et al., 2016](#); [Terlizzi et al., 2017](#); [Blango and Mulvey, 2010](#)). Much of our current understanding of UPEC pathogenesis in the bladder is derived from studies conducted using mouse models of infection ([Barber et al., 2016](#); [Murray et al., 2021](#)). Upon reaching the murine bladder lumen, UPEC can adhere to superficial umbrella cells of the urothelium, which triggers their internalization ([Mulvey et al., 1998](#); [Martinez et al., 2000](#)). There, they proliferate quickly to form biofilm-like intracellular bacterial communities (IBCs) comprising hundreds to thousands of bacteria ([Anderson et al., 2003](#); [Duraishwamy et al., 2018](#)). Efflux of bacteria from IBCs back into the bladder lumen results in infection of neighboring umbrella cells, thus perpetuating the infection cycle ([Justice et al., 2004](#); [Iosifidis and Duggin, 2020](#); see also **Figure 1.1**). Noticeably, IBCs have been observed within exfoliated epithelial cells in the urine of cystitis patients, confirming their importance in human infection ([Rosen et al., 2007](#); [Robino et al., 2014](#); [Martinez-Figueroa et al., 2020](#)). More recently, the role of IBCs in reseeding infection upon cessation of antibiotic treatment was supported by direct microscopic observation using a bladder-chip model that mimics the architecture of the human bladder ([Sharma et al., 2021b](#)). UPEC may also invade into deeper layers of the bladder urothelium and establish quiescent intracellular reservoirs (QIRs), which have been postulated to



be responsible for long-term infection relapse ([Mysorekar and Hultgren, 2006](#); [Schwartz et al., 2011](#); [Sharma et al., 2021a](#)).

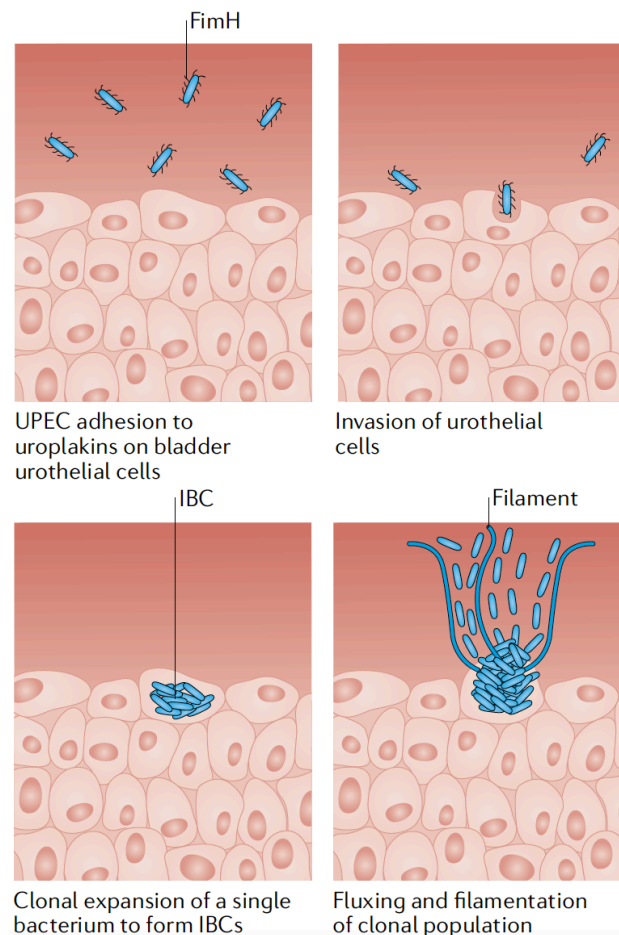


**Figure 1.1: Overview of UPEC pathogenesis in the bladder.** UPEC adhere to and invade superficial umbrella cells in a FimH-dependent manner (see **Section 1.2.3**). There, they undergo clonal expansion to form IBCs, where they can evade mechanical and immunological clearance mechanisms of the host, as well as antibiotic treatment. They later flux out of the umbrella cells into the bladder lumen, where they can subsequently adhere to neighboring cells and begin a new infection cycle. Panel adapted from [Klein and Hultgren, 2020](#).

### 1.2.2. Adhesion of UPEC to bladder cells

Adhesion of UPEC to the umbrella cells lining the bladder lumen is a necessary prelude to invasion of urothelial cells and formation of IBCs and QIRs, as it prevents

mechanical elimination of bacteria by the bulk flow of urine (Bien et al., 2012; Flores-Mireles et al., 2015). In recent years, novel therapeutic strategies targeting UPEC adhesion have emerged as an exciting alternative to conventional antibiotic therapy (Spaulding et al., 2017; Sarshar et al., 2020). Bacteria assemble a wide variety of structures to mediate adhesion to surfaces, including pili, also known as fimbriae (Pizarro-Cerda and Cossart, 2006; Kline et al., 2009). Among pathogenic Gram-negative bacteria, the family of chaperone-usher pili (CUP) mediates most of the interactions with host cells, with a tissue tropism dependent on the tip adhesin (Waksman and Hultgren, 2009; Thanassi et al., 2012; see also **Figure 1.2**). The collective pangenome of UPEC strains harbors at least 38 distinct CUP operons, and genomes of individual UPEC strains often encode several of them, providing bacteria with the ability to bind to a variety of receptors and surfaces (Wurpel et al., 2013).

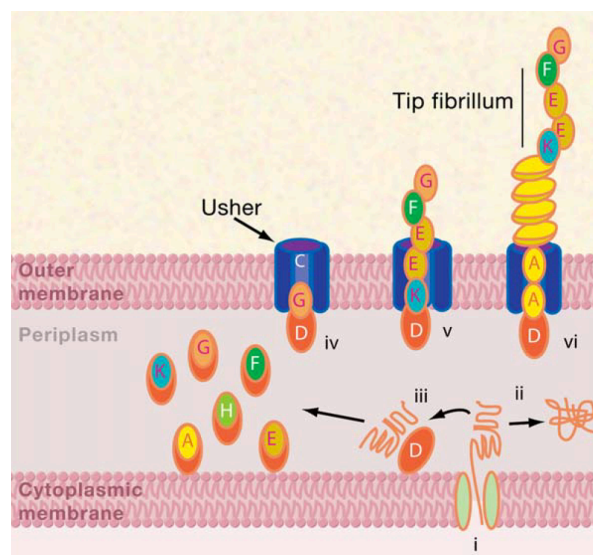


**Figure 1.2: Biogenesis of CUP pili** (example shown for P pili). Individual pili components are first transported from the cytoplasm to the periplasm via the Sec pathway (i). In the absence of the chaperone PapD, pili subunits are degraded (ii). Otherwise, PapD stabilizes the subunits (iii) and transports them to the outer membrane usher PapC (iv). The tip adhesin PapG is assembled first, then pili grow from their base (v). The final structure is acquired outside the bacteria (vi). Panel adapted from Pizarro-Cerda and Cossart, 2006.

### 1.2.3. Contribution of chaperone-usher pili to UPEC adhesion

For example, the genome of the well-studied clinical UPEC isolate CFT073 contains 10 CUP operons ([Welch et al., 2002](#); see also **Table 1.1**), among which the type 1 pili and P pili have been shown to play key roles in colonization of the bladder and kidney, respectively. Type 1 pili mediate UPEC adhesion in the bladder via binding of the adhesin FimH to mannosylated uroplakin residues present on the surface of bladder umbrella cells ([Mulvey et al., 1998](#); [Martinez et al., 2000](#); [Hung et al., 2002](#); [Wright et al., 2007](#); see also **Figure 1.1**), while P pili mediate UPEC adhesion in the kidney via binding of the adhesin PapG to globoside glycolipids expressed by kidney epithelial cells ([Roberts et al., 1994](#); [Dodson et al., 2001](#); [Johnson et al., 2005](#); [Lane et al., 2007](#); [Lillington et al., 2014](#)). In addition to the well-characterized type 1 and P pili, recent studies have implicated several other types of pili in adhesion to urothelial cells, including F9 pili, Yad pili, and Ygi pili ([Wurpel et al., 2014](#); [Conover et al., 2016](#); [Spurbeck et al., 2011](#)).

However, the contribution of different pili types to adhesion to different tissues is often assessed using lab-adapted *E. coli* strains recombinantly expressing one pili type, rather than fully virulent UPEC strains, which can simultaneously express several types of pili at the population level. Different pili operons also have the possibility to cross-regulate each other, through a mechanism known as phase variation ([Holden and Gally, 2004](#); [Totsika et al., 2008](#)). Besides, conventional adhesion assays are usually based on the quantification of host-cell-associated bacteria through measurement of colony-forming unit (CFU) counts after cell lysis, what is more at late timepoints, when it becomes difficult to distinguish between adhesion and invasion.

These considerations served as the basis for the first high-content screen presented in this work, aimed at identifying UPEC mutants with altered early adhesion to bladder cells.

	<b>P pili (<i>pheV</i>)</b>	<b>P pili (<i>pheU</i>)</b>	<b>F1C pili</b>	<b>F9 pili</b>	<b>Auf pili</b>	<b>Yad pili</b>	<b>Yfc pili</b>	<b>Yeh pili</b>	<b>Yqi pili</b>
<b>A.</b> major pilin	PapA	PapA_2	FocA	c1936	c4214 (AufG)	c0172 (YadN)	c2884 (YfcV)	c2638 (YehD)	c3791 (YgiL)
% aa identity with FimA	33.15 %	30.60 %	63.39 %	63.64 %	29.21 %	24.28 %	29.27 %	29.03 %	33.33 %
<b>B.</b> chaperone	PapD	PapD_2	FocC	c1935	c4213	c0171 (EcpD)	c2882 (YfcS)	c2637 (YehC)	c3793 (YqiH)
% aa identity with FimC	33.87 %	33.87 %	64.47 %	59.83 %	45.33 %	29.87 %	31.20 %	28.77 %	28.77 %
<b>C.</b> usher	PapC	PapC_2	FocD	c1934	c4212 (YcbS)	c0170 (HtrE)	c2883 (YfcU)	c2636 (YehB)	c3792 (YqiG)
% aa identity with FimD	30.18 %	30.18 %	64.40 %	57.94 %	45.77 %	32.09 %	27.49 %	29.50 %	28.95 %
<b>D.</b> adhesin	PapG	PapG_2	FocH	c1931 (YdeQ)	c4207 (AufA)	c0166 (YadC)	c2878 (YfcO)	c2635 (YehA)	c3794
% aa identity with FimH	not found	not found	36.09 %	47.65 %	not found	not found	not found	not found	not found

**Table 1.1: Sequence similarity between CFT073 chaperone-usher pili (CUP) operons.** The percentage of amino acid (aa) sequence identity between homologous proteins of the different operons was calculated using pBlast. In each case, the corresponding protein of the type 1 pili operon was used as reference. **(A)** major pilin subunit; **(B)** chaperone protein; **(C)** usher subunit; **(D)** pili tip adhesin.

## 1.3. Persistence of UPEC to antibiotic treatment

### 1.3.1. Bacterial persistence to antibiotics

Adhesion to and invasion of bladder epithelial cells by UPEC is not the only reason explaining their recalcitrance to antibiotic treatment in the absence of underlying antibiotic resistance. Antibiotic persistence is increasingly viewed as another major cause of antibiotic treatment failure and infection relapse ([Blango and Mulvey, 2010](#); [Gupta, 2001](#)). Unlike resistant bacteria, which have acquired genetic mutations allowing them to grow in the presence of antibiotic concentrations that are normally inhibitory, persister bacteria arise within a genetically susceptible population ([Fisher et al., 2017](#)). They form a small fraction of the population that is able to survive prolonged exposure to bactericidal agents by transiently entering a physiological state in which antibiotics kill them at a much slower rate than the bulk of the population ([Balaban et al., 2013](#); [Dhar and McKinney, 2007](#)).

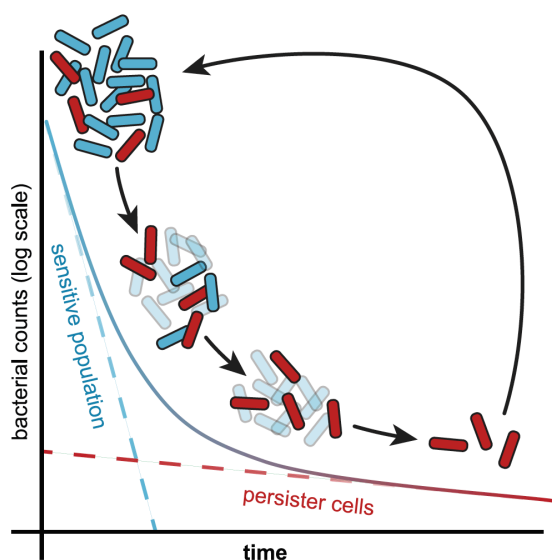


**Figure 1.3. The dynamics of bacterial survival during antimicrobial treatment.**

The bulk of the population (blue) is sensitive to the antibiotic and is rapidly killed at the beginning of the treatment until only persister cells (red) remain, due to their slower killing rate. The termination of the antibiotic treatment enables surviving persisters to regrow and regenerate the bacterial population. Panel adapted from [Harms et al., 2016](#).

The presence of persister cells in a clonal population exposed to a lethal dose of antibiotic can easily be detected when the fraction of viable cells is measured over time in what is commonly referred to as a “time-kill curve” assay ([Balaban et al., 2019](#)). A characteristic biphasic pattern is then observed: while the majority of the population is rapidly killed, resulting in a fast exponential decay in the first few hours of antibiotic treatment, persister cells die with much slower kinetics, causing the curve to progressively flatten out (**Figure 1.3**). When the treatment ceases, a small fraction of persister cells may still survive and can switch back to a regular growing state, thus replenishing the bacterial population. Importantly, persisters regenerate a population as susceptible to the antibiotic as the original one ([Harms et al., 2016](#)), meaning that their offspring does not acquire genetically-encoded antibiotic resistance.

Persister cells were first identified in 1944 when Joseph Bigger established that about one in a million cells in a clonal population of *Staphylococcus pyogenes* was able to survive extended exposure to penicillin ([Bigger, 1944](#)). The phenomenon has since been observed in most bacterial species. Yet, for about 60 years, the mechanisms behind the formation of persister cells remained largely unexplored, mostly due to the technical challenges associated with the study of a transient phenotype that is displayed by only a small fraction of cells ([Michiels et al., 2016](#)). In 2004, a breakthrough study by [Balaban et al., 2004](#) reported for the first time the visualization of individual *E. coli* persister cells. This was made possible by the identification of *hipA7* mutants with a higher persistence rate ([Moyed et al., 1983](#)), as well as the use of transparent microfluidic devices, which enabled time-lapse imaging at the single-cell level. The authors thus showed that persistence was linked to a pre-existing phenotypic heterogeneity in the bacterial population, with persister cells already

having a reduced growth rate before the beginning of antibiotic exposure (Balaban et al., 2004; see also **Figure 1.4**).

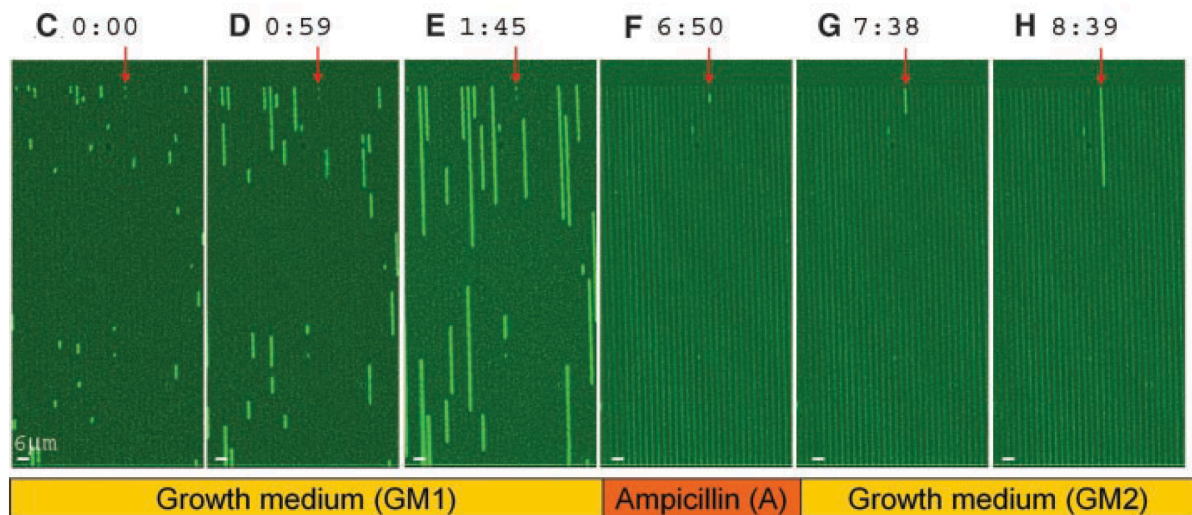


**Figure 1.4: Single-cell visualization of *E. coli* persisters using a combination of microfluidics and time-lapse microscopy.** Fluorescent time series of *hipA7* mutant *E. coli* cells expressing the yellow fluorescent protein (YFP), cultured using a microfluidic device patterned with polydimethylsiloxane (PDMS) grooves. Bacteria grew and established linear microcolonies (**C,D,E**), prior to treatment with ampicillin for 5 hours (**F**), which lysed susceptible cells. Red arrows indicate a non-growing persister cell that resumed growth upon antibiotic removal (**G,H**). Panel adapted from Balaban et al., 2004.

### 1.3.2. Cellular signaling involved in persister generation

Following this pioneering discovery, bacterial persistence was studied in earnest and is now generally understood to arise from the phenotypic diversity within a clonal population (Dhar and McKinney, 2007). Stochastic variation in gene expression at the single-cell level accounts in part for this diversity, allowing some individual cells to better survive changing environmental conditions, in what has been described as a



“bet-hedging” strategy ([Balaban et al., 2013](#)). In addition, persister cell formation seems to be induced by environmental cues indicating imminent threats for the bacteria, such as antibiotic exposure or stationary-phase-induced starvation ([Harms et al., 2016](#)). Interestingly, prolonged antibiotic regimens have been shown to select *in vitro* for mutants displaying higher persistence rates ([Fridman et al., 2014](#)). Thus, even though persistence is by definition a non-heritable phenotypic trait, the pathways used for survival by individual cells are genetically encoded and can be mutated, leading to modulations in the persistence rate.

Recently, several studies have begun to shed light on the molecular and genetic mechanisms of persister cell formation. A common approach involved screening a knockout gene library for mutants with altered persistence rates, which has led to the identification of several “persister genes” in *E. coli* ([Spoering et al., 2006](#); [Hansen et al., 2008](#)). Importantly, no mutant completely lacking persister cells could be identified during these procedures, which seems to indicate the redundancy of persister formation mechanisms ([Michiels et al., 2016](#)).

“Persister genes” comprise several toxin-antitoxin (TA) modules – including the *hipBA* locus that proved instrumental to the observation of persister cells – that are now intensively studied in relation to persistence ([Ronneau and Helaine, 2019](#)). TA modules consist of a stable toxin, usually inhibiting essential cellular processes (such as DNA replication, DNA transcription, protein synthesis, or proton motive force) and an unstable antitoxin, which counteracts the activity of its associated toxin ([Gerdes and Maisonneuve, 2012](#); [Van Melderren, 2010](#)). TA modules were originally identified on plasmids where they are thought to serve as selection markers during cell division:



if the plasmid is absent in a daughter cell, the cytoplasmically inherited antitoxin is degraded and the toxin kills the new cell, a mechanism known as “post-segregational killing” ([Fraikin et al., 2020](#)). The activation of toxins was initially thought to occur through antitoxin degradation by the Lon protease, following activation of the stringent response ([Harms et al., 2016](#)), although the original study papers were later retracted, due to the discovery that several *E. coli* mutant strains had been infected with a bacteriophage ([Harms et al., 2017](#); [Goormaghtigh et al., 2018](#)). As of now, the link between TA modules and persistence thus remain unclear.

### 1.3.3. Antibiotic treatment of UTIs

Most studies on antibiotic persistence of *E. coli* were carried out so far by treating non-pathogenic lab-adapted strains with broad-spectrum antibiotics, such as the beta-lactam ampicillin or the fluoroquinolone ciprofloxacin, using nutrient-rich media, such as Luria-Bertani (LB) or Mueller-Hinton broth ([Balaban et al., 2004](#); [Dörr et al., 2010](#); [Orman and Brynildsen, 2015](#); [Windels et al., 2019](#)). However, this standard setup has three major shortcomings when translated to the study of antibiotic persistence in the context of urinary tract infections (UTIs):

1. Antibiotic survival mechanisms might be different between lab-adapted *E. coli* strains and pathogenic strains such as UPEC, especially considering the large amount of genomic variation between both groups. For example, the CFT073 UPEC strain was shown to only have 75% of genes in common with K-12 strains classically used in laboratories ([Kaper et al., 2004](#)).

2. Beta-lactams and fluoroquinolones provide good models for studies on antibiotic persistence but are not recommended as first-line drugs against uncomplicated UTIs anymore, due to high resistance rates in the general population ([Gardiner et al., 2019](#)).
3. The use of nutrient-rich media is unlikely to reflect the physiology of UPEC in the context of a real infection ([Ipe et al., 2016](#)). These media also suffer from known batch-to-batch variation that can greatly affect the outcome of persistence assays ([Harms et al., 2017](#)).

**These considerations motivated the second high-content screen presented in this work, where we aimed at identifying UPEC mutants with altered antibiotic persistence under clinically and physiologically relevant conditions.**

## **1.4. Automated microscopy and high-content screening (HCS)**

Recent technological advances now enable the use of automated microscopy for screening purposes. When combined with automated image analysis, this technique is referred to as high-content screening (HCS) and yields large-scale quantitative data at the single-cell level ([Usaj et al., 2016](#)). Originally developed to screen small-compound libraries, HCS is now widely used to answer more fundamental questions in systems biology. For example, [Neumann et al., 2010](#) carried out a whole-genome phenotypic screen on an RNAi library of HeLa cells, leading to the discovery of several novel genes involved in mitosis. To date, most HCS assays were performed with mammalian cells in static platforms, such as micro-well titer plates ([Boutros et al.,](#)

2015). However, the use of micro-well plates can prove challenging for the study of bacterial phenotypes since bacteria do not adhere to the bottom of the wells like mammalian cells. In addition, it is not possible to switch medium during the course of an experiment when using micro-well plates, which makes them unsuitable to screen for phenotypes that appear only in dynamic environments, such as persistence.

## 1.5. Microfluidic-based screening

Microfluidic platforms can offer solutions to these two limitations. Microfluidics is a recently developed technology that allows manipulation of fluids at the microscopic scale, using microchannels imprinted on a soft device. Microfluidic devices are usually made of polydimethylsiloxane (PDMS), a transparent elastomeric material that can be easily processed using soft lithography techniques, and which is ideal for optical measurement (Franssila, 2010). Devices can consist of a single microchannel, such as the ones used for capillary electrophoresis (Andersson et al., 2003), or comprise thousands of channels to deliver medium to microchambers where cells or bacteria can be grown, such as in microfluidic large-scale integration (MLSI) devices (Maerkl, 2009). The size and shape of the microchambers can be precisely defined to perfectly accommodate the organism of interest, for example to limit bacterial motility, and micromechanical valves can be used to control medium supply inside the device. Microfluidics is therefore an ideal tool to perform HCS assays, and its combination with time-lapse microscopy enables long-term monitoring of single-cell dynamics with precise control of the environment.

## **1.6. Aims of the thesis**

In the present thesis, we employed recent technological advances in automated microscopy and microfluidics to perform high-content screening assays aimed at better understanding the genetic basis for the high recurrence rates of UPEC-caused UTIs. The thesis therefore focuses on three aims:

1. To build a transposon library of UPEC mutants that is well-suited for high-content screening and allows robust and easy image analysis
2. To take advantage of UPEC adhesion to bladder epithelial cells to screen for UPEC mutants with defects in early adhesion, using a micro-well plate format and a high-throughput fluorescence microscopy-based setup
3. To select clinically and physiologically relevant conditions for the study of UPEC antibiotic persistence and apply them to screen for UPEC mutants with altered persistence, using a setup combining microfluidics and time-lapse microscopy

## **2. General considerations on the construction of a transposon insertion library suitable for high-content UPEC imaging**

The purpose of this chapter is to present steps that led to the construction of the library of UPEC transposon mutants, which we used for high-content screening in the two following chapters. In order to facilitate the identification of disrupted genes in mutants displaying altered phenotypes, the whole study was conducted using the CFT073 clinical UPEC isolate ([Mobley et al., 1990](#)), for which the whole genome has been sequenced and annotated ([Welch et al., 2002](#)). Successive genetic manipulations of this background strain were performed following two main considerations:

- the quantity of information that can be extracted from screening assays, which basically corresponds to the number of independent fluorescent reporters that can be used to provide information on the bacterial status
- the quality of information collected, which directly influences the performance of quantitative readouts used to identify mutants with aberrant phenotypes

### **2.1. Results**

#### **2.1.1. Construction of a non-flagellated UPEC strain**

In order to facilitate single-cell imaging, we first engineered a UPEC strain that constitutively expresses a fluorescent protein. To this end, CFT073 was transformed with a pZA32 plasmid containing the sequence of the yellow fluorescent protein (YFP) under control of the  $P_{\text{LacO-1}}$  promoter. In the absence of the *lac* repressor protein LacI,

this promoter functions as a constitutive one (Lutz et al., 1997), driving strong YFP expression that could be recorded by fluorescence microscopy (**Figure 2.1A**). We found however that the quality of imaging was somewhat reduced by UPEC swimming motility, resulting in blurred images with strong misalignment between the phase-contrast and fluorescence channels (**Figure 2.1A**). Since this was likely to limit the quality of information that can be extracted from screening assays, we engineered a non-flagellated UPEC strain by constructing an unmarked deletion of the *fliC* gene encoding flagellin (see **2.2. Materials and methods**). Deletion of *fliC* was previously shown to completely abolish swimming motility in CFT073 (Lane et al., 2005). Accordingly, the quality of microscopic images was appreciably improved when using CFT073  $\Delta fliC$  compared to the wild-type strain (**Figure 2.1B**).

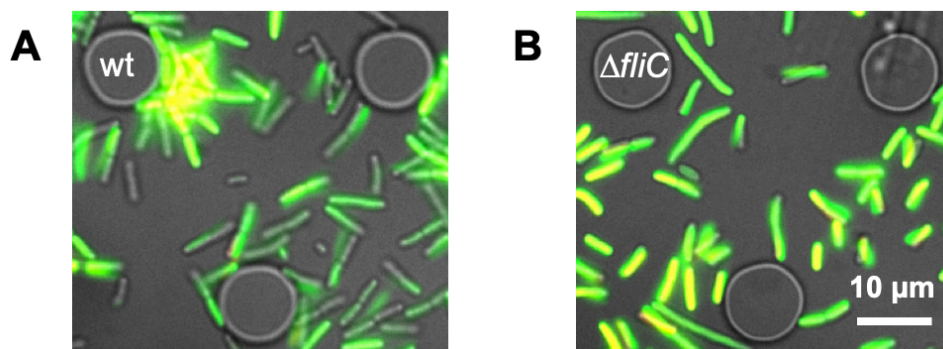


**Figure 2.1: *fliC* deletion from CFT073 improves microscopic imaging quality.** CFT073 wild-type (**A**) and  $\Delta fliC$  (**B**), both expressing YFP from an episomal plasmid, were cultured in LB medium using the microfluidic platform described in **Chapter 4**, and imaged on phase-contrast and yellow fluorescence channels. The circular structures correspond to PDMS pillars of the microfluidic device (see details in **Figure 4.1**). Scale bar: 10  $\mu\text{m}$  for both images.

In retrospect, *fliC* deletion proved necessary to prevent UPEC from swimming between microchambers inside the microfluidic device (see **Chapter 4**), which could

otherwise generate undesirable cross-contamination between different UPEC mutants. The use of a non-flagellated strain also allowed detection with good resolution of pili proteins using mass spectrometry (MS) analysis of the bacterial surface proteome, which would otherwise be cluttered by huge amounts of the FliC protein; as well as quantification of single-cell UPEC piliation on scanning electron microscopy (SEM) images, which would be impossible in the presence of flagella (for MS and SEM analyses, see **Chapter 3**).

### **2.1.2. Construction of an ATP reporter UPEC strain**

We next looked into coupling important bacterial processes to the expression of fluorescent reporter proteins, so as to provide a microscopic readout of UPEC physiology in real time and therefore increase the information content of our screening assays. Thinking mostly about the screen aimed at identifying UPEC mutants with altered antibiotic persistence, we selected the Förster resonance energy transfer (FRET)-based ATP reporter construct developed by [Imamura et al., 2009](#) (**Figure 2.2A**). ATP availability can affect antibiotic persistence in different ways: while it was shown that bacterial persisters are associated with low levels of ATP in a lab strain of *Escherichia coli* ([Dörr et al., 2010](#); [Verstraeten et al., 2015](#)) and in *Staphylococcus aureus* ([Conlon et al., 2016](#)), persister cells of *Mycobacterium smegmatis* maintain high ATP levels during antibiotic exposure ([Maglica et al., 2015](#)). As for UPEC, it is not known whether modulation of ATP levels contributes to persister formation, but this could be elucidated in our screening assay, potentially leading to a better understanding of the mechanisms underlying altered persistence in the identified transposon mutants.

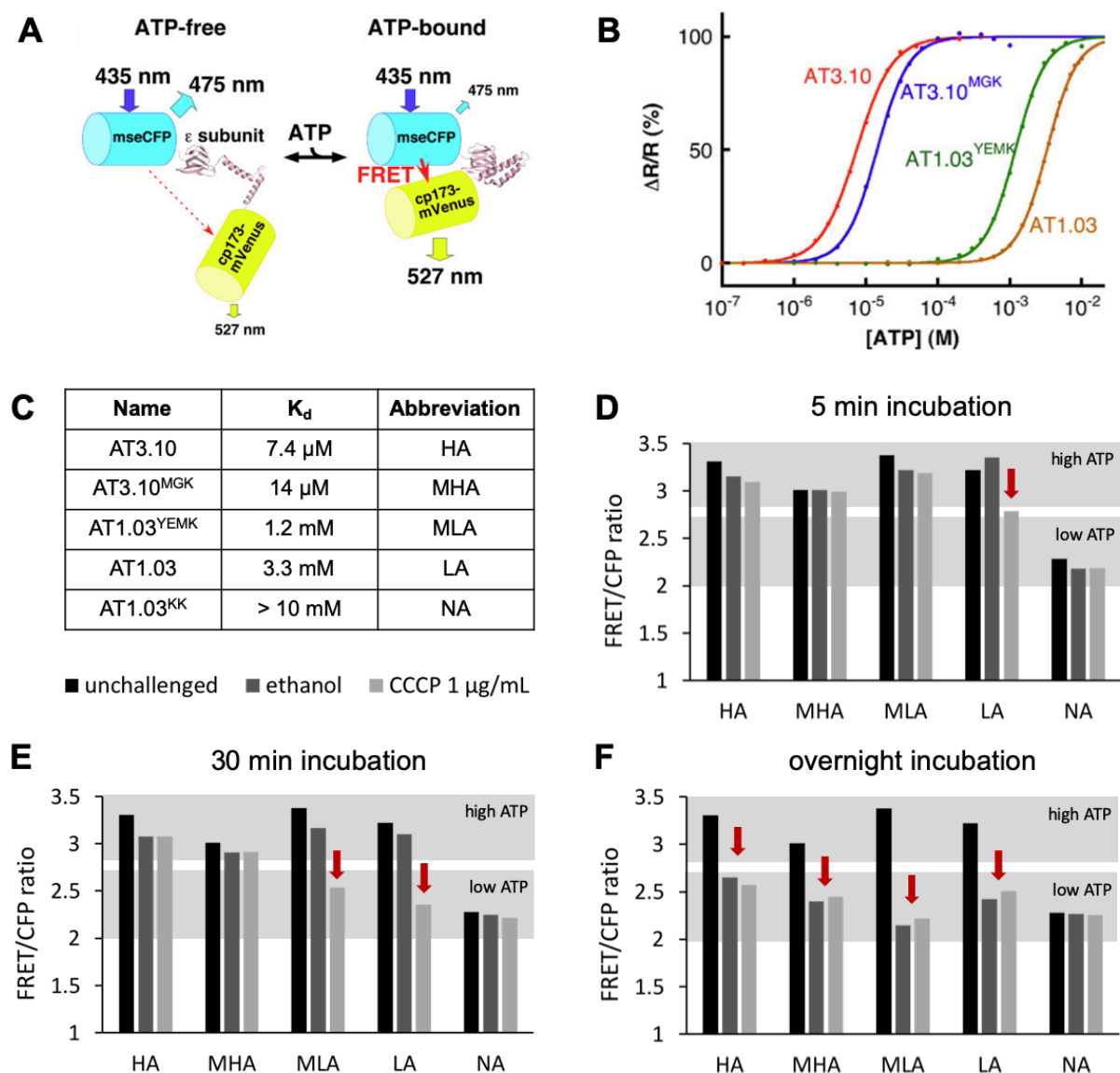


**Figure 2.2: Proof-of-work of the ATeam ATP biosensors in CFT073.** (A) Schematic of the FRET-based ATeam biosensor developed by Imamura et al., 2009. Variants of CFP (mseCFP, blue) and YFP (cp173-mVenus, yellow) are connected to the epsilon subunit of the  $F_0F_1$  ATP synthase from *Bacillus subtilis*. In the ATP-free form (left), the extended conformation of the epsilon subunit separates the two fluorescent proteins, resulting in low FRET efficiency. In the ATP-bound form (right), the epsilon subunit retracts and draws the two fluorescent proteins close to each other, thereby increasing FRET efficiency. FRET efficiency can be measured by the FRET/CFP emission ratio (527/475 nm) when exciting at 435 nm. (B) ATP-dependent FRET/CFP emission ratio (R) changes for four ATeam biosensors with different affinities for ATP. In each case, the fraction of FRET/CFP emission ratio change ( $\Delta R/R$ ) is plotted against the ATP concentration. (C = Table 2.1) Apparent ATP dissociation constants ( $K_d$ ) of the ATeam biosensors, and abbreviations used in this work: HA



(high affinity), MHA (medium-high affinity), MLA (medium-low affinity), LA (low affinity) and NA (no affinity). Panels **(A-C)** are adapted from [Imamura et al., 2009](#). **(D-F)** FRET/CFP emission ratios for CFT073  $\Delta fliC$  expressing the different ATeam biosensors (HA, MHA, MLA, LA and NA) in M9 minimal medium supplemented with 0.4% succinate, measured either before (black, unchallenged) or after 5 min **(D)**, 30 min **(E)**, and overnight **(F)** incubation with 1% ethanol (vehicle, dark grey) or 1  $\mu\text{g/mL}$  carbonyl cyanide m-chlorophenyl hydrazone (CCCP, light grey). Red arrows indicate decrease in FRET/CFP emission ratio compared to the unchallenged control.

The ATeam ATP biosensor developed by [Imamura et al., 2009](#) is based on the FRET pairing of cyan and yellow fluorescent proteins (CFP and YFP), flanking the epsilon subunit of *Bacillus subtilis*  $F_0F_1$  ATP synthase, which binds ATP with a high specificity (**Figure 2.2A**). It exists as a series of five indicators with different affinities for ATP, obtained through modification of the ATP-binding residues of the ATP synthase, and labelled HA (high affinity), MHA (medium-high affinity), MLA (medium-low affinity), LA (low affinity) and NA (no affinity) in order of decreasing affinity (**Figure 2.2B,C**). To find out which reporter was appropriate for real-time monitoring of ATP levels in UPEC, we cloned the five constructs into CFT073  $\Delta fliC$  using the pZA32 backbone already described. We then grew the different strains in M9 minimal medium supplemented with 0.4% succinate, a non-fermentable carbon source, so as to restrict ATP production to the ATP synthase only. In these conditions, disruption of the proton motive force should lead to rapid ATP depletion inside bacterial cells. Correspondingly, incubation with the proton ionophore carbonyl cyanide m-chlorophenyl hydrazone (CCCP) resulted in measurable decrease of the FRET/CFP emission ratio after 5 minutes for the strain expressing the LA sensor (**Figure 2.2D**), and after 30 minutes for the strain expressing the MLA sensor (**Figure 2.2E**). Both these sensors have an apparent ATP dissociation constant ( $K_d$ ) in the mM range

(**Figure 2.2C**), which is in line with the reported intracellular ATP concentration of 1-5 mM in *E. coli* ([Mempin et al., 2013](#)). On the contrary, no visible decrease in FRET/CFP emission occurred over the course of 30 minutes for strains expressing the high-affinity HA and MHA sensors, whose  $K_d$  is in the  $\mu$ M range (**Figure 2.2C**), but could be seen after overnight incubation (**Figure 2.2F**), presumably as the remaining ATP level falls below that range. Finally, the FRET/CFP emission ratio remained low throughout the experiment for the strain expressing the NA sensor, consistent with its  $K_d > 10$  mM (**Figure 2.2C**). Overall, these results show that the LA and MLA biosensors can be used to quickly and accurately monitor ATP levels in UPEC at the population level.

We next asked whether these FRET biosensors were also suitable for monitoring the ATP status of single bacterial cells over time by time-lapse fluorescence microscopy. We therefore imaged UPEC strains expressing the HA, MLA and NA sensors during growth in M9 succinate and subsequent starvation with phosphate-buffered saline (PBS). Consistent with previous results, UPEC cells expressing the HA and MLA sensors performed measurable amounts of FRET when grown in M9 succinate, as shown by their turquoise color in the left panels of **Figure 2.3A,B**, corresponding to the superposition of the CFP (blue) and FRET (yellow) emission signals. After 4 hours in PBS however, the majority of cells expressing the HA sensor still performed FRET, while most cells expressing the MLA sensor had turned blue, indicating low FRET efficiency due to ATP depletion in these cells (**Figure 2.3A,B**, right panels). UPEC cells expressing the NA sensor remained blue throughout the experiment (**Figure 2.3C**), in accordance with the low ATP affinity of this sensor. Taken together, these results support the use of the MLA biosensor to record changes in UPEC ATP status at the single-cell level.

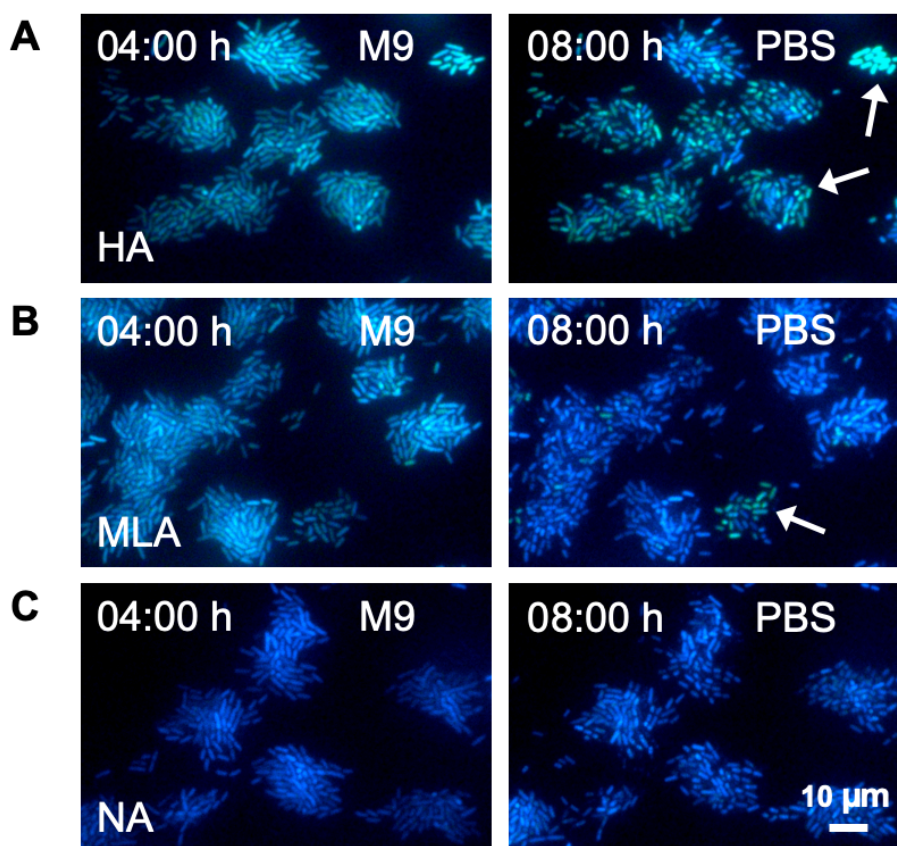


**Figure 2.3: Decrease in FRET efficiency of the ATeam biosensors in CFT073 can be recorded by fluorescence microscopy.** Representative fluorescence images of CFT073  $\Delta fliC$  expressing the high-affinity **(A)**, medium-low-affinity **(B)**, and no-affinity **(C)** ATeam biosensors, taken either 4 h after growth in M9 minimal medium supplemented with 0.4% succinate (M9, left panels) or 4 h after switching to phosphate-buffered saline (PBS, right panels). White arrows indicate examples of bacteria that still perform FRET at the end of the experiment. Bacteria were cultured in the microfluidic device described in **Chapter 4**, and imaged using a color camera upon excitation at 435 nm. Scale bar: 10  $\mu\text{m}$  for all images.

### 2.1.3. Integration of the fluorescent protein into the UPEC chromosome

Despite this encouraging qualitative proof-of-work, getting quantitative single-cell values of the FRET/CFP emission ratio over time proved quite challenging. More specifically, single-cell segmentation was made difficult by the important cell-to-cell variation in fluorescence brightness (**Figure 2.3**). This is directly linked to the pZA32

backbone used for fluorescent protein expression, which maintains between 20 and 30 copies per cell (Lutz et al., 1997). In order to reduce the heterogeneity in ATeam expression, we therefore tried to integrate its coding sequence directly into the UPEC chromosome but were unsuccessful in doing so, presumably because of the high similarity between the CFP and YFP sequences, which can interfere with  $\lambda$  Red recombineering (Datsenko and Wanner, 2000). We thus went back to the original construct with a single fluorescent protein, and integrated the sequence coding for superfolder green fluorescent protein (sfGFP) into the chromosome of CFT073  $\Delta fliC$ , similar to what was recently described by Eshaghi et al., 2016 (see details in 2.2. Materials and methods).

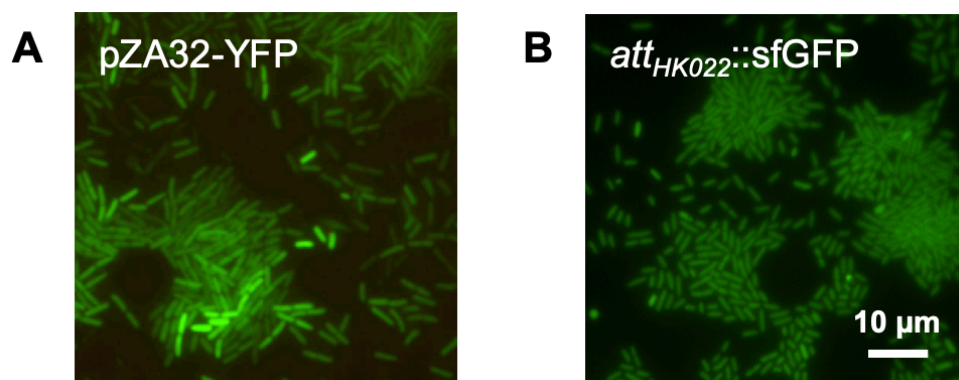


**Figure 2.4: Driving fluorescent protein expression from the chromosome of CFT073 decreases cell-to-cell fluorescence heterogeneity.** CFT073  $\Delta fliC$  expressing either YFP from an episomal plasmid (**A**) or sfGFP from a chromosomal locus (**B**) were cultured using the microfluidic platform described in **Chapter 4**, and imaged on the green fluorescence channel. Scale bar: 10  $\mu$ m for both images.

This strategy allowed us to reduce cell-to-cell fluorescence heterogeneity without too much reduction in brightness, thanks to the use of the brighter sfGFP protein in lieu of YFP (**Figure 2.4**). Quantitative image analysis was also greatly facilitated, whereby

total green fluorescence in an image could serve as a good proxy for the number of bacteria without the need for more complicated single-cell segmentation techniques, which can be rather cumbersome for high-throughput imaging. Overall, giving up on the ATP sensor in favor of sfGFP expression driven from the UPEC chromosome appeared as a necessary compromise between the quantity of information that can be extracted from screening assays and the quality of this information, which is paramount for robust image analysis.

#### **2.1.4. Characterization of reference UPEC strains used in this work**

Considering the successive genetic manipulations required to construct the CFT073  $\Delta fliC$  sfGFP strain, we were concerned about potential off-target recombination events inside the bacterial chromosome, and therefore performed whole-genome sequencing (WGS) of this strain and its two ancestors, CFT073 wt and CFT073  $\Delta fliC$ . This was also motivated by the publicized retraction of three major articles in the field of antibiotic persistence, following the discovery of several prophage contaminants in *E. coli* strains that were central to the studies ([Harms et al., 2017](#); [Goormaghtigh et al., 2018](#)). WGS analysis of our strains revealed no major structural variation, apart from the deletion of a 33-kbp fragment around minute 11 of the bacterial chromosome in strains CFT073  $\Delta fliC$  and CFT073  $\Delta fliC$  sfGFP. This region was previously characterized and corresponds to P2-like prophage  $\Phi$ -CFT073-b0847 ([Lloyd et al., 2007](#)), which got presumably excised from the chromosome during construction of the *fliC* deletion. Notably, this prophage was shown to harbor a gene required for systemic blood-borne infections in both mice and zebrafish, but not for urinary tract infections in mice ([Wiles et al., 2013](#)). It was also shown to be relatively rare in genomes of other

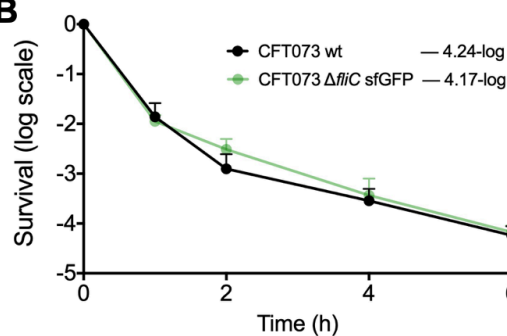
*E. coli* strains, without significant association with pathogenic versus commensal isolates, suggesting acquisition by horizontal gene transfer (Lloyd et al., 2007; Vejborg et al., 2011). Since the focus of the present work is on UPEC-mediated urinary tract infections, we thought that deletion of this prophage was unlikely to invalidate the results of our studies.

We nevertheless verified that phenotypes central to this work were not altered in CFT073  $\Delta fliC$  and CFT073  $\Delta fliC$  sfGFP. More precisely, we did not observe any growth defect in either Luria-Bertani broth (LB) or synthetic human urine (SHU) media compared to CFT073 wt (**Figure 2.5A**). All three strains also had similar susceptibility to three antibiotics commonly used for selection in the lab (ampicillin, kanamycin and chloramphenicol), as well as three antibiotics used for the treatment of urinary tract infections in the clinic (nitrofurantoin, cotrimoxazole and fosfomycin) (**Figure 2.5A**).

**A**

Strain	Doubling time in LB (min)	Doubling time in SHU (min)	AMP MIC in LB ( $\mu\text{g/mL}$ )	KAN MIC in LB ( $\mu\text{g/mL}$ )	CHL MIC in LB ( $\mu\text{g/mL}$ )	NIT MIC in LB ( $\mu\text{g/mL}$ )	SXT MIC in LB ( $\mu\text{g/mL}$ )	FOS MIC in LB ( $\mu\text{g/mL}$ )	FOS MIC in SHU ( $\mu\text{g/mL}$ )	Phage b0847?
CFT073 wt	22.2 $\pm$ 2.0	50.0 $\pm$ 3.6	7.7 $\pm$ 2.7	2.9 $\pm$ 0.5	1.6 $\pm$ 0.2	7.2 $\pm$ 2.2	0.9 $\pm$ 0.2	4.5 $\pm$ 1.9	17.9 $\pm$ 2.5	present
CFT073 $\Delta fliC$	21.8 $\pm$ 2.4	47.1 $\pm$ 4.3	6.2 $\pm$ 0.6	3.3 $\pm$ 0.4	1.5 $\pm$ 0.3	9.3 $\pm$ 1.4	1.7 $\pm$ 0.6	5.2 $\pm$ 1.3	21.3 $\pm$ 1.8	absent
CFT073 wt sfGFP	21.1 $\pm$ 2.8	n.d.	n.d.	n.d.	n.d.	n.d.	n.d.	n.d.	n.d.	present
CFT073 $\Delta fliC$ sfGFP	23.1 $\pm$ 0.7	48.1 $\pm$ 4.6	5.8 $\pm$ 1.2	2.9 $\pm$ 0.9	1.9 $\pm$ 0.5	9.3 $\pm$ 1.0	1.5 $\pm$ 0.3	3.8 $\pm$ 1.5	20.3 $\pm$ 1.0	absent

**B**



**C**

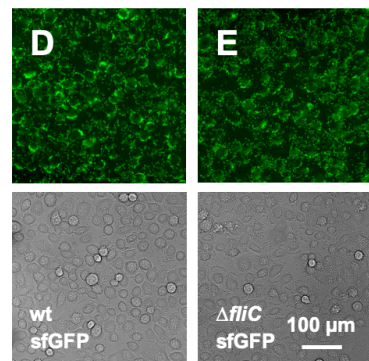
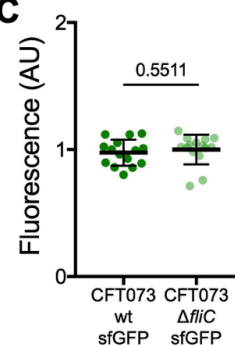


**Figure 2.5: Characterization of UPEC strains used in this work. (A = Table 2.2)** Doubling time in exponential phase and minimum inhibitory concentration (MIC) of various antibiotics in Luria-Bertani broth (LB) and synthetic human urine (SHU) for the four reference UPEC strains used in this work: CFT073 wt (black), CFT073  $\Delta fliC$  (grey), CFT073 wt sfGFP (dark green), and CFT073  $\Delta fliC$  sfGFP (light green). Values are reported as the average  $\pm$  standard deviation of  $n \geq 3$  independent experiments. AMP: ampicillin; KAN: kanamycin; CHL: chloramphenicol; NIT: nitrofurantoin; SXT: cotrimoxazole; FOS: fosfomycin; n.d. not determined. **(B)** Time-kill curves of the indicated UPEC strains in the presence of 5X FOS MIC in SHU (corresponding to 100  $\mu\text{g/mL}$  FOS), recorded by CFU plating on LB agar plates.  $n = 3$  independent experiments; symbols indicate mean; error bars indicate standard deviation; values next to each condition correspond to the extent of bacterial killing at 6 h. **(C)** Quantification of GFP fluorescence after spinfection/washing of 5637 human bladder epithelial cells with the indicated UPEC strains. Data were normalized to CFT073  $\Delta fliC$  sfGFP.  $n = 15$  wells from 3 independent experiments; black lines indicate mean and standard deviation;  $P$ -value was calculated using Welch's t-test. **(D,E)** Corresponding phase-contrast and green fluorescence images for CFT073 wt sfGFP **(D)** and CFT073  $\Delta fliC$  sfGFP **(E)**. Scale bar: 100  $\mu\text{m}$  for all images.

Anticipating on **Chapter 4**, we did not see any difference in persistence to fosfomycin treatment in SHU between CFT073  $\Delta fliC$  sfGFP and CFT073 wt (**Figure 2.5B**). Anticipating on **Chapter 3**, we did not see any difference in bladder epithelial cell adhesion between CFT073  $\Delta fliC$  sfGFP and CFT073 wt sfGFP, using fluorescence as a readout to record host-cell adhesion (**Figure 2.5C-E**). Importantly, the latter assay required the integration of the sequence coding for sfGFP into the wild-type background, after what we verified by PCR that the newly constructed strain still contained the  $\Phi$ -CFT073-b0847 prophage sequence (**Figure 2.5A**). It is also worth noting that the results presented in **Figure 2.5B,C** rule out any involvement of the *fliC* gene in the phenotypes being assessed, namely persistence to fosfomycin in SHU and bladder epithelial cell adhesion.



### 2.1.5. Short conclusion and outlook

Based on these results, we used the CFT073  $\Delta fliC$  sfGFP strain (hereafter referred to as simply  $\Delta fliC$ ) as the parental strain for transposon mutagenesis (see details in **2.2. Materials and methods**). Even though we observed no difference between this parental strain and the wild-type strain in phenotypes central to this work, care should be taken to properly construct unmarked deletions in both backgrounds once mutants of interest are identified, so as to rule out the involvement of *fliC* in the altered phenotypes. However, this shortcoming of the library is largely outweighed by the benefits of using a non-flagellated strain which, combined with constitutive sfGFP expression from the bacterial chromosome, offers great capabilities for high-content screening with robust image analysis and therefore easy identification of mutants with aberrant phenotypes.

## 2.2. Materials and methods

### 2.2.1. Plasmids and primers

Plasmids and primers used in this chapter are listed in **Tables 5.2 and 5.3**.

### 2.2.2. Bacterial culture conditions

The UPEC CFT073 strain was originally isolated from a patient with bacteremia of urinary tract origin ([Mobley et al., 1990](#)) and procured from ATCC (#700928). CFT073



wild-type and mutant strains were inoculated from frozen glycerol stocks and cultured overnight for 16 h ( $\pm$  1 h) at 37°C with shaking at 170 rpm in either LB Luria medium (Sigma) or, for experiments with ATP sensors, in M9 minimal medium consisting of 1X M9 salts (Sigma), 2 mM MgSO<sub>4</sub> and 0.1 mM CaCl<sub>2</sub> supplemented with 0.4% sodium succinate. When required, media were supplemented with 100 µg/mL ampicillin (Sigma), 50 µg/mL kanamycin (Sigma) or 25 µg/mL chloramphenicol (Sigma).

### 2.2.3. Construction of the CFT073 $\Delta$ *fliC* strain

The *fliC* locus in CFT073 (between nucleotides 2,151,497 and 2,153,284) was deleted using the  $\lambda$  Red recombineering system ([Datsenko and Wanner, 2000](#)). Briefly, CFT073 was first transformed with plasmid pKD46 to express the  $\lambda$  Red recombinase, then with the *kan<sup>R</sup>* resistance cassette amplified from plasmid pKD4 using primers *fliC\_KO\_F* and *fliC\_KO\_R*. Successful chromosomal recombination was confirmed by PCR using primers *fliC\_F* and *fliC\_R*, and the *kan<sup>R</sup>* resistance cassette was removed using plasmid pCP20 encoding the FLP recombinase. Loss of swimming motility was assessed by soft-agar assay, as previously described ([Lane et al., 2005](#)).

### 2.2.4. Construction of the ATP reporter strains

Plasmids pRSET-AT3.10, pRSET-AT3.10<sup>MGK</sup>, pRSET-AT1.03<sup>YEMK</sup>, pRSET-AT1.03 and pRSET-AT1.03<sup>KK</sup> ([Imamura et al., 2009](#)) were used as templates for PCR amplification of the different ATP sensor sequences with primers *AT\_F* and *AT\_R*. PCR products were digested with HindIII and SphI and ligated into the pZA32 backbone downstream of the P<sub>LacO-1</sub> promoter. pZA32 plasmids containing the

sequences of the ATP sensors were then electroporated into CFT073  $\Delta fliC$  and transformants were selected on LB agar plates supplemented with chloramphenicol.

#### **2.2.5. FRET measurements in batch**

CFT073  $\Delta fliC$  strains expressing the different ATP sensors were grown in M9 succinate to mid-exponential phase ( $OD_{600} = 0.3-0.4$ ) then concentrated 10 times and aliquoted in three triplicates of wells in a 96-well plate. One triplicate was left unchallenged, one was treated with 1% ethanol (vehicle control) and one with 1  $\mu\text{g/mL}$  CCCP, after which the plate was incubated at 37°C with shaking at 170 rpm. FRET/CFP emission ratios were recorded every 5 minutes using a fluorescence plate reader (Tecan) and calculated by dividing the signal for FRET emission at 527 nm by the signal for CFP emission at 475 nm, both measured upon excitation at 435 nm. Measurements were normalized by the  $OD_{600}$  in each well.

#### **2.2.6. FRET measurements by fluorescence microscopy**

CFT073  $\Delta fliC$  strains expressing the AT3.10, AT1.03<sup>YEMK</sup> and AT1.03<sup>KK</sup> ATP sensors were grown in M9 succinate to mid-exponential phase ( $OD_{600} = 0.3-0.4$ ) then injected each into one section of the microfluidic device described in **Figure 4.1**. Bacteria were grown for four more hours in M9 succinate, after which medium supply was switched to PBS. Fluorescence images of selected microchambers were recorded every 20 minutes using a 60X oil objective (NA = 1.4, #MRD31605, Nikon Instruments) and a color camera (DS-Fi3, Nikon Instruments) upon excitation at 435 nm (for precise methods on microfluidic chip handling, please refer to **Section 4.3**).

### 2.2.7. Integration of the sfGFP sequence into the chromosome of CFT073

The sfGFP sequence was introduced under control of a strong  $P_{\sigma 70}$  promoter at the chromosomal *att<sub>HK022</sub>* site (between nucleotides 1,090,927 and 1,090,928) of CFT073 wt and  $\Delta fliC$  using a recently described method (Eshaghi et al., 2016). Briefly, the *kan<sup>R</sup>-P<sub>RhaB</sub>-relE* toxin cassette was amplified from plasmid pSLC217 using primers P4 and P5 and integrated into the bacterial chromosome using  $\lambda$  Red recombineering. Primers P6 and P7 were then used to amplify the sfGFP-containing fragment from plasmid pSLC293, and these PCR amplicons were used to replace the *kan<sup>R</sup>-P<sub>RhaB</sub>-relE* toxin cassette by  $\lambda$  Red recombineering with negative selection on M9 agar (Sigma) supplemented with 2% L-rhamnose (Sigma). Successful recombination at each step was confirmed by PCR using primers attHK\_F and attHK\_R.

### 2.2.8. Whole-genome sequencing of CFT073 reference strains

Genomic DNA (gDNA) was extracted from 2 mL late-exponential phase ( $OD_{600} = 1$ ) LB cultures of CFT073 wt,  $\Delta fliC$  and  $\Delta fliC$  sfGFP using the Genomic-tip 20/G extraction kit (QIAGEN) according to the manufacturer's instructions. The amount of DNA was quantified using a Qubit® fluorometer (Invitrogen) and its quality assessed by Fragment Analyzer (Advanced Analytical Technologies). Genomic library preparation and sequencing were then performed by the Genomic Technologies Facility (GTF) of the University of Lausanne. Briefly, 1  $\mu$ g of gDNA was fragmented with a g-TUBE® shearing device (Covaris) and concentrated using the PacBio® AMPure kit (Pacific Biosciences). Sheared DNA was then used to prepare a SMRTbell library using the PacBio® SMRTbell Template Prep kit (Pacific Biosciences). The resulting library was

size-selected for molecules larger than 8 kb using a BluePippin system (Sage Science), and sequenced using a SMRT cell on a PacBio® RSII sequencer (Pacific Biosciences). Generated genome sequences were aligned to the reference genome of CFT073 using Mauve ([Darling et al., 2004](#)).

#### **2.2.9. PCR confirmation of the presence of the $\Phi$ -CFT073-b0847 prophage**

Strains to be tested were streaked on LB agar plates. A single colony was boiled for 10 minutes in 50  $\mu$ L water and 1  $\mu$ L was used as template in a standard 25- $\mu$ L Q5® PCR reaction (New England Biolabs) using primers GenIsland\_F and GenIsland\_R and 30 cycles at 67°C with a 30-sec extension time. PCR amplicons were analysed on a 1% agarose gel stained with SYBR® Safe DNA Gel Stain (Invitrogen), and the presence of the  $\Phi$ -CFT073-b0847 prophage sequence confirmed by a 400 bp-band. Results for the different strains tested are reported in **Figure 2.5A**.

#### **2.2.10. Construction of the CFT073 $\Delta$ *fliC* sfGFP transposon insertion library**

Tn5 transposon insertion mutants were generated in the CFT073  $\Delta$ *fliC* sfGFP strain using the EZ-Tn5 transposome kit (Epicentre). Briefly, bacteria were electroporated with transposome complexes and allowed to recover in SOC broth for 1 h at 37°C / 170 rpm prior to plating on LB agar plates supplemented with kanamycin and incubation overnight at 37°C. A total of 17,600 mutants was obtained, from which 8,184 were picked, grown overnight in LB kanamycin, added with 15% glycerol (Fisher Chemical) and archived in 96-well plates.

### **3. High-content screening identifies a critical role for P pili in early adhesion of UPEC to bladder cells**

In this chapter, we applied the transposon insertion library previously constructed to screen for UPEC mutants with defects in early adhesion to human bladder epithelial cells, using a high-throughput fluorescence microscopy-based setup.

Keywords: uropathogenic *Escherichia coli* (UPEC); bladder epithelial cells; high-content screening (HCS); bacterial adhesion; P pili; type 1 pili; scanning electron microscopy (SEM); mass spectrometry (MS); surface proteomics

## **3.1. Results**

### **3.1.1. A fluorescence microscopy-based assay to measure early adhesion of UPEC to bladder cells**

We developed a high-throughput fluorescence microscopy-based assay to monitor early adhesion of UPEC to human bladder epithelial cells (**Figure 3.1A**). As previously described, the clinical UPEC isolate CFT073 was engineered to express sfGFP from a strong constitutive promoter integrated on the chromosome and swimming motility was eliminated by deleting the *flhC* gene encoding flagellin, in order to facilitate imaging. Human 5637 bladder epithelial cells were grown in 96-well plates and spininfected with bacteria at a multiplicity-of-infection (MOI) of 200:1. In order to focus on the initial stages of bacterial adhesion, rather than downstream events such as

invasion and intracellular growth, plates were incubated at 37°C for 20 minutes then washed to remove non-adherent bacteria and immediately imaged (**Figure 3.1A**). Automated microscopy was used to measure GFP fluorescence in each well as a proxy for the number of adherent bacteria, and the integrity of the epithelial cell layer was simultaneously assessed on the phase-contrast channel.

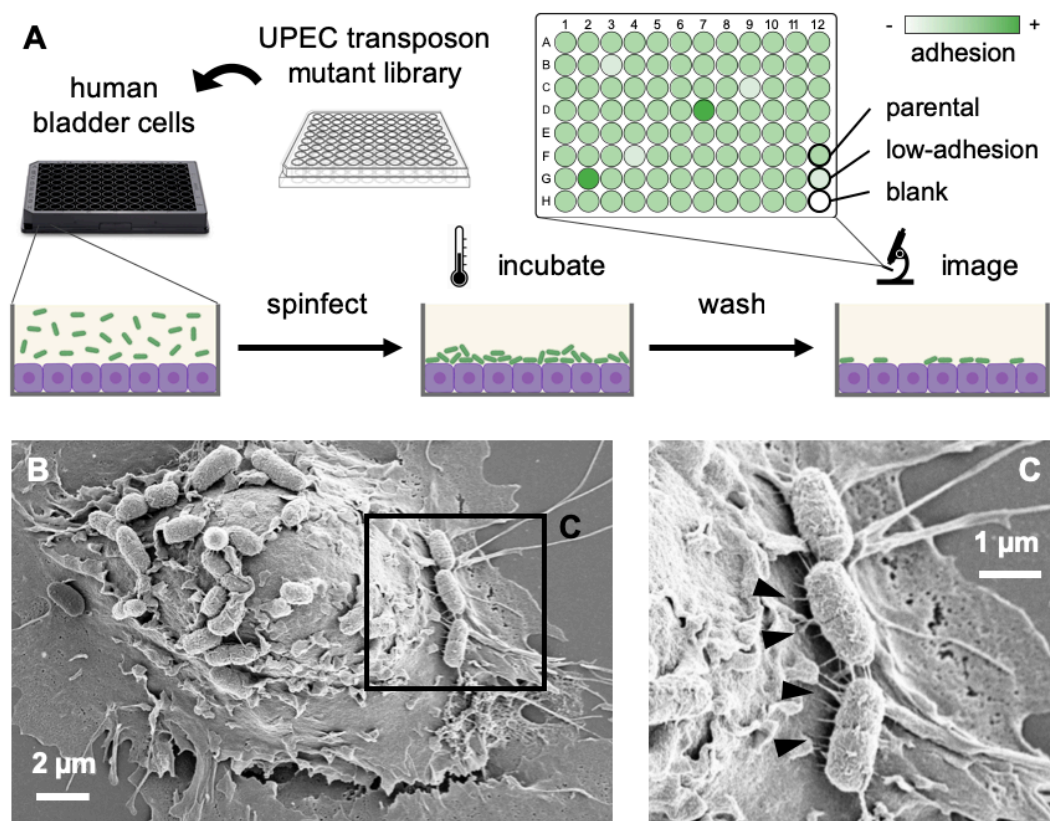


**Figure 3.1: A high-content screening assay to measure early adhesion of UPEC to bladder epithelial cells.** (A) Schematic of the high-content screening assay. Confluent 5637 human bladder epithelial cells in 96-well plates were spininfected with UPEC transposon mutants constructed in the parental strain CFT073  $\Delta fliC$  sfGFP (hereafter referred to as  $\Delta fliC$ ). Plates were incubated, washed to remove non-adherent bacteria, and imaged on phase-contrast and green fluorescence channels using a high-throughput microscope. Quantification of GFP fluorescence served as a proxy for the number of adherent bacteria in each well. Each plate comprised 93 transposon mutants, the  $\Delta fliC$  parental strain, a  $\Delta fliC$  *dkcA*-Tn low-adhesion strain, and a blank well without bacteria. A total of 8,184 transposon mutants was

screened (see detailed workflow in **Figure 3.4**). **(B)** Scanning electron micrograph showing the interaction between the  $\Delta fliC$  parental strain and bladder epithelial cells. Scale bar: 2  $\mu\text{m}$ . **(C)** Zoom of the boxed area in panel **(B)** showing that bacterial adhesion to bladder cells is mediated by pili, indicated by black arrowheads. Scale bar: 1  $\mu\text{m}$ .

We confirmed by scanning electron microscopy (SEM) that bacteria adhered to the surface of bladder cells using pili under the conditions of our assay (**Figure 3.1B,C**). We also confirmed by immunofluorescence that 5637 bladder epithelial cells expressed cytokeratin 8 (CK8) and uroplakin IIIa (UPK3A), which are both markers for superficial umbrella cells of the bladder urothelium (**Figure 3.2**). Importantly, uroplakin mediates UPEC infection of the bladder through its terminal mannosyl moieties, which serve as receptors for type 1 pili ([Wu et al., 1996](#); [Zhou et al., 2001](#); [Thumbikat et al., 2009](#)). We later confirm by qRT-PCR and mass spectrometry that UPEC expressed type 1 pili under the conditions we used for bacterial culture, consistent with previous reports ([Snyder et al., 2004](#); **Figure 3.14**).

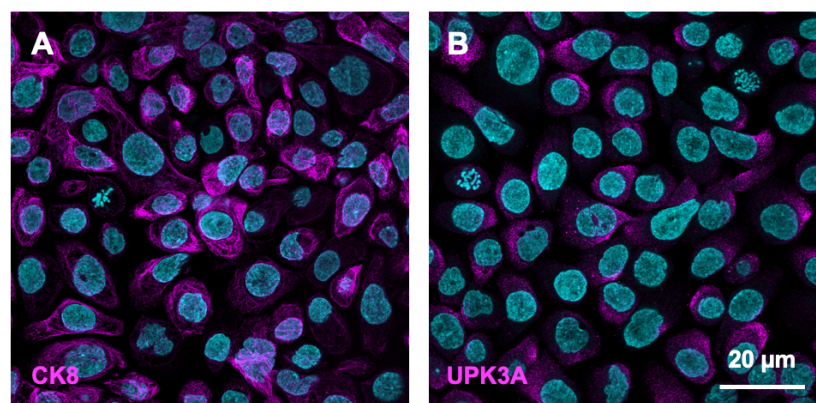


**Figure 3.2: 5637 bladder epithelial cells express markers specific to umbrella cells.** Immunofluorescence staining of 5637 human bladder epithelial cells for the umbrella cell-specific markers cytokeratin 8 (CK8) **(A)**, and uroplakin IIIa (UPK3A) **(B)**, shown in both cases in magenta. Cell nuclei were labelled with DAPI, shown in cyan. Images are a courtesy of lab colleague Kunal Sharma. Scale bar: 20  $\mu\text{m}$  for both images.



### 3.1.2. High-content screening identifies UPEC mutants with altered adhesion to bladder cells

The CFT073  $\Delta fliC$  sfGFP strain (hereafter  $\Delta fliC$ ) served as the parental strain for transposon mutagenesis. A library of 8,184 transposon mutants was screened following the procedure outlined in **Figure 3.1A**, corresponding to about 80% saturation of the genome of CFT073, which is 5.2 Mb in length and has 5,533 annotated protein-coding genes (Zilsel et al., 1992; Welch et al., 2002). As controls in the screening procedure, we used the  $\Delta fliC$  parental strain (**Figure 3.3A,D,E**), a  $\Delta fliC dksA$ -Tn5 low-adhesion strain that we identified at an early stage of the screening process (**Figure 3.3B,D,F**), as well as uninfected bladder cells (**Figure 3.3C**).

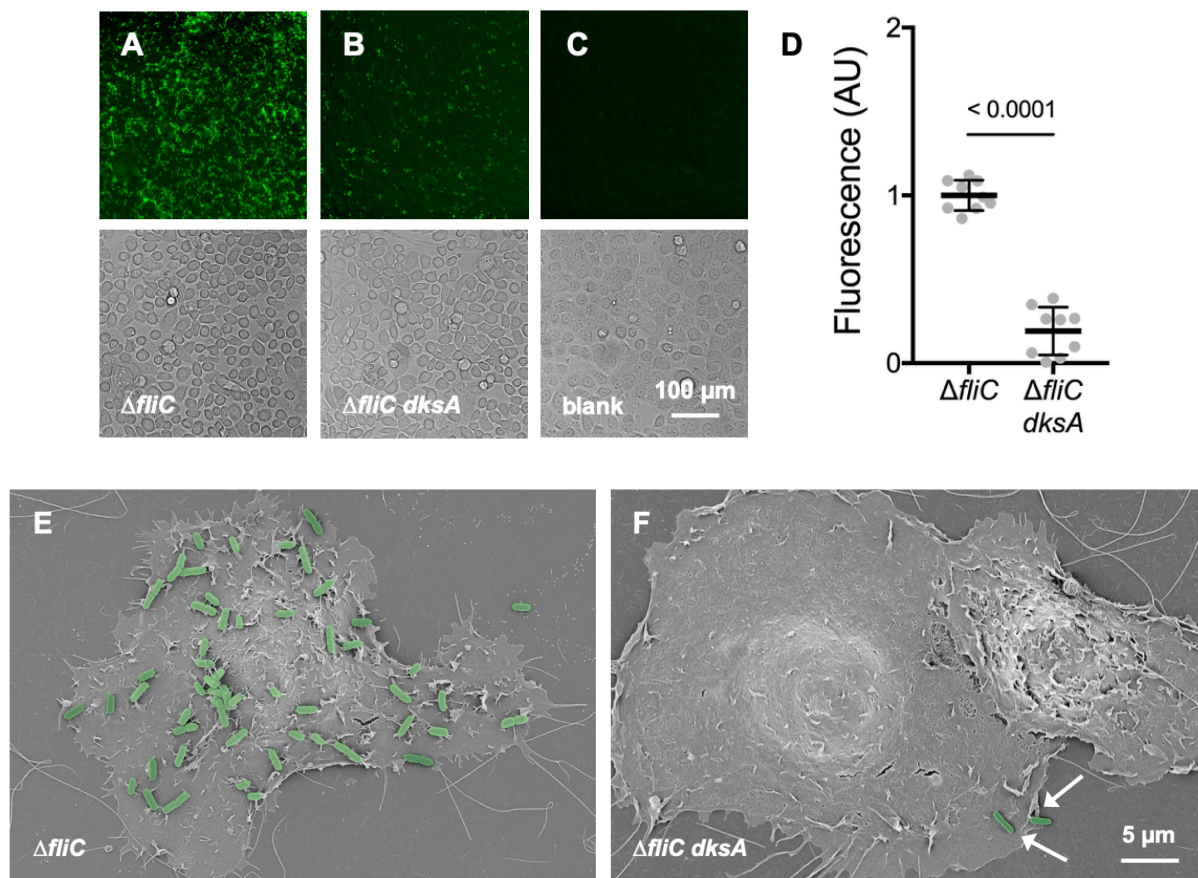




**Figure 3.3: Characterization of control UPEC strains used in the screen.** (A-C) Representative images of bladder epithelial cells spininfected with the  $\Delta fliC$  parental strain (A),  $\Delta fliC$  *dksA*-Tn low-adhesion strain (B), as well as an uninfected control (C), imaged on the green fluorescence channel to quantify adherent bacteria (upper panels) or phase-contrast channel to confirm the integrity of the epithelial cell layer (lower panels). Scale bar: 100  $\mu$ m for all images. (D) Quantification of GFP fluorescence for each condition. Data were normalized to the  $\Delta fliC$  parental strain.  $n = 9$  wells from 3 independent experiments; black lines indicate mean and standard deviation;  $P$ -value was calculated using Welch's t-test. (E,F) Scanning electron micrographs showing bladder epithelial cells spininfected with the  $\Delta fliC$  parental strain (E) or  $\Delta fliC$  *dksA*-Tn low-adhesion strain (F). Bacteria are pseudo-colored in green and indicated by white arrows in (F). Scale bar: 5  $\mu$ m for both images.

Mutants that displayed decreased (Figure 3.5B,D) or increased (Figure 3.5C,D) adhesion to bladder cells compared to the  $\Delta fliC$  parental strain (Figure 3.5A,D) were selected using an automated three-step screening procedure (Figure 3.4). This procedure resulted in the identification and confirmation of 82 low-adhesion mutants (1.0% of the total screened), representing 60 genes, and 54 high-adhesion mutants (0.7%), representing 32 genes (Table 5.1). The positions of the transposon insertion sites within the genome of CFT073 were scattered throughout the chromosome with no obvious “hot spots” or “cold spots” (Figure 3.6).

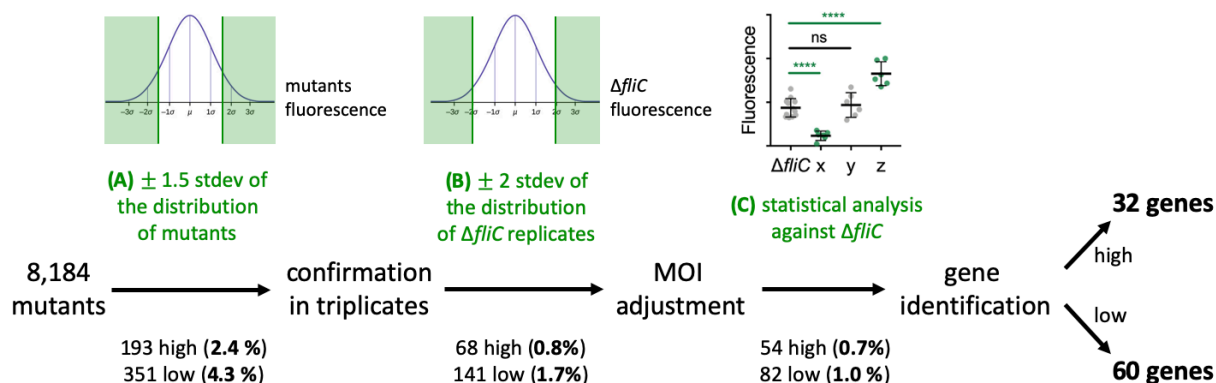


**Figure 3.4: Screening procedure and data analysis pipeline.** (A) A library of 8,184 UPEC transposon mutants, corresponding to 88 x 96-well plates, was screened to identify mutants exhibiting altered adhesion to bladder epithelial cells using the microscopy-based method described in **Figure 3.1**. For each 96-well plate, the mean GFP fluorescence in each well after spinfection/washing was recorded and mutants with values more than 1.5 standard deviations from the average fluorescence on the plate were selected for retesting. Mutants that did not grow were discarded. (B) Candidate mutants were arrayed in triplicates on a 96-well plate along with 30 replicates of the  $\Delta fliC$  parental strain and screened following the same procedure as in (A). Mutants with values more than 2 standard deviations from the average fluorescence of the  $\Delta fliC$  parental strain were retained. (C) Overnight cultures of candidate mutants were adjusted to the same final OD<sub>600</sub> value to ensure the same multiplicity-of-infection (MOI) for each strain, arrayed in 6 replicates per strain on a 96-well plate along with 6 replicates of the  $\Delta fliC$  parental strain, and screened following the same procedure as in (A). For each mutant, the distribution of GFP fluorescence values after spinfection/washing was compared to the distribution for the  $\Delta fliC$  parental strain using Welch's t-test and strains with  $P < 0.05$  were selected for further analysis. Disrupted genes were identified as described in **3.3. Materials and methods**.

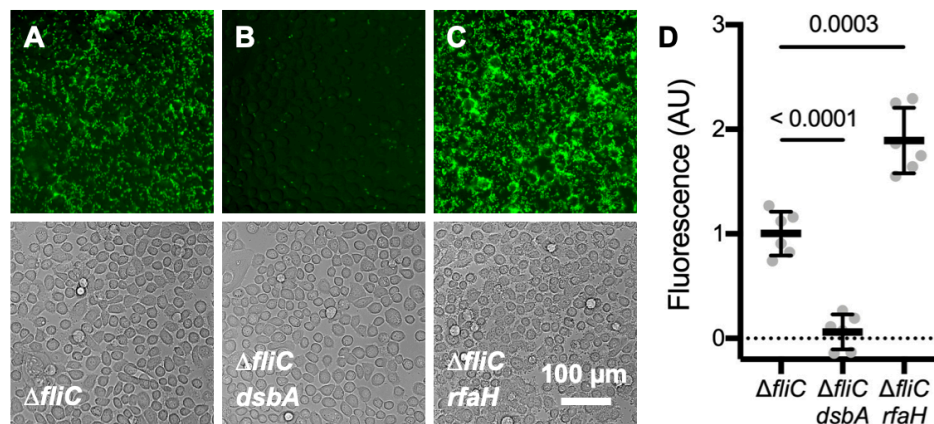


**Figure 3.5: Examples of UPEC mutants with altered adhesion to bladder epithelial cells identified through the screen.** (A-C) Representative images of bladder epithelial cells spininfected with the  $\Delta fliC$  parental strain (A),  $\Delta fliC dsbA$ -Tn low-adhesion mutant (B), and  $\Delta fliC rfaH$ -Tn high-adhesion mutant (C). Scale bar: 100  $\mu m$  for all images. (D) Quantification of GFP fluorescence for each condition. Data were normalized to the  $\Delta fliC$  parental strain.  $n = 6$  wells per strain; black lines indicate mean and standard deviation;  $P$ -values were calculated using Welch's t-test.

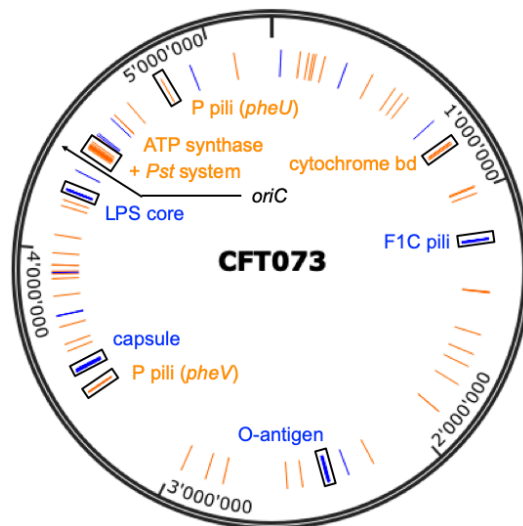


**Figure 3.6: Chromosomal transposon insertion sites of UPEC mutants with altered adhesion to bladder epithelial cells.** Map of the chromosome of CFT073 showing the position of low-adhesion transposon “hits” in orange and high-adhesion transposon “hits” in blue. Hits that are found within the same operon are framed in black and the function of the operon is indicated. The black arrow indicates the position of the origin of replication *oriC*.

### 3.1.3. Genes that contribute positively or negatively to early adhesion of UPEC to bladder cells

In order to establish pathways involved in early adhesion of UPEC to bladder epithelial cells, genes identified in the screen were grouped according to their KEGG (Kyoto Encyclopedia of Genes and Genomes) classification. We focused in particular on genes that were “hit” several times throughout the screen or that belong to the same operon (**Figure 3.7**). Most of the transposon insertions corresponding to high-adhesion phenotypes clustered within genes involved in biogenesis of the cell envelope (**Figure 3.7**, top panel). More particularly, operons linked to the synthesis of the lipopolysaccharide (LPS) O-antigen (**Figure 3.7A**), the LPS core (**Figure 3.7B**), and the capsule layer (**Figure 3.7C**) were repeatedly identified, possibly because trimming of these outward-facing surface structures lead to better pili display.

Interestingly, we also identified six insertions within the operon coding for the synthesis of F1C pili (**Figure 3.7D**), which are most closely related to type 1 pili, sharing up to 64% amino acid sequence identity at the protein level (**Table 1.1**). Identification of high-adhesion hits in the F1C pili locus may suggest cross-regulation between different pili operons ([Holden and Gally, 2004](#)), resulting in upregulation of other adhesins in the absence of F1C pili (see more details in **Section 3.1.6**).

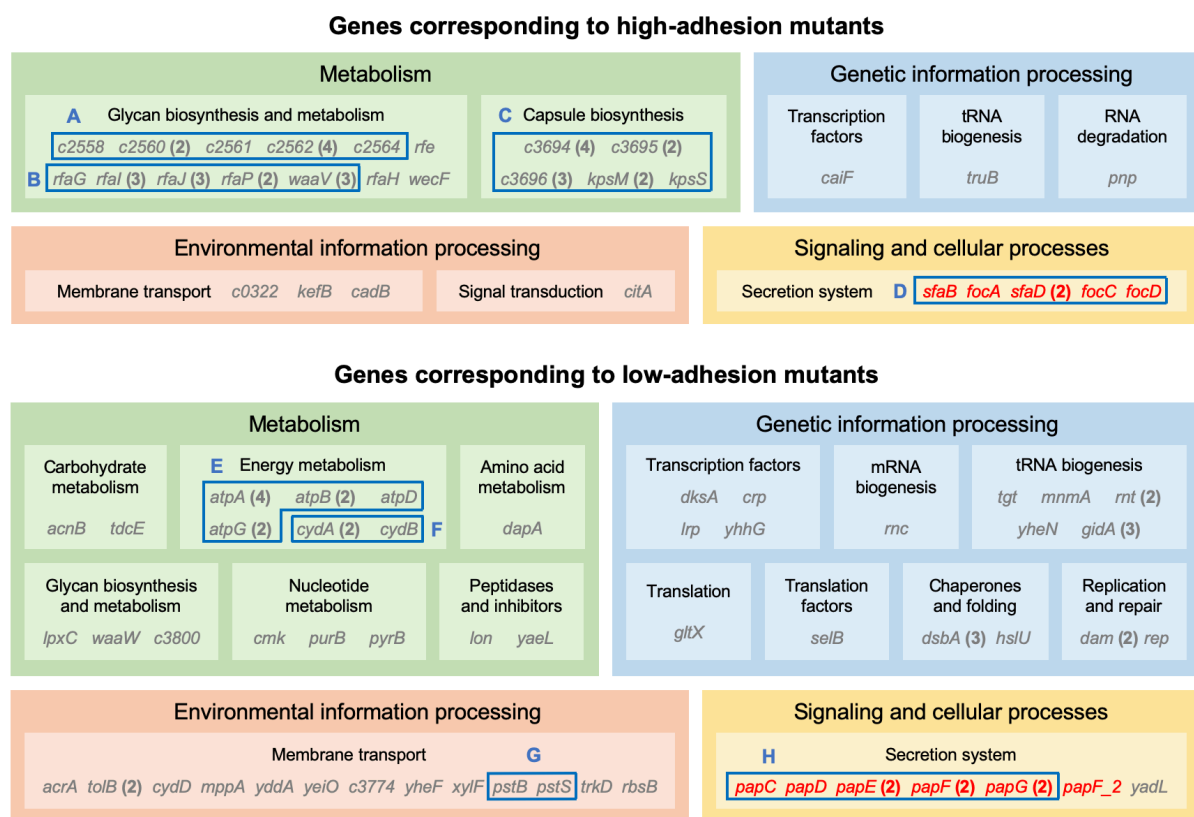


**Figure 3.7: Early adhesion of UPEC to bladder epithelial cells is differentially regulated by multiple genes.** Genes disrupted in UPEC transposon mutants with increased (upper panel) or decreased (lower panel) adhesion to bladder epithelial cells grouped according to their KEGG classification. Genes that do not have a KEGG annotation are listed in **Table 5.1**. Numbers in parentheses indicate the number of independent transposon “hits” obtained in the corresponding genes. Genes that belong to the same operon are framed in blue: **(A)** O-antigen synthesis; **(B)** LPS core synthesis; **(C)** capsule synthesis; **(D)** F1C pili synthesis; **(E)** ATP synthase; **(F)** cytochrome bd; **(G)** Pst system; **(H)** P pili synthesis (*pheV* operon). Genes that are studied further in this work are indicated in red.

A number of low-adhesion mutants were linked to bacterial metabolism (**Figure 3.7**, bottom panel), especially energy metabolism, with several transposon hits identified within the operons coding for the components of the ATP synthase (**Figure 3.7E**) and the cytochrome bd (**Figure 3.7F**). We also identified genes associated with tRNA biogenesis and membrane transport, including the Pst ABC transporter for inorganic phosphate (**Figure 3.7G**). Surprisingly, we did not identify a single hit directly linked to the synthesis of type 1 pili, which are thought to be the main mediators of UPEC adhesion to bladder cells ([Martinez et al., 2000](#); [Hung et al., 2002](#)). However, we identified nine independent transposon insertions within genes coding for the synthesis of P pili (**Figure 3.7H**), which are usually thought to be important primarily for colonization of the kidney in cases of pyelonephritis ([Roberts et al., 1994](#); [Dodson et al., 2001](#); [Johnson et al., 2005](#); [Lane et al., 2007](#); [Lillington et al., 2014](#)). Since the results from our screen identified a key role for P pili, but not for type 1 pili, in early adhesion of UPEC to bladder epithelial cells, we performed a series of additional assays to dissect the contribution of both types of pili to bacterial adhesion.

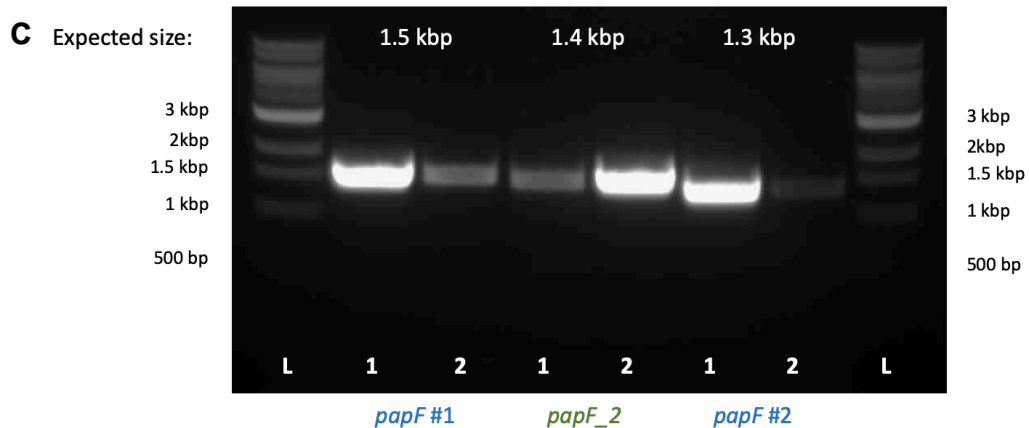
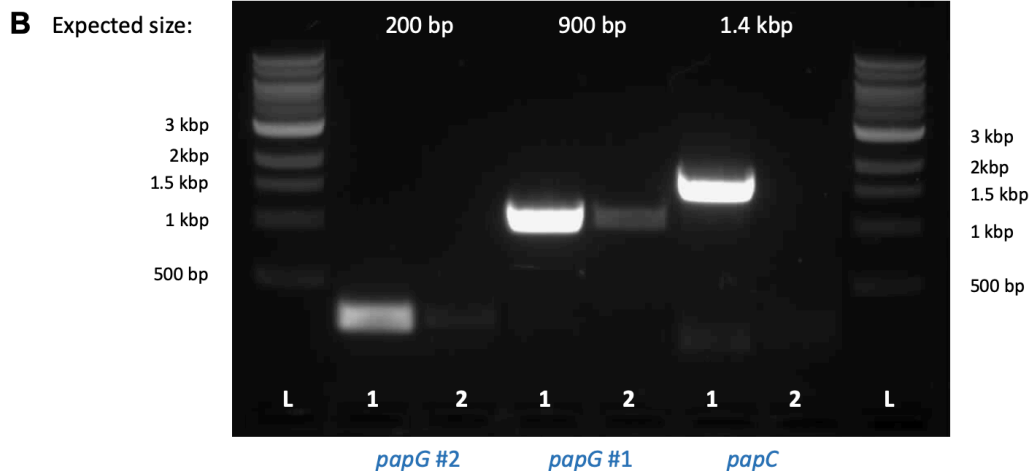
#### **3.1.4. P pili are key mediators of early adhesion of UPEC to bladder cells**

CFT073 encodes two P pili operons that are located on pathogenicity islands next to the tRNA genes *pheV* (hereafter referred to as the *pap1* operon) and *pheU* (hereafter referred to as the *pap2* operon) ([Welch et al., 2002](#); [Lloyd et al., 2007](#)). Both operons have the same organization (**Figure 3.9A**). Because of the high degree of identity between corresponding genes of the two *pap* operons (**Figure 3.8A**), the single-primer PCR protocol we used for mutant identification failed to assign transposon insertions to either *pap1* or *pap2*. We therefore developed a PCR assay that takes advantage

of the distinct DNA sequences flanking the two operons, as explained in **3.3. Materials and methods**. Among the nine transposon insertions identified within P pili genes, eight were assigned to *pap1* and only one to *pap2*, more precisely to the sequence coding for *papF\_2* (**Figure 3.8B-D and Figure 3.9A**). All nine insertions led to an intermediate yet significant low-adhesion phenotype, which was most pronounced for insertions in *papF* and *papF\_2* (**Figure 3.9B-L**).

**A**

	<i>papA</i> vs <i>papA_2</i>	<i>papH</i> vs <i>papH_2</i>	<i>papC</i> vs <i>papC_2</i>	<i>papD</i> vs <i>papD_2</i>	<i>papJ</i> vs <i>papJ_2</i>	<i>papK</i> vs <i>papK_2</i>	<i>papE</i> vs <i>papE_2</i>	<i>papF</i> vs <i>papF_2</i>	<i>papG</i> vs <i>papG_2</i>
% DNA identity	77.76 %	99.49 %	99.88 %	100.00 %	100.00 %	100.00 %	100.00 %	100.00 %	99.60 %
% aa identity	77.50 %	100.00 %	100.00 %	100.00 %	100.00 %	100.00 %	100.00 %	100.00 %	98.81 %



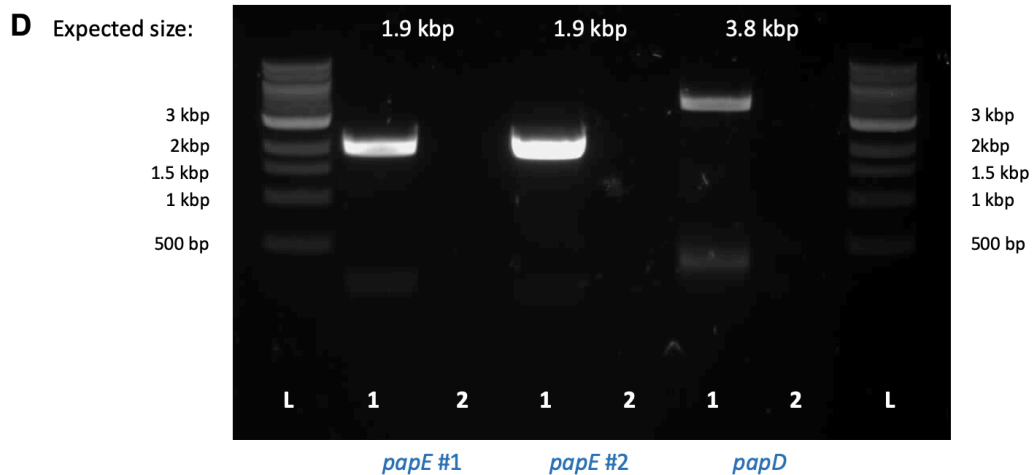
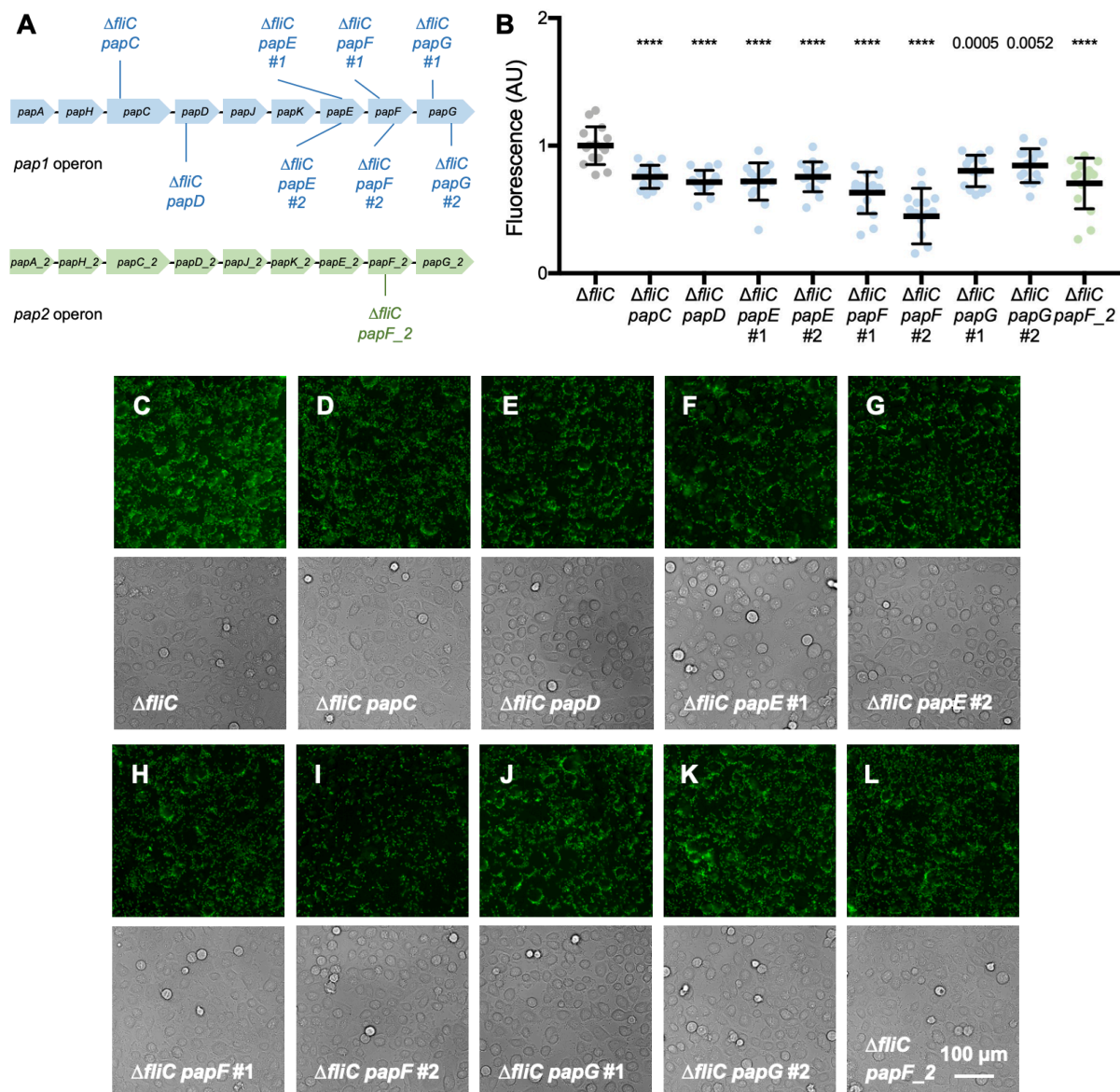


**Figure 3.8: Assignment of P pili transposon insertions to the *pap1* or *pap2* operons. (A = Table 3.1)** Sequence similarity between *pap1* and *pap2* operons. The percentage of DNA sequence identity between homologous genes was calculated using nBlast. The percentage of amino acid (aa) sequence identity between homologous proteins was calculated using pBlast. **(B-D)** Images of SYBR<sup>®</sup>-stained agarose gels loaded with PCR amplicons obtained using the assay described in **3.3. Materials and methods**. 1: amplicons obtained with primers specific to the *pap1* operon. 2: amplicons obtained with primers specific to the *pap2* operon. L: 1 kb ladder. The number of base pairs (bp) indicates the expected band size for each transposon insertion. Identification of the gene disrupted in each strain was based on the brightest amplicon band for each primer set (blue, *pap1*; green, *pap2*). When two insertions occurred in the same gene, the most upstream insertion is annotated #1.

**Figure 3.9 (next page): Adhesion phenotypes of P pili transposon mutants. (A)** Position of transposon insertions identified within the two P pili operons of CFT073, according to the results of the PCR assay shown in **Figure 3.8**. Top: *pheV* operon (*pap1*, blue). Bottom: *pheU* operon (*pap2*, green). **(B)** Quantification of GFP fluorescence after spinfection/washing of bladder epithelial cells with the indicated UPEC strains. Data were normalized to the  $\Delta fliC$  parental strain. n = 15 wells from 3 independent experiments; black lines indicate mean and standard deviation; *P*-values were calculated using Welch's t-test comparing mutant strains to the  $\Delta fliC$  parental strain; \*\*\*\* *P* < 0.0001. **(C-L)** Corresponding phase-contrast and green fluorescence images for the  $\Delta fliC$  parental strain **(C)**, and transposon mutants  $\Delta fliC$  *papC*-Tn **(D)**,  $\Delta fliC$  *papD*-Tn **(E)**,  $\Delta fliC$  *papE*-Tn #1 **(F)**,  $\Delta fliC$  *papE*-Tn #2 **(G)**,  $\Delta fliC$  *papF*-Tn #1 **(H)**,  $\Delta fliC$  *papF*-Tn #2 **(I)**,  $\Delta fliC$  *papG*-Tn #1 **(J)**,  $\Delta fliC$  *papG*-Tn #2 **(K)**, and  $\Delta fliC$  *papF\_2*-Tn **(L)**. Scale bar: 100  $\mu$ m for all images.

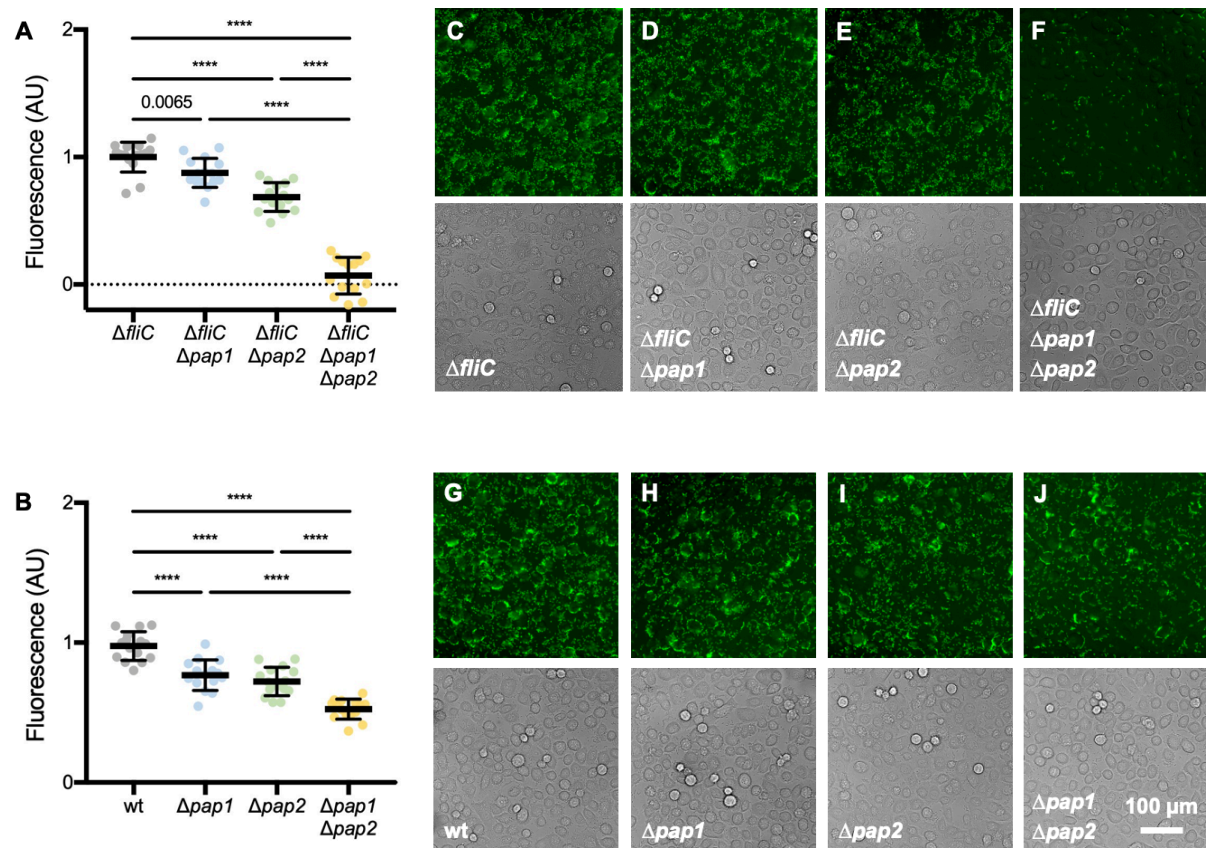




We further assessed the contribution of each *pap* operon to UPEC adhesion by constructing unmarked deletion mutants of *pap1* and *pap2* in both the  $\Delta fliC$  and wild-type backgrounds. Both  $\Delta fliC \Delta pap1$  and  $\Delta fliC \Delta pap2$  had an intermediate but significant low-adhesion phenotype, in agreement with the phenotypes of the corresponding transposon insertion mutants (**Figure 3.10A,C,D,E**). Interestingly, the double *pap* deletion mutant  $\Delta fliC \Delta pap1 \Delta pap2$  showed strongly impaired adhesion that was significantly greater than the defect of either single *pap* deletion mutant (**Figure 3.10A,C,F**), indicating an additive role for *pap1* and *pap2* in adhesion to



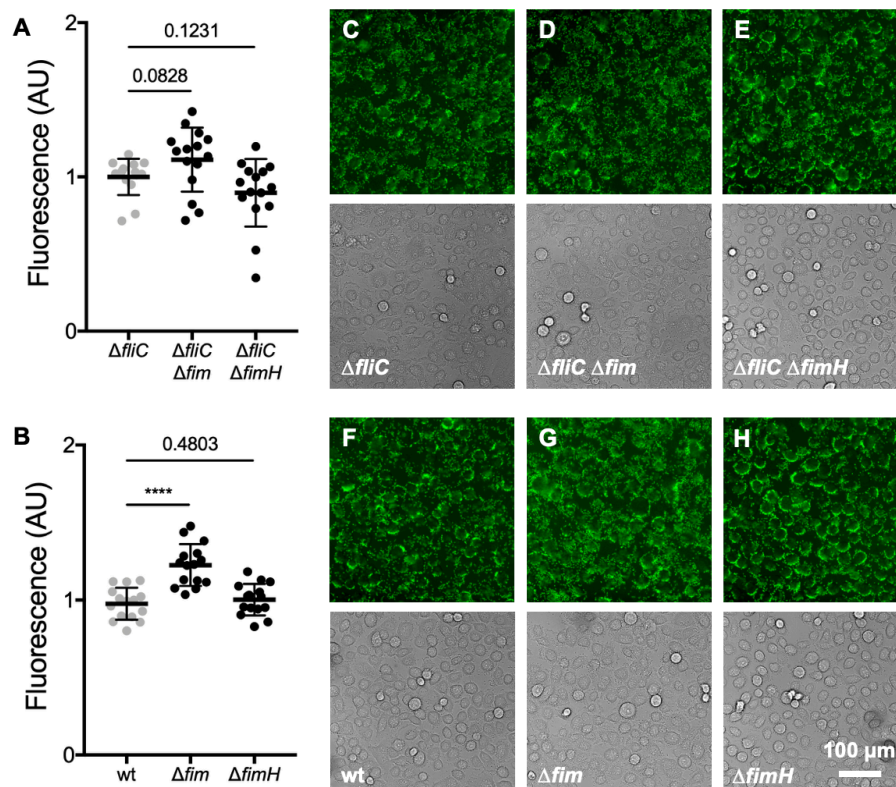
bladder cells. The low-adhesion phenotypes of the  $\Delta fliC$  *pap* mutants were also recapitulated when the single and double *pap* operon deletions were introduced in the wild-type background, thereby confirming that deletion of *fliC* does not affect early adhesion of UPEC to bladder epithelial cells in our assay (**Figure 3.10B,G,H,I,J**).



**Figure 3.10: P pili are key mediators of early adhesion of UPEC to bladder epithelial cells. (A,B)** Quantification of GFP fluorescence after spinfection/washing of bladder epithelial cells with the indicated UPEC strains. Data were normalized to the  $\Delta fliC$  parental strain.  $n = 15$  wells from 3 independent experiments; black lines indicate mean and standard deviation;  $P$ -values were calculated using Welch's t-test; \*\*\*\*  $P < 0.0001$ . **(C-J)** Corresponding phase-contrast and green fluorescence images for  $\Delta fliC$  (C), wild-type (G), single *pap* deletion mutants  $\Delta fliC \Delta pap1$  (D),  $\Delta fliC \Delta pap2$  (E),  $\Delta pap1$  (H), and  $\Delta pap2$  (I), and double *pap* deletion mutants  $\Delta fliC \Delta pap1 \Delta pap2$  (F) and  $\Delta pap1 \Delta pap2$  (J). Scale bar: 100  $\mu m$  for all images.

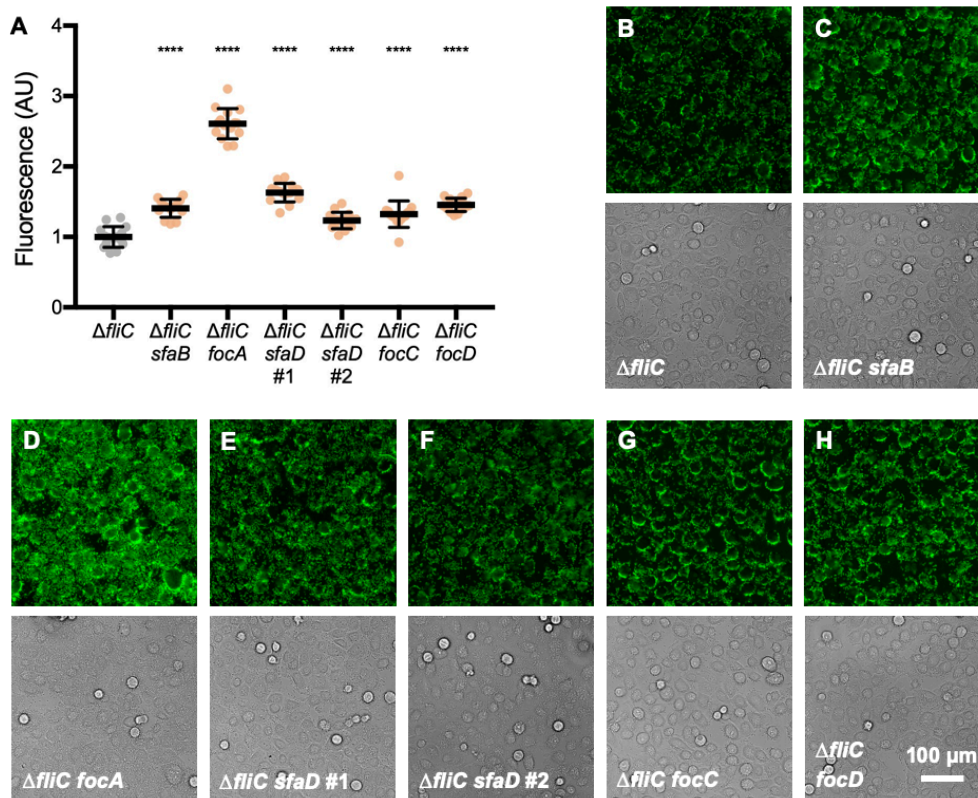
### 3.1.5. Type 1 pili are not essential for early adhesion of UPEC to bladder cells

We next assessed the direct role of type 1 pili in early adhesion of UPEC by constructing unmarked deletions of the entire *fim* operon in both the  $\Delta fliC$  and wild-type backgrounds. Mutants in both backgrounds showed a trend towards a high-adhesion phenotype that was statistically significant in the wild-type background (**Figure 3.11A,C,D,B,F,G**). To avoid the possibility of cross-regulation of other pili operons as a consequence of deleting the entire *fim* operon, we deleted only the adhesin gene *fimH* in both the wild-type and  $\Delta fliC$  backgrounds. Neither strain,  $\Delta fimH$  or  $\Delta fliC \Delta fimH$ , displayed a significant defect in adhesion to bladder epithelial cells (**Figure 3.11A,C,E,B,F,H**). These results therefore confirm that type 1 pili are not essential for early adhesion of UPEC to bladder cells, in agreement with the absence of hits in the *fim* operon in our screen.



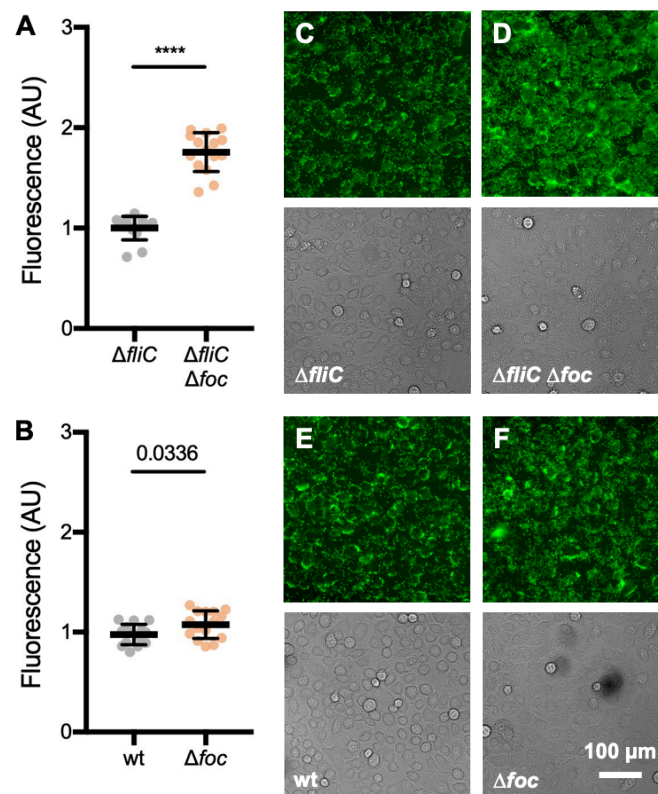
**Figure 3.11: Type 1 pili are not essential for early adhesion of UPEC to bladder epithelial cells.** (A,B) Quantification of GFP fluorescence after spinfection/washing of bladder epithelial cells with the indicated UPEC strains. Data were normalized to the  $\Delta fliC$  parental strain.  $n = 15$  wells from 3 independent experiments; black lines indicate mean and standard deviation;  $P$ -values were calculated using Welch's t-test; \*\*\*\*  $P < 0.0001$ . (C-H) Corresponding phase-contrast and green fluorescence images for  $\Delta fliC$  (C),  $\Delta fliC \Delta fim$  (D),  $\Delta fliC \Delta fimH$  (E), wild-type (F),  $\Delta fim$  (G), and  $\Delta fimH$  (H). Scale bar: 100  $\mu m$  for all images.

### 3.1.6. P pili expression is upregulated in F1C pili-deficient UPEC mutants



**Figure 3.12: Adhesion phenotypes of F1C pili transposon mutants.** (A) Quantification of GFP fluorescence after spinfection/washing of bladder epithelial cells with the indicated UPEC strains. Data were normalized to the  $\Delta fliC$  parental strain.  $n = 15$  wells from 3 independent experiments; black lines indicate mean and standard deviation;  $P$ -values were calculated using Welch's t-test comparing mutant strains to the  $\Delta fliC$  parental strain; \*\*\*\*  $P < 0.0001$ . (B-H) Corresponding phase-contrast and green fluorescence images for the  $\Delta fliC$  parental strain (B),  $\Delta fliC sfaB$ -Tn (C),  $\Delta fliC focA$ -Tn (D),  $\Delta fliC sfaD$ -Tn #1 (E),  $\Delta fliC sfaD$ -Tn #2 (F),  $\Delta fliC focC$ -Tn (G), and  $\Delta fliC focD$ -Tn (H). Scale bar: 100  $\mu m$  for all images.

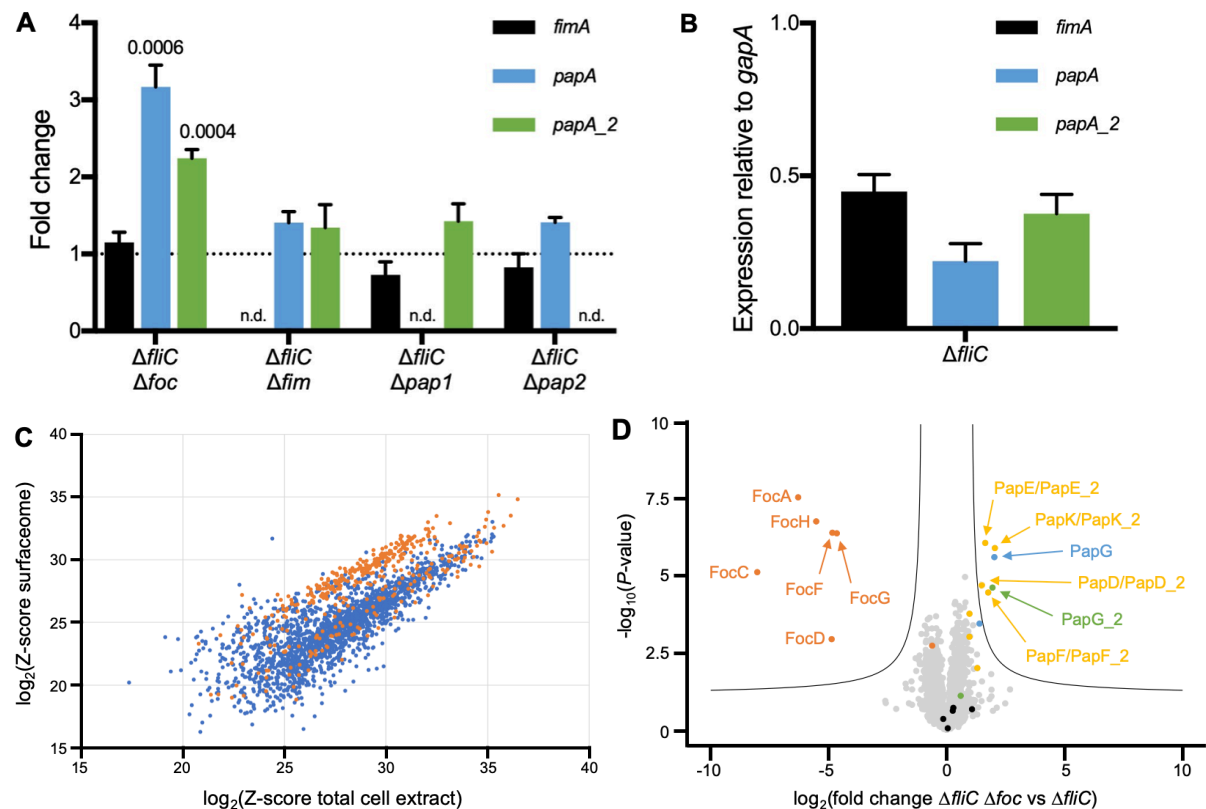
We identified five transposon insertions within effector genes of the F1C pili operon (*focA*, *sfaD*, *focC*, and *focD*) and one insertion in the linked regulatory gene *sfaB*. All insertions led to a significant increase in UPEC adhesion to bladder cells (**Figure 3.12**). This high-adhesion phenotype was recapitulated when we constructed an unmarked deletion mutant of the entire *foc* operon in both the  $\Delta fliC$  background (**Figure 3.13A,C,D**) and wild-type background (**Figure 3.13B,E,F**), although the magnitude of this effect was more modest in the latter. Based on these results, we hypothesized that loss of F1C pili might lead to increased synthesis of P pili, resulting in increased adhesion of the *foc* mutants to bladder epithelial cells.



**Figure 3.13: Adhesion phenotypes of unmarked F1C pili operon deletion mutants. (A,B)** Quantification of GFP fluorescence after spinfection/washing of bladder epithelial cells with the indicated UPEC strains.  $n = 15$  wells from 3 independent experiments; black lines indicate mean and standard deviation;  $P$ -values were calculated using Welch's t-test; \*\*\*\*  $P < 0.0001$ . **(C-F)** Corresponding phase-contrast and green fluorescence images for  $\Delta fliC$  (**B**),  $\Delta fliC \Delta foc$  (**C**), wild-type (**C**), and  $\Delta foc$  (**D**). Scale bar: 100  $\mu m$  for all images.



To test this hypothesis, we measured the expression levels of genes corresponding to the major pilin subunits of type 1 pili (*fimA*), P1 pili (*papA*), and P2 pili (*papA\_2*) in the  $\Delta fliC \Delta foc$  mutant strain. We observed a three-fold upregulation of *papA* expression and a two-fold upregulation of *papA\_2* expression in the  $\Delta fliC \Delta foc$  strain compared to the  $\Delta fliC$  parental strain, while expression of *fimA* was unaffected (**Figure 3.14A**). Considering the high degree of sequence identity between the three genes, especially *papA* and *papA\_2* (**Figure 3.8A**), we confirmed the specificity of our assay by assessing their expression levels in strains deleted for the entire corresponding operons ( $\Delta fim$ ,  $\Delta pap1$ ,  $\Delta pap2$ ). As expected, in each operon deletion mutant, expression of the corresponding pilin gene was abolished while expression of the two other genes remained unchanged (**Figure 3.14A**). In the parental strain, *fimA* and *papA\_2* were expressed at similar levels while expression of *papA* was about 50% lower (**Figure 3.14B**), in agreement with the literature ([Snyder et al., 2004](#)).



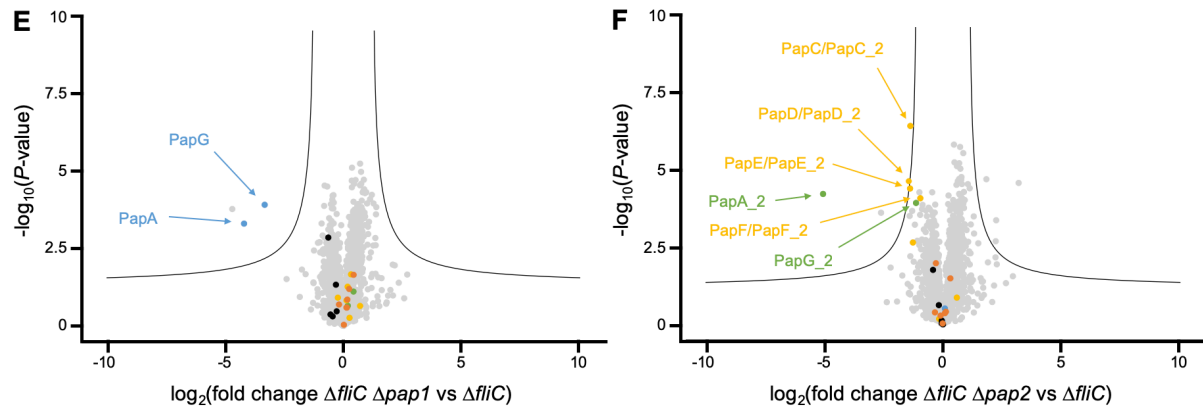


**Figure 3.14: P pili expression is upregulated in F1C pili-deficient high-adhesion UPEC mutants.** (A) Expression levels of genes encoding the major pilin subunits of type 1 pili (*fimA*, black), P1 pili (*papA*, blue), and P2 pili (*papA\_2*, green) measured by qRT-PCR for the indicated mutant strains. Relative expression (fold change) was calculated by normalizing to the  $\Delta fliC$  parental strain. *P*-values were calculated using Student's t-test comparing mutant strains to  $\Delta fliC$ ; *P*-values > 0.05 are not shown; n.d. not detected. (B) Expression levels of the selected type 1 and P pili genes in the  $\Delta fliC$  parental strain. Relative expression was calculated by normalizing to the expression level of *gapA*. For panels (A,B), *n* = 3 independent experiments; bars indicate mean; error bars indicate standard deviation. (C) Efficiency of the surface biotinylation and protein affinity-purification steps. For each protein quantified by mass spectrometry, the Z-score in the surfaceome (corresponding to the fraction of proteins enriched by affinity-purification) is plotted against the Z-score in the total cell extract. Orange: proteins that localize to the outer membrane according to their gene ontology (GO) annotation; blue: other proteins. (D-F) Volcano plots showing changes in surface protein abundances between  $\Delta fliC \Delta foc$  and  $\Delta fliC$  (D),  $\Delta fliC \Delta pap1$  and  $\Delta fliC$  (E), or  $\Delta fliC \Delta pap2$  and  $\Delta fliC$  (F). Proteins that are part of the following pili operons are colored: type 1 pili (black), P1 pili (blue), P2 pili (green), proteins common to P1 and P2 pili (yellow), F1C pili (orange). The name of the pili proteins showing a significant change is indicated. *n* = 4 independent experiments; the grey line corresponds to a false discovery rate of 0.01.

To further assess whether the upregulation of *papA* and *papA\_2* expression in the  $\Delta fliC \Delta foc$  mutant translates into increased P pili synthesis, we performed quantitative mass spectrometry analysis of the bacterial surface proteome. The fraction of surface-exposed proteins was isolated through surface biotinylation and affinity-purification

([Monteiro et al., 2018](#)). We confirmed that this procedure led to significant enrichment of proteins localised at the outer membrane based on gene ontology (GO) annotation of the CFT073 genome (**Figure 3.14C**). In agreement with results of mRNA analysis (**Figure 3.14A**), we observed a higher abundance of P1 and P2 proteins in the  $\Delta fliC$   $\Delta foc$  mutant compared to the  $\Delta fliC$  parental strain, while proteins corresponding to type 1 pili did not show any differential abundance between the two strains (**Figure 3.14D**). Despite the similarity between P1 and P2 proteins (**Figure 3.8A**), we verified that the  $\Delta pap1$  and  $\Delta pap2$  mutants could be distinguished at the protein level: as expected, PapA and PapG were decreased specifically in the  $\Delta fliC$   $\Delta pap1$  strain, while PapA\_2 and PapG\_2 were decreased specifically in the  $\Delta fliC$   $\Delta pap2$  strain (**Figure 3.14E,F**). Overall, these results demonstrate increased synthesis of P1 and P2 pili in the  $\Delta fliC$   $\Delta foc$  mutant compared to the  $\Delta fliC$  parental strain, consistent with evidence of cross-regulation between different pili operons in UPEC ([Holden and Gally, 2004](#)).

### 3.1.7. Quantification of single-cell piliation of pili-deficient UPEC mutants

We next asked how deletion of whole pili operons would affect UPEC piliation at the single-cell level. We therefore developed an Ilastik-based automated image analysis pipeline to count the number of pili per bacterium on SEM images of single bacteria (see **3.3.Materials and methods** and **Figure 3.16**). Despite some variability, most bacteria in the  $\Delta fliC$  parental strain were heavily piliated (**Figure 3.15A,B**), confirming the observations of **Figure 3.1C**. In sharp contrast, bacteria in the  $\Delta fliC$  *dsbA*-Tn mutant were almost completely devoid from pili (**Figure 3.15A,C**), as expected from the severe adhesion defect of this mutant (**Figure 3.5B**). Surprisingly, we did not observe increased single-cell piliation in the  $\Delta fliC$   $\Delta foc$  mutant compared to the  $\Delta fliC$

parental strain (**Figure 3.15A**), presumably because the increased synthesis of P1 and P2 pili is offset by the absence of F1C pili (**Figure 3.14D**). We however observed decreased piliation when deleting the entire *fim* operon but not when deleting only the *fimH* gene encoding the type 1 pili adhesin. Likewise, piliation was decreased in the  $\Delta fliC$  *papC*-Tn mutant but unchanged in the  $\Delta fliC$  *papG*-Tn mutant, in accordance with the disparate roles of PapC as the usher component of the P1 pili assembly machinery and of PapG as the P1 pili adhesin. Consistent with this interpretation, we found that deletion of the entire *pap1* operon, *pap2* operon, or both operons resulted in decreased piliation compared to the  $\Delta fliC$  parental strain (**Figure 3.15A**). Taken together, these results show that deletion of type 1 pili, P1 pili and P2 pili operons in the  $\Delta fliC$  background all lead to a clear decrease in bacterial piliation, even though the former does not have any impact on early adhesion to bladder cells (**Figure 3.11A**).

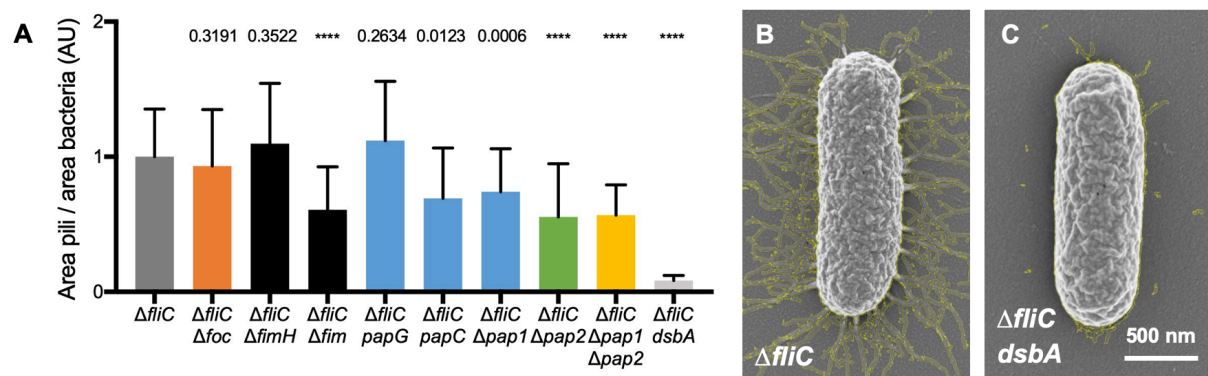


**Figure 3.15: Quantification of single-cell piliation of pili-deficient UPEC mutants.** (A) Quantification of the number of pili per bacterium for the indicated UPEC strains. Data were normalized to the  $\Delta fliC$  parental strain (dark grey). Mutants were colored according to the pili disrupted: F1C pili (orange), type 1 pili (black), P1 pili (blue), P2 pili (green), P1 and P2 pili (yellow).  $n \geq 30$  bacteria from 2 biological replicates for the  $\Delta fliC$  parental strain and unmarked deletion mutants;  $n \geq 15$  bacteria from 1 biological replicate for transposon mutants;  $P$ -values were calculated using Mann-Whitney's test comparing mutant strains to  $\Delta fliC$ ; \*\*\*\*  $P < 0.0001$ . (B,C) Corresponding SEM images for  $\Delta fliC$  (B) and  $\Delta fliC$  *dsbA*-Tn (C), showing the pili highlighted in yellow. Scale bar: 500 nm for both images.



### 3.2. Discussion and outlook

Adhesion and invasion into superficial bladder umbrella cells allow UPEC to form intracellular biofilm-like communities (IBCs) and quiescent intracellular reservoirs (QIRs), which are suspected to be a major cause of bacterial persistence within the bladder. There is a growing interest in developing anti-adhesion therapies for UTIs as an alternative to conventional antibiotics, which requires a more complete understanding of the molecular mechanisms that promote bacterial adhesion and invasion into the bladder epithelium. Here, we carry out a high-content screen to identify genes that are important for early adhesion of a clinical UPEC isolate to human bladder epithelial cells. Unexpectedly, neither the results of our screen nor targeted analysis of unmarked deletion mutants support a role for type 1 pili in early adhesion of UPEC to bladder cells. Instead, our results show that, under the conditions of our assay, early adhesion is mediated by P pili: deletion of genes encoding P pili leads to decreased adhesion to bladder cells, while deletion of genes encoding F1C pili leads to increased P pili synthesis and increased adhesion to bladder cells.

Our results do not rule out the involvement of type 1 pili in the overall UPEC infection cycle within the bladder. Binding of type 1 pili to uroplakins expressed on the surface of bladder epithelial cells has been characterized in depth ([Wu et al., 1996](#); [Zhou et al., 2001](#); [Thumbikat et al., 2009](#)), and the contribution of type 1 pili to invasion of bladder epithelial cells has been documented in several studies, using both *in vivo* mouse infection models and *in vitro* human cell culture-based systems ([Mulvey et al., 1998](#); [Martinez et al., 2000](#); [Hung et al., 2002](#); [Wright et al., 2007](#)). In most studies though, prolonged contact between UPEC and bladder cells (several hours) did not

permit the distinction between bacterial adhesion and internalization. It is also possible that different mechanisms might mediate early and late adhesion, as shown for example for enteropathogenic *E. coli* (Cleary et al., 2004). Our results suggest that early adhesion of UPEC to bladder epithelial cells is mediated by P pili, whereas type 1 pili likely play a role in internalization and IBC formation, as described previously (Anderson et al., 2003; Duraiswamy et al., 2018). This interpretation is consistent with an earlier study in which recombinant expression of either type 1 pili or P pili in a lab-adapted K12 strain of *E. coli* both conferred the ability to adhere to 5637 human bladder epithelial cells after two hours of co-incubation (Martinez et al., 2000). However, only bacteria expressing type 1 pili were recovered after treatment of the infected cells with gentamicin, an antibiotic that cannot penetrate the host-cell membrane, indicating that, under these conditions, expression of P pili alone was sufficient to mediate adhesion but not invasion. Another strategy was used by Virkola et al., 1988 where recombinant K12 strains expressing cloned type 1 or P pili were tested for their ability to adhere to fixed tissue sections coming from human bladder biopsies. After a short incubation time, bacterial adhesion to the epithelial layer of the bladder was found to be non-existent for type 1-piliated bacteria and weak for P-piliated bacteria, although fixed tissue samples are unlikely to entirely reproduce the natural physiology of bladder epithelial cells. Still, it is worth noting that this setup prevents any form of bacterial invasion of host cells, and as such, provides an interesting method to look at UPEC adhesion in the absence of internalization. In this case, type 1 pili do not seem to play any role in adhesion to the bladder epithelium.

Importantly, the work presented here was conducted with a clinical isolate of UPEC, which simultaneously expresses a variety of pili types at the population level, including

but not limited to type 1 and P pili, as assessed by qRT-PCR and mass spectrometry. Under these conditions, type 1 pili appear to be dispensable for UPEC adhesion to human bladder cells. Functional redundancy between different pili operons could provide one possible explanation for this unexpected result. The CFT073 strain encodes 10 CUP operons in total, some of which share a high degree of sequence identity with the operon encoding type 1 pili. For example, the F9 pili adhesin YdeQ (encoded by *c1931* in CFT073) shares 48% amino acid sequence identity with the type 1 pili adhesin FimH (**Table 1.1**). YdeQ was previously shown to be important for sustained colonization of the inflamed bladder in UPEC-infected mice ([Conover et al., 2016](#)). Peptide sequences corresponding to YdeQ were identified in our mass spectrometry analysis of the CFT073 surface proteome, confirming that F9 pili are expressed and exposed on the surface of the bacteria under the conditions of our assay. Thus, the apparent lack of an essential role for type 1 pili might be explained by functional redundancy between type 1 pili and F9 pili or other pili expressed by CFT073. This could also explain the residual adhesion that we observe for the *pap1 pap2* double deletion mutant.

The absence of fluidic flow in our model system might also explain the apparent lack of an essential role for type 1 pili in our adhesion assay. Shear stress has been shown to increase the affinity of FimH binding to mannosylated surfaces via a ‘catch-bond’ mechanism ([Thomas et al., 2002](#); [Yakovenko et al., 2008](#)). Conversely, the affinity of FimH for mannosylated residues is reduced in the absence of tensile stress ([Sauer et al., 2016](#)). The impact of flow on the relative contribution of different pili types to adhesion could be studied in greater depth using a model of the human bladder that reproduces flow and shear stress, such as the recently developed bladder-chip device

([Sharma et al., 2021b](#)). Still, it is worth noting that the impact of flow on bacteria in the bladder is cyclical, with short periods of high-velocity flow during micturition events interspersed with long periods of little or no flow. Thus, the absence of flow in our model system arguably represents the flow conditions within the urinary bladder during most of the micturition cycle.

Although an essential role for type 1 pili in colonization of the bladder has been clearly demonstrated in mouse models of infection ([Kalas et al., 2017](#)), the evidence implicating type 1 pili in bladder colonization in humans is somewhat mixed ([Hannan et al., 2012](#)). Possible explanations for this apparent discrepancy include the fact that type 1 pili genes are variably expressed in human UTIs and weakly expressed in human urine *in vitro* ([Hagan et al., 2010](#); [Subashchandrabose et al., 2014](#); [Greene et al., 2015](#)). Even when expressed *in vivo*, type 1 pili may be bound by the Tamm-Horsfall protein, which has been shown to inhibit adhesion of type 1-piliated *E. coli* to uroplakins ([Pak et al., 2001](#); [Bates et al., 2004](#)), or by uromodulin, which was recently shown to aggregate type 1-piliated bacteria, possibly facilitating their clearance from the urinary tract ([Weiss et al., 2020](#)). These observations suggest that type 1 pili might not be the only mediators of UPEC adhesion in the human bladder. Although it is generally thought that P pili are important for UPEC infection in the kidney rather than the bladder, our demonstration of an essential role for P pili in early adhesion of CFT073 to bladder epithelial cells *in vitro* is consistent with evidence that P pili are expressed by UPEC in the human bladder ([de Ree et al., 1987](#); [Agata et al., 1989](#)).

Finally, the work presented here identifies potential targets for the development of new anti-adhesion therapies. For example, the periplasmic chaperone DsbA, identified by

several low-adhesion hits in our screen, was the target of a recent study aimed at evaluating small-molecule inhibitors as candidates for anti-virulence therapeutics (Verderosa et al., 2021). DsbA is responsible for disulfide bond formation in pili subunits within the bacterial periplasm, and deletion of *dsbA* was previously shown to abolish P pili biogenesis in a lab strain of *E. coli* engineered to express P pili (Jacob-Dubuisson et al., 1994). Another example is the Dam DNA adenine methylase, also identified by low-adhesion hits in our screen. Dam regulates several virulence factors and has been shown to be essential for epigenetic regulation of *fim*, *pap*, and *foc* transcription along with leucine-responsive regulatory protein Lrp and cAMP receptor protein Crp (van der Woude and Bäumlér, 2004; Totsika et al., 2008), both of which were identified as low-adhesion hits in our screen too. With some modifications, our screening method could also be used for other applications, for example, screening of mutant libraries to identify genes important for invasion of bladder cells and formation of IBCs, or high-throughput analysis of collections of clinical isolates to compare quantifiable phenotypes such as their adhesion to bladder cells. These studies would not only advance our understanding of key mechanisms of UPEC pathogenesis in the bladder, they might also inform new strategies for the development of small molecules targeting virulence factors as an alternative to conventional antibiotics.

### **3.3. Materials and methods**

#### **3.3.1. Plasmids and primers**

Plasmids, primers and qRT-PCR primers used in this chapter are listed in **Tables 5.2, 5.3 and 5.5** respectively.

### **3.3.2. Bacterial culture conditions**

CFT073 wild-type and mutant strains were inoculated from frozen glycerol stocks and cultured in LB Miller medium (Difco) overnight for 16 h ( $\pm$  1 h) at 37°C without shaking to induce type 1 pili expression for adhesion experiments, or with shaking at 170 rpm for molecular cloning experiments. When required, LB was supplemented with 100 µg/mL ampicillin (Sigma) or 50 µg/mL kanamycin (Sigma).

### **3.3.3. Human bladder epithelial cell culture**

Human 5637 bladder epithelial cells (HTB-9™, procured from ATCC) were cultured in RPMI 1640 medium (ATCC) supplemented with 10% Fetal Bovine Serum (FBS, Gibco) at 37°C, 5% CO<sub>2</sub>. Cells were split every other day by detachment with trypsin-EDTA 0.05% (Gibco) for 5 minutes at 37°C. Cells were then either passaged at a 1:3 ratio in fresh RPMI 10% FBS for cell line maintenance, or diluted in phenol-red-free RPMI medium (Gibco) 5% FBS for microscopy experiments.

### **3.3.4. Spinfection of bladder epithelial cells with UPEC**

CellCarrier™-96 Ultra microplates (Perkin-Elmer) were plasma-activated with a Zepto plasma cleaner (Diener Electronic) at 30 W for 1 min, coated with an ice-cold solution of 50 µg/mL bovine dermis native collagen (AteloCell) in PBS (Gibco), and incubated for 3 h at 37°C for the collagen to polymerize. Wells were washed twice with PBS to remove unbound collagen, seeded with 5637 epithelial cells in phenol-red-free RPMI 5% FBS at a density of 50,000 cells per well, and incubated overnight at 37°C, 5%

CO<sub>2</sub> to reach confluency. On the day of the experiment, RPMI was removed from the plates and wells were rinsed once with PBS. Overnight UPEC cultures in 96-well plates were diluted 1:10 in phenol-red-free RPMI 5% FBS and added to the epithelial cells at a multiplicity-of-infection (MOI) of 200:1 using a Liquidator 96 (Mettler-Toledo). Plates were spun down at 600g for 5 minutes and incubated for 20 minutes at 37°C, 5% CO<sub>2</sub>. Wells were washed twice with PBS to remove non-adherent bacteria and phenol-red free RPMI 5% FBS was added back.

### **3.3.5. Immunostaining of bladder epithelial cells**

Confluent 5637 bladder epithelial cells in 96-well plates were fixed with 4% paraformaldehyde (PFA) for 30 minutes. Fixed cells were washed three times with PBS, permeabilized with 0.15 % Triton X-100 for 15 minutes, washed three times with PBS, and blocked with antibody incubation buffer (PBS supplemented with 1% BSA and 0.01% Triton X-100) for 1 hour. Cells were then incubated with primary antibodies (rabbit monoclonal Alexa Fluor® 647 anti-cytokeratin 8 antibody from abcam, or mouse monoclonal anti-uropodkin IIIa antibody from Santa Cruz) at a 1:100 dilution in antibody incubation buffer overnight at 4°C, and washed three times with PBS. For uropodkin staining, cells were subsequently incubated with secondary antibodies (donkey anti-mouse Alexa Fluor® 647 highly cross-adsorbed IgG from Invitrogen) at a concentration of 2 µg/mL in antibody incubation buffer for 1 hour at room temperature, and washed three times with PBS. Cell nuclei were stained with a 5 µg/mL DAPI (Invitrogen) solution in PBS for 30 minutes, followed by three additional washes with PBS. Cells were imaged with a 63X oil objective on a SP8 confocal microscope (Leica), and images were deconvolved using SVI Huygens (Quality, 0.05; Iterations, 40).

### **3.3.6. High-content imaging of bladder epithelial cells infected with UPEC**

Wells containing infected 5637 bladder cells were imaged in 9 fields of view using a high-throughput Operetta CLS microscope (Perkin-Elmer) on the phase-contrast and green fluorescence channels (Excitation BP 435-460 BP 460-490; Dichroic LP 495; Emission HC 500-550) with a 20X air objective (NA = 0.40). The microplate was maintained at 37°C, 5% CO<sub>2</sub> during imaging. Image analysis was performed using the integrated Harmony® high-content analysis software (Perkin-Elmer). Briefly, the mean GFP fluorescence was displayed for each field of view and the average and standard deviation for the 9 fields of view were calculated for each well. For wells where the coefficient of variation (CV) exceeded 10%, images were manually inspected and fields of view with fluorescence artefacts removed from the analysis.

### **3.3.7. Screening for UPEC mutants with altered adhesion: 1<sup>st</sup> step**

In the first screening step, 96-well plates were arranged with 93 transposon insertion mutants, the *ΔfliC* parental strain, the *ΔfliC dksA*-Tn low-adhesion strain, and one blank well containing LB medium only. After overnight culture, they were used to infect 5637 bladder epithelial cells following the aforementioned procedure. OD<sub>600</sub> was also recorded for each well and mutants that did not grow were removed from the analysis. After spinfection and imaging, the average and standard deviation of GFP fluorescence on a particular plate were calculated based on the individual fluorescence values for each well, and mutants with values more than 1.5 standard deviations from the average were selected for retesting. We always made sure that the value for the *ΔfliC* parental strain was less than 1.5 standard deviations from the



average, and that the value for the  $\Delta fliC$  *dksA*-Tn low-adhesion strain was more than 2 standard deviations from the average, otherwise the experiment was repeated for that plate. We also visually controlled the integrity of the epithelial cell layer in each well by phase-contrast microscopy.

### **3.3.8. Screening for UPEC mutants with altered adhesion: 2<sup>nd</sup> step**

In the second screening step, 96-well plates were arranged with 3 wells of each candidate mutant, 30 wells containing the  $\Delta fliC$  parental strain, 3 wells containing the  $\Delta fliC$  *dksA*-Tn low-adhesion strain, and 3 blank wells containing LB medium only. After overnight culture, they were used to infect 5637 bladder epithelial cells following the aforementioned procedure. After spinfection and imaging, the average and standard deviation of GFP fluorescence were calculated for the 30 replicates of the reference strain, and mutants with values more than 2 standard deviations from the average were selected for retesting.

### **3.3.9. Screening for UPEC mutants with altered adhesion: 3<sup>rd</sup> step**

In the third screening step, candidate mutants were cultured overnight in individual flasks along with the  $\Delta fliC$  parental strain and the  $\Delta fliC$  *dksA*-Tn low-adhesion strain. All cultures were adjusted to the same final OD<sub>600</sub> value in pre-warmed phenol-red-free RPMI 5% FBS, so that this would correspond to a 1:10 dilution for the mutant with the lowest overnight OD<sub>600</sub>. 96-well plates were arranged with 6 wells of each mutant, 6 wells containing the  $\Delta fliC$  parental strain, 6 wells containing the  $\Delta fliC$  *dksA*-Tn low-adhesion strain, and 6 blank wells containing phenol-red-free RPMI 5% FBS. The rest

of the procedure was conducted as described above. For each mutant, the distribution of GFP fluorescence values after spinfection was compared to the distribution for the  $\Delta fliC$  parental strain using Welch's t-test and strains with  $P < 0.05$  were selected for further analysis.

### **3.3.10. Identification of transposon insertion sites by RATE (rapid amplification of transposon ends)**

Tn5 insertion sites were identified using a single-primer PCR protocol adapted from [Ducey et al., 2002](#). Briefly, confirmed mutants were streaked on LB agar supplemented with 50 µg/mL kanamycin. A single colony was boiled for 10 minutes in 50 µL water and 1 µL was used as template in a standard 50-µL PCR reaction with primer R6K\_inv1 using a double amount of Platinum® Taq High Fidelity DNA Polymerase (Invitrogen). The first 30 cycles of the PCR reaction were done at 55°C with a 60-sec extension time; the next 30 cycles were done at 30°C with a similar extension time; and the last 30 cycles were performed at 55°C with a 2-minute extension time. PCR amplicons were then sent for sequencing using the nested R6K\_RP1 primer (Microsynth), and the sequence was aligned to the chromosome of CFT073 using Snapgene.

### **3.3.11. Assignment of P pili transposon insertions to the *pap1* or *pap2* operons**

To determine whether a transposon insertion occurred within the *pap1* or *pap2* operon, we performed a dual set of standard 25-µL Q5® PCR reactions (New England Biolabs) using a first primer specific to the transposon sequence, and a second primer specific

to the DNA sequence flanking either of the two operons. Primer pairs were chosen based on the position and orientation of each transposon insertion, as indicated in **Table 5.4**. PCR amplicons were analysed on 1% agarose gels stained with SYBR® Safe DNA Gel Stain (Invitrogen), and identification of the gene disrupted was based on the brightest amplicon band (**Figure 3.8B-D**).

### 3.3.12. Construction of unmarked UPEC deletion strains

The *fimH* locus (between nucleotides 5,143,529 and 5,144,440), *fim* operon (between nucleotides 5,135,689 and 5,144,440), *foc* operon (between nucleotides 1,188,213 and 1,194,827) and *pap* operons (*pap1* operon between nucleotides 3,429,593 and 3,437,564; *pap2* operon between nucleotides 4,940,831 and 4,948,799) were deleted from CFT073 sfGFP and CFT073  $\Delta fliC$  sfGFP using the  $\lambda$  Red recombineering system as described earlier. The *kan<sup>R</sup>* resistance cassette was amplified from plasmid pKD4 using primer pairs *fimH\_KO\_F* + *fimH\_KO\_R*, *fimB\_KO\_F* + *fimH\_KO\_R*, *focA\_KO\_F* + *focH\_KO\_R*, and *papA\_KO\_F* + *papG\_KO\_R* respectively. For deletion of the *pap* operons, we used the same primer pair for integration of the *kan<sup>R</sup>* resistance cassette in place of either operon and then identified the disrupted operon using specific primer pairs. Successful chromosomal recombination was confirmed by PCR using primer pairs *fimH\_F* + *fimH\_R* for  $\Delta fimH$ , *fimB\_F* + *fimH\_R* for  $\Delta fim$ , *focA\_F* + *focH\_R* for  $\Delta foc$ , *papI\_F* + *papG\_R* for  $\Delta pap1$ , and *papI2\_F* + *papG2\_R* for  $\Delta pap2$ . The double *pap* deletion mutants were obtained by successively deleting the *pap1* and *pap2* operons from CFT073 sfGFP and CFT073  $\Delta fliC$  sfGFP. Adhesion phenotypes of all mutants were assessed using the same method as in the third step of the screen. To be able to pool data coming from different experiments, results were normalized to

either CFT073 sfGFP or CFT073  $\Delta fliC$  sfGFP depending on the strain used for deletion construction.

### **3.3.13. Quantitative real-time PCR (qRT-PCR)**

CFT073 mutant strains cultured overnight in static conditions were pelleted and RNA was extracted using the High Pure RNA Isolation kit (Roche) according to the manufacturer's instructions. RNA samples were DNase-treated using the TURBO DNA-free™ kit (Invitrogen), and cDNA was obtained using the SuperScript™ IV reverse transcriptase with random hexamers (Invitrogen). qRT-PCR reactions were set up using the SYBR® Green PCR Master Mix (Applied Biosystems) with 2.5  $\mu$ M primers and 2  $\mu$ L cDNA. Reactions were run on an ABI PRISM7900HT Sequence Detection System (Applied Biosystems). For each gene and each experiment, relative expression levels were calculated by normalizing to the expression level of the housekeeping gene *gapA* and to the expression level in the  $\Delta fliC$  parental strain.

### **3.3.14. Biotinylation of surface-exposed proteins and protein affinity purification**

The bacterial surface proteome was isolated as described by [Monteiro et al., 2018](#). Briefly, CFT073 mutant strains cultured overnight in static conditions were pelleted, washed twice with PBS, and incubated for 30 minutes in PBS supplemented with 1% (m/m) sulfo-NHS-SS-biotin (Thermo Scientific Pierce™) under gentle agitation at room temperature. Excess of the biotinylation reagent was quenched by three washes with a 500 mM glycine (AppliChem) solution in PBS, and bacteria were resuspended in PBS supplemented with 1% (v/v) Triton X-100 and Protease Inhibitor Cocktail

(Roche). Cell lysis was performed using FastPrep (MP Biomedicals) with two steps of 20 sec at 6 m/s, and cell debris were pelleted by centrifugation at 20,000g for 30 minutes. Biotinylated proteins in the supernatant were affinity-purified using High Capacity NeutrAvidin™ Agarose (Thermo Scientific Pierce™) according to the manufacturer's instructions. Briefly, agarose slurry was packed into 2 mL Centrifuge Columns (Thermo Scientific Pierce™), washed with 3 column volumes of PBS, and incubated with protein samples for 60 minutes at 4°C under gentle rotation. Unlabelled proteins were washed away with 5 column volumes of PBS, and biotinylated proteins were eluted with DTT-modified Laemmli buffer (2% SDS, 20% glycerol, 62.5 mM Tris-HCl, 50 mM DTT, 5% β-mercaptoethanol). The protein concentration in eluted samples was assessed using the Pierce™ 660nm Protein Assay (Thermo Scientific Pierce™) according to the manufacturer's recommendations for samples eluted in Laemmli buffer. To assess the efficiency of the surface biotinylation and affinity-purification steps (**Figure 3.14C**), CFT073  $\Delta fliC$  sfGFP protein samples were prepared as described above, except that lysis was performed with 2% SDS (Sigma). Samples before affinity-purification (total cell extracts) were then directly analysed by mass spectrometry along with affinity-purified samples (surfaceomes).

### 3.3.15. Protein sample preparation

Mass spectrometry-based proteomics-related experiments were performed by the Proteomics Core Facility (PCF) at EPFL. Protein samples (10 µg per dataset) were loaded on an SDS-PAGE gel and allowed for a short migration. The gel pieces containing the concentrated proteins were excised, washed twice with 50% ethanol in 50 mM ammonium bicarbonate (AB, Sigma) for 20 minutes, and dried by vacuum

centrifugation. Proteins were reduced with 10 mM dithioerythritol (Merck-Millipore) for 1 hour at 56°C followed by washing/drying. Reduced proteins were alkylated with 55 mM iodoacetamide (Sigma) for 45 minutes at 37°C in the dark followed by washing/drying. Alkylated proteins were digested overnight at 37°C using mass spectrometry grade Trypsin Gold (Promega) at a concentration of 12.5 ng/μL in 50 mM AB supplemented with 10 mM CaCl<sub>2</sub>. Resulting peptides were extracted in 70% ethanol, 5% formic acid (FA, Merck-Millipore) twice for 20 minutes, dried by vacuum centrifugation and stored at -20 °C until further analysis.

### **3.3.16. Mass spectrometry analysis**

Peptides were desalted on C<sub>18</sub> StageTips ([Rappsilber et al., 2007](#)) and dried by vacuum centrifugation prior to LC-MS/MS injections. Samples were resuspended in 2% acetonitrile (Biosolve), 0.1% FA and nano-flow separations were performed on a Dionex UltiMate™ 3000 RSLCnano UPLC system (Thermo Scientific™) on-line connected with an Orbitrap Exploris™ 480 mass spectrometer (Thermo Scientific™). A capillary precolumn (Acclaim™ PepMap™ C<sub>18</sub>, 3 μm-100Å, 2 cm x 75 μm i.d.) was used for sample trapping and cleaning. A 50cm long capillary column (75 μm i.d., in-house packed using ReproSil-Pur C<sub>18</sub>-AQ 1.9 μm silica beads, Dr. Maisch) was then used for analytical separations at 250 nL/min over 150-minute biphasic gradients. Acquisitions were performed through Top Speed Data-Dependent acquisition mode using a cycle time of 2 seconds. First MS scans were acquired with a resolution of 60'000 (at 200 m/z) and the most intense parent ions were selected and fragmented by High energy Collision Dissociation (HCD) with a Normalized Collision Energy (NCE) of 30% using an isolation window of 2 m/z. Fragmented ions were acquired with a

resolution of 15'000 (at 200 m/z) and selected ions were then excluded for the following 20 seconds.

### 3.3.17. Bioinformatic analysis

Raw data were processed using MaxQuant 1.6.10.43 (Cox and Mann, 2008) against the *Escherichia coli* CFT073 Uniprot database (5336 entries, last modification 210307). Carbamidomethylation was set as fixed modification, whereas oxidation (M), phosphorylation (S, T, Y), acetylation (Protein N-term), CAMthiopropionyl (K and Protein N-term) and glutamine to pyroglutamate were considered as variable modifications. A maximum of two missed cleavages were allowed and “Match between runs” option was enabled. A minimum of two peptides was required for protein identification and the false discovery rate (FDR) cutoff was set to 0.01 for both peptides and proteins. Label-free quantification and normalisation was performed by MaxQuant using the MaxLFQ algorithm, with the standard settings (Cox et al., 2014).

The statistical analysis was performed using Perseus 1.6.12.0 (Tyanova et al., 2016) from the MaxQuant tool suite. Reverse proteins, potential contaminants and proteins only identified by sites were filtered out. Protein groups containing at least three valid values in at least one group were conserved for further analysis. Empty values were imputed with random numbers from a normal distribution (width: 0.3, down shift: 1.8 sd). A two-sample t-test with permutation-based FDR statistics (250 permutations, FDR = 0.01, S0 = 0.5) was performed to determine significant differentially abundant candidates. Further graphical displays were performed using homemade programs written in R (<https://www.R-project.org/>).

### 3.3.18. Scanning electron microscopy (SEM) sample preparation

5637 bladder epithelial cells spininfected with UPEC in  $\mu$ -dishes (Ibidi) or CFT073 mutant strains left to adhere for 20 minutes on poly-L-lysine-coated coverslips were fixed for 30 minutes with 1.25% glutaraldehyde in PBS 0.1M pH 7.4. Sample preparation was then performed by the Biological Electron Microscopy Facility (BioEM) at EPFL. Samples were post-fixed for 30 minutes with 1% osmium tetroxide in 0.1 M cacodylate buffer followed by washing with distilled water. Next, samples were dehydrated in graded ethanol series and dried in an automated critical point dryer (Leica Microsystems). Finally, samples were attached to an adhesive conductive surface followed by coating with 3-4 nm of gold/palladium (Quorum Technologies). Images of the samples were acquired using a field emission scanning electron microscope (Zeiss NTS).

### 3.3.19. Automated quantification of single-cell piliation using Ilastik

The Ilastik-based image analysis pipeline was developed and optimized by Anaëlle Dubois from the BioEM Facility. The Ilastik software was trained by manually annotating background, pili and bacterial body on four SEM images of the  $\Delta fliC$  parental strain. After applying the trained software on a new SEM image, the channel corresponding to the bacterial body was processed using Fiji and subtracted from the channel corresponding to the pili (see **Figure 3.16**). In order to take into account the varying sizes of bacterial cells, single-cell piliation was then inferred by dividing the area corresponding to the pili by the area corresponding to the bacterial body.



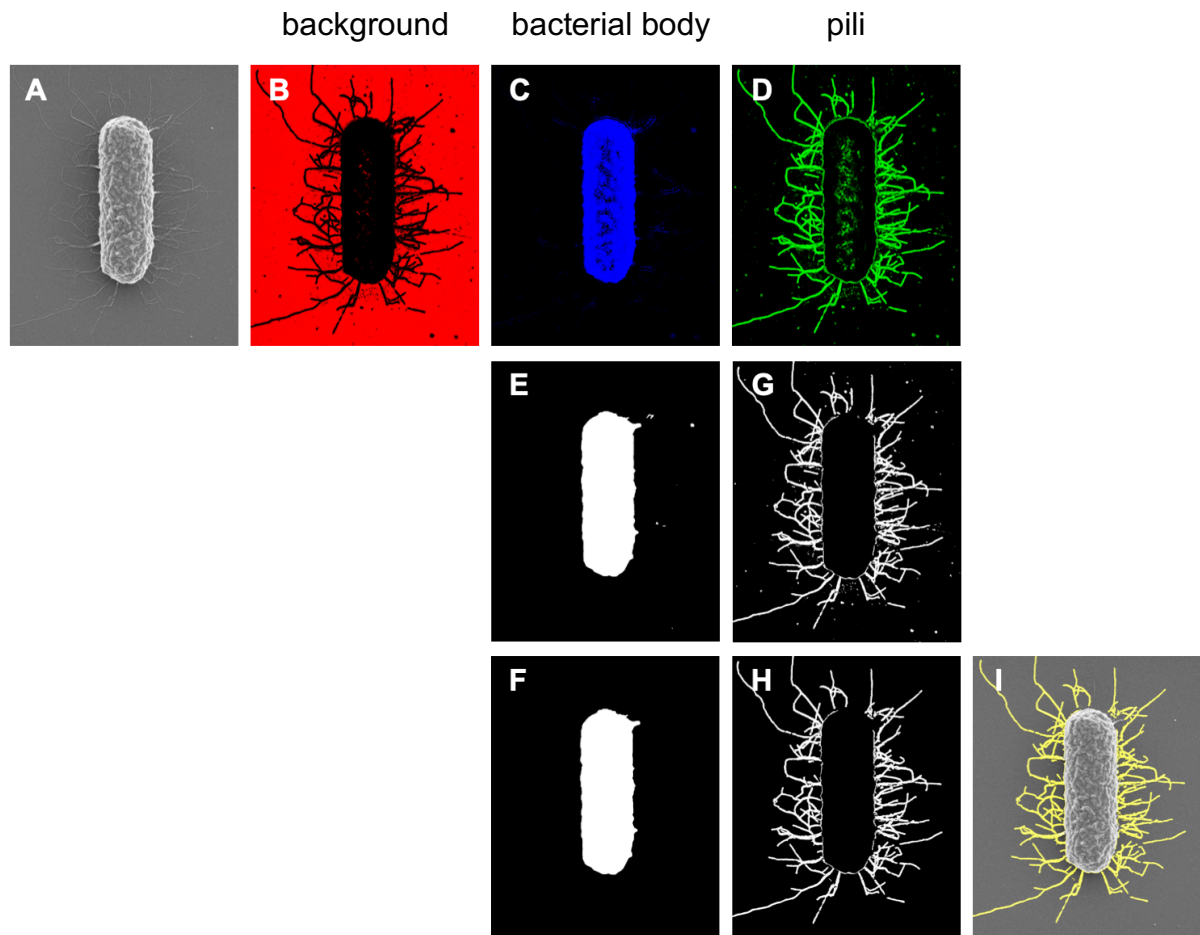


**Figure 3.16: Automated quantification of UPEC single-cell piliation on SEM images using Ilastik.** (B-D) Channels obtained when applying the trained Ilastik software on the original SEM image shown in (A). (B) Channel 1: background. (C) Channel 2: bacterial body. (D) Channel 3: pili. The image corresponding to the bacterial body (C) is further processed using Fiji to fill holes (E) and keep only circular particles with an area above 250,000 pixels (F). The image corresponding to the pili (D) is then subtracted with the processed bacterial body channel (G) and further processed to keep only non-circular particles with an area above 100 pixels (H). The cleaned pili channel can eventually be merged with the original SEM image, resulting in the overlay shown in (I).

## **4. High-content microfluidic screening identifies UPEC mutants with decreased persistence to fosfomycin in synthetic human urine**

In this chapter, we combined microfluidics and time-lapse microscopy together with the transposon insertion library previously constructed to screen for UPEC mutants with defects in persistence to fosfomycin in a synthetic surrogate for human urine.

Keywords: uropathogenic *Escherichia coli* (UPEC); high-content screening (HCS); microfluidics; time-lapse microscopy; antibiotic persistence; fosfomycin (FOS); synthetic human urine (SHU); cell-wall-deficient forms; peptidoglycan synthesis; outer membrane synthesis

### **4.1. Results**

#### **4.1.1. Design of the microfluidic screening platform**

The microfluidic platform that we used for high-content UPEC imaging is derived from a series of previously published designs aimed at screening yeast ([Dénervaud et al., 2013](#)) and mycobacteria ([Verpoorte, 2017](#)) libraries with the following capabilities:

- single-cell-resolution time-lapse imaging of yeast / bacteria
- precise control over the growth environment
- automatized imaging of hundreds of mutants in parallel

This makes it perfectly suited to screen for UPEC mutants with altered antibiotic persistence, which is a phenotype displayed by a small fraction of bacteria, and which requires switching between media with and without antibiotic over time.

The microfluidic device consists of an array of 1,152 microchambers, where bacteria can be grown and imaged (**Figure 4.1A**). These microchambers are connected to flow channels, which provide continuous perfusion with culture medium (**Figure 4.1B**). Channels and chambers form the so-called flow layer of the device, which is in direct contact with a microscope coverslip (**Figure 4.1C**). Channels are 12  $\mu\text{m}$  high whereas chambers are only 1.4  $\mu\text{m}$  high, so as to constrain bacterial growth to the horizontal plane and improve single-cell imaging quality. The flow layer is topped by a second layer called the control layer, which consists of 12  $\mu\text{m}$ -high control channels arranged perpendicularly to the flow channels (**Figure 4.1A,C**). Both layers are made of polydimethylsiloxane (PDMS), which is a soft elastomeric material (**Figure 4.1D**). Control channels thus function as micromechanical valves: when their inner pressure is increased, the underlying flow channel collapses and medium supply is interrupted (**Figure 4.1C**). The whole process is reversible and highly responsive, so that flow channels can be opened and closed within milliseconds ([Unger et al., 2000](#)). This allows fast and precise switching between different media sources, which can advantageously be used for transient antibiotic treatment of bacteria in the device.

The design presented in **Figure 4.1A** directly stems from the one described by [Verpoorte, 2017](#) with two major modifications. First, the microchamber size was decreased in order to be able to capture the whole chamber in a single camera field-of-view during time-lapse imaging, and therefore ensure that all UPEC regrowth events within a microchamber were properly recorded. Second, the number of control valves was reduced to the strict minimum, so as to facilitate the setup of the device and limit the time before UPEC can be provided with culture medium (see below). Photomasks and silicon wafers used to fabricate this modified PDMS device were prepared as described in **4.3. Materials and methods**.

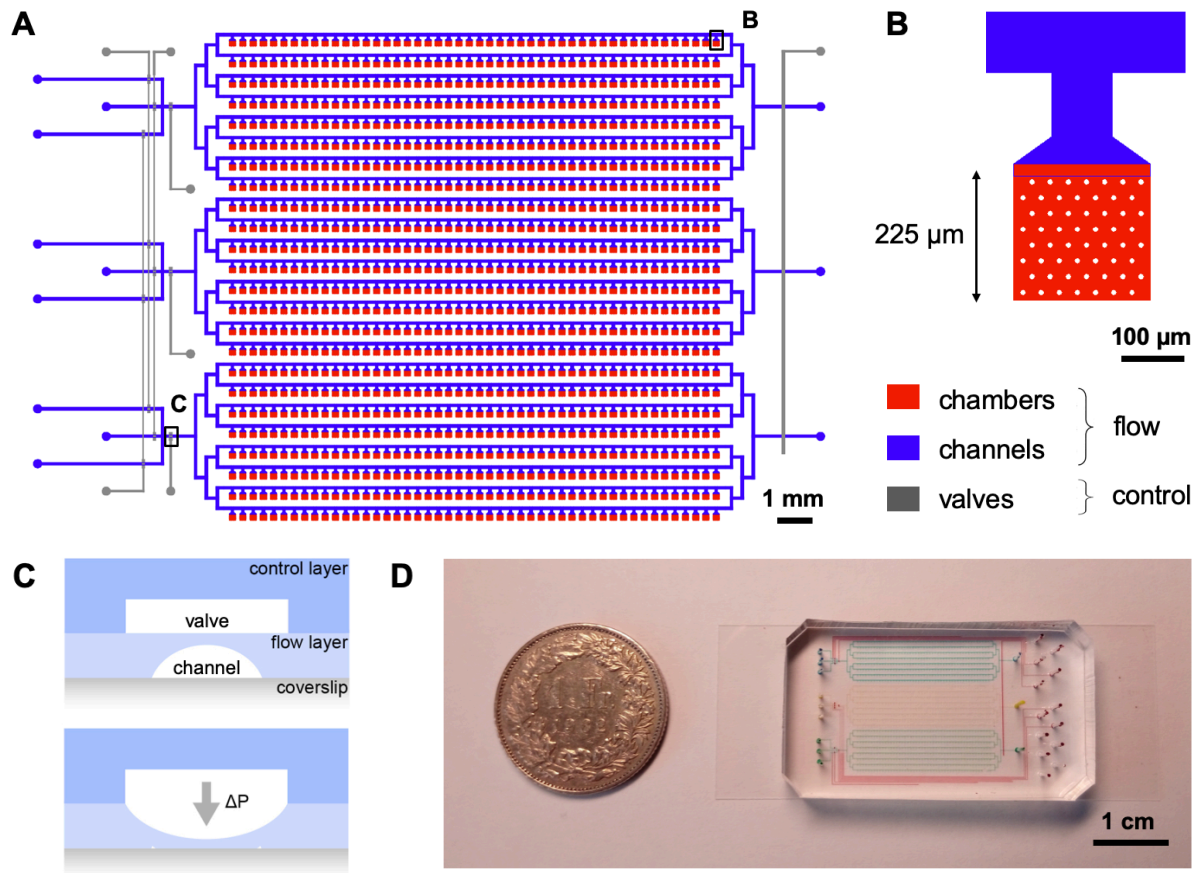


**Figure 4.1: A microfluidic screening platform for high-content UPEC imaging.** (A) Top view of the microfluidic screening platform. The flow layer of the device consists of an array of 1,152 microchambers (red, height: 1.4 μm) connected together with flow channels (blue, height: 12 μm), and arranged in three independent sections (top, middle and bottom). The control layer of the device consists of seven micromechanical valves (grey, height: 12 μm) to allow fast and precise control of medium supply inside the flow channels. Scale bar: 1 mm. (B) Zoom of the boxed area in panel (A) showing the details of a microchamber. Microchambers have dimensions 225 x 225 x 1.4 μm and accommodate PDMS pillars (white circles) to prevent ceiling collapse. Scale bar: 100 μm. (C) Side cut view of the boxed area in panel (A) showing the two layers of the microfluidic device, the upper control layer and the lower flow layer, on top of the microscope coverslip. When pressure is increased in the control valve ( $\Delta P$ ), the PDMS membrane separating the two channels deflects downwards, thereby closing the underlying flow channel. Panel adapted from [Verpoorte, 2017](#). (D) Photograph of the assembled microfluidic screening platform showing the PDMS device bonded to a glass coverslip. The three independent flow sections were injected with blue, yellow and green dyes respectively, while the control valves were injected with a red dye (note that their arrangement is slightly different from the one shown in panel (A)). A one Swiss franc coin is shown for scale. Scale bar: 1 cm.

#### 4.1.2. Optimization of the live UPEC spotting procedure

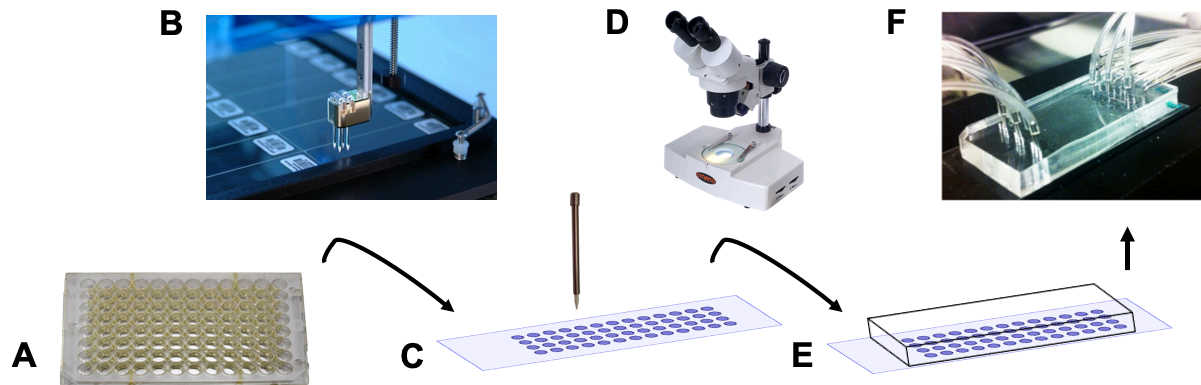


**Figure 4.2: Schematic of the live UPEC spotting procedure.** UPEC transposon mutants constructed in the parental strain CFT073  $\Delta fliC$  sfGFP (again referred to as  $\Delta fliC$ ) were grown overnight in 96-well plates (**A**). Using a high-precision microarrayer (**B**), the content of the 96-well plates was replicated on a glass coverslip (**C**). With the help of a stereomicroscope (**D**), the microfluidic device presented in **Figure 4.1** was manually aligned onto the spots of bacteria (**E**), thereby addressing each spot to a specific microchamber. The whole device was then connected with medium tubing at the inlets and outlets (**F**) before time-lapse imaging on a fluorescence microscope.

The assembled microfluidic platform can either be injected with bacterial cultures, in which case the throughput is limited to the three independent sections of the device (**Figure 4.1D**), or it can be combined with a high-precision microarrayer to create arrays of bacterial mutant spots on microscope coverslips (**Figure 4.2A-C**). In this case, the device is manually aligned on top of the spotted coverslip, so that each mutant fits within one microchamber, where it can later be grown and imaged independently from other mutants (**Figure 4.2D-F**). It turned out however that UPEC were not as resistant to the spotting procedure as were yeast and mycobacteria – for which the original platform was designed – initially resulting in very few bacteria being able to grow back once the device was assembled and perfused with culture medium.

To prevent desiccation of spotted bacteria, various osmoprotectants were therefore added to the spotting medium, including lysine, glycine, glycine betaine, ectoine, glutamate, glutamine, proline, sucrose and trehalose, all chosen from previous work on *E. coli* arrays (Melamed et al., 2011). Ectoine was eventually preferred over the others, as it gave the best UPEC survival rates at the end of the spotting procedure.

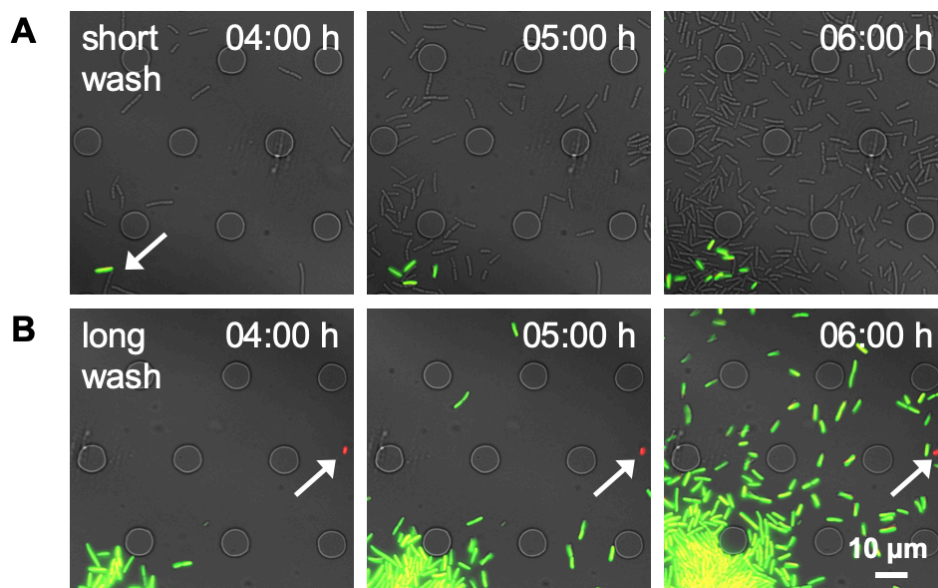


**Figure 4.3: Increasing the ethanol washing time prevents UPEC cross-contamination between microchambers.** (A) Microchambers were spotted in alternation with non-fluorescent or YFP-expressing CFT073  $\Delta fliC$  with a pin washing time of 0.5 second (short wash). Representative time series of a microchamber spotted with non-fluorescent CFT073  $\Delta fliC$  indicates cross-contamination from a YFP-expressing bacterium that is able to grow back (white arrow). (B) Microchambers were spotted in alternation with CFT073  $\Delta fliC$  expressing either YFP or mCherry with a pin washing time of 4 seconds (long wash). Representative time series of a microchamber spotted with YFP-expressing CFT073  $\Delta fliC$  indicates cross-contamination from an mCherry-expressing bacterium that is however unable to grow back (presumably killed by the ethanol wash). In all panels, microchambers were imaged on phase-contrast, green and red fluorescence channels. Scale bar: 10  $\mu$ m for all images.

We next assessed whether UPEC could be carried over by the metallic pins of the arrayer between spotting runs, which could result in undesirable well-to-well



contamination between different UPEC mutants. To this purpose, we spotted in alternation CFT073 strains expressing different fluorescent proteins and evaluated the extent of cross-contamination between microchambers once the device was assembled and perfused. As can be seen in **Figure 4.3**, well-to-well contamination was evident when metallic pins were washed with ethanol for only 0.5 second between each inking (default setting of the arrayer, **Figure 4.3A**) but could be circumvented by increasing the ethanol washing time to 4 seconds (**Figure 4.3B**), resulting in carried-over bacteria being unable to regrow in the assembled device.

Finally, success of the overall device assembly procedure also required optimization of the PDMS-to-glass bonding strength, to ensure that the final device would be water-tight when perfused with medium. PDMS-to-glass bonding is usually performed by oxygen plasma treatment of both surfaces and subsequent thermal curing at 80°C ([Franssila, 2010](#)), which is clearly incompatible with the spotting of live bacteria. This was previously managed by using epoxysilane-coated coverslips ([Dénervaud et al., 2013](#); [Verpoorte, 2017](#)), which bond to PDMS with an acceptable strength upon short incubation at 37°C. However, the discontinuation of these coverslips by their supplier required us to find another solution. We became aware of a similar strategy for PDMS bonding to plastic surfaces ([Tang and Lee, 2010](#)), based on the formation of amine-epoxy bonds between aminosilane-treated PDMS and epoxysilane-treated plastic. Adaptation of this protocol to the assembly of our device proved initially challenging because of the strong bonding it generates, which resulted in flow channels getting irreversibly closed as soon as the control valves were actuated. Using the iterative strategy described in **Section 4.3.8**, we nevertheless managed to identify conditions that resulted in suitable PDMS-to-glass bonding, while also ensuring bacterial growth once the assembled device was perfused with medium.

### 4.1.3. Selection of conditions for the study of UPEC antibiotic persistence

We then searched for a suitable model to study antibiotic persistence of UPEC using clinically and physiologically relevant conditions, while also ensuring good reproducibility and compatibility with our high-content microfluidic screening setup. As for the antibiotic, most current UTI treatment guidelines recommend the use of fosfomycin (FOS) or nitrofurantoin (NIT), both of which have been shown to reach therapeutic concentrations in the urinary tract only, thereby limiting their impact on the gastrointestinal flora and the development of antibiotic resistance ([Gupta et al., 2011](#); [Gardiner et al., 2019](#)). FOS has a well-defined mechanism-of-action and acts by inhibiting bacterial cell wall synthesis, supposedly leading to cell lysis. Since this is readily observable by microscopy, we therefore selected FOS over NIT, for which the mechanism-of-action is not well understood yet.

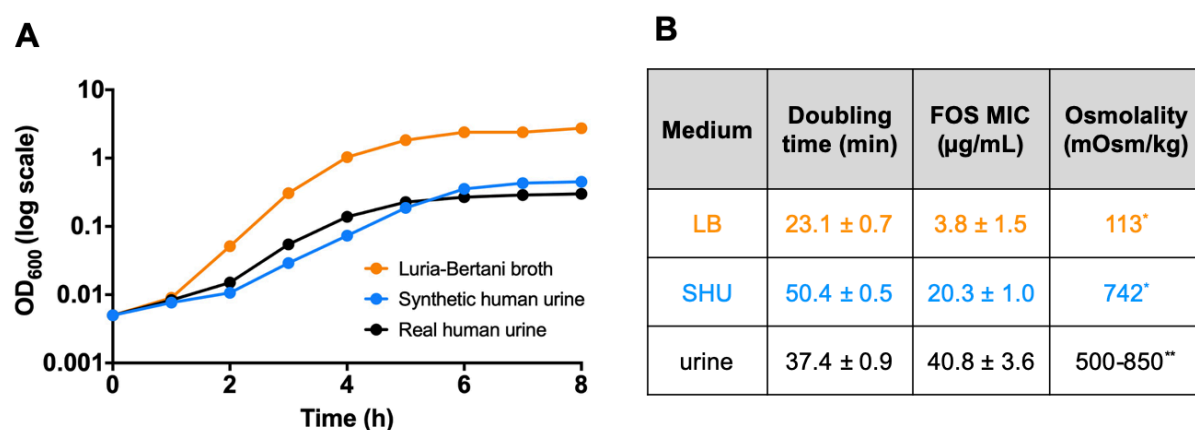


**Figure 4.4: SHU mimics the physiology and FOS response of UPEC in real human urine.**

**(A)** Representative growth curves of the  $\Delta fliC$  parental strain measured in Luria-Bertani broth (LB, orange), synthetic human urine (SHU, blue) or pooled human female urine (black). **(B = Table 4.1)** Corresponding doubling time in exponential phase, minimum inhibitory concentration of fosfomycin (FOS MIC) and osmolality values for the different media. Values for doubling time and FOS MIC are reported as the average  $\pm$  standard deviation of at least  $n = 3$  independent experiments. Osmolality values were either measured experimentally by lab colleague Frédéric Normandeau (\*) or derived from the literature (\*\*, [Mundt et al., 2016](#)).



As for the medium, we became aware of a recently developed formulation of Synthetic Human Urine (SHU, [Ipe et al., 2016](#)), based on eight previously published recipes of artificial urine media. SHU recapitulates the main features of human urine – namely its high osmolality, low pH and the presence of amino acids as carbon source – while still providing chemical definition, thus avoiding the problem of batch-to-batch variation encountered with real urine. As expected, we observed that the physiology of CFT073 in human urine was better approximated when using SHU instead of LB, both in terms of growth (**Figure 4.4A**) and susceptibility to fosfomycin (**Figure 4.4B**). Importantly, the osmolality value measured for SHU was in the range of that observed in real urine, as opposed to LB, which has a much lower osmolality (**Figure 4.4B**).

#### **4.1.4. SHU provides a good model for UPEC persistence to FOS treatment**

We next asked whether UPEC treatment with FOS in SHU displayed hallmarks of bacterial persistence. We therefore performed SHU time-kill assays of CFT073 in the presence of increasing concentrations of FOS (**Figure 4.5A**). At all concentrations tested, time-kill curves showed evidence of biphasic killing (highlighted in **Figure 4.5B**), indicating the presence of a subpopulation of persister cells that are killed at a slower rate than the bulk of the population. Interestingly, the level of persistence decreased with increasing FOS concentrations, although less so for concentrations high above the MIC (**Figure 4.5A**, 10X MIC and 20X MIC, the testing of higher FOS concentrations was precluded by the limit of detection of the assay). Overall, these results validate the existence of UPEC persisters during FOS treatment in SHU.

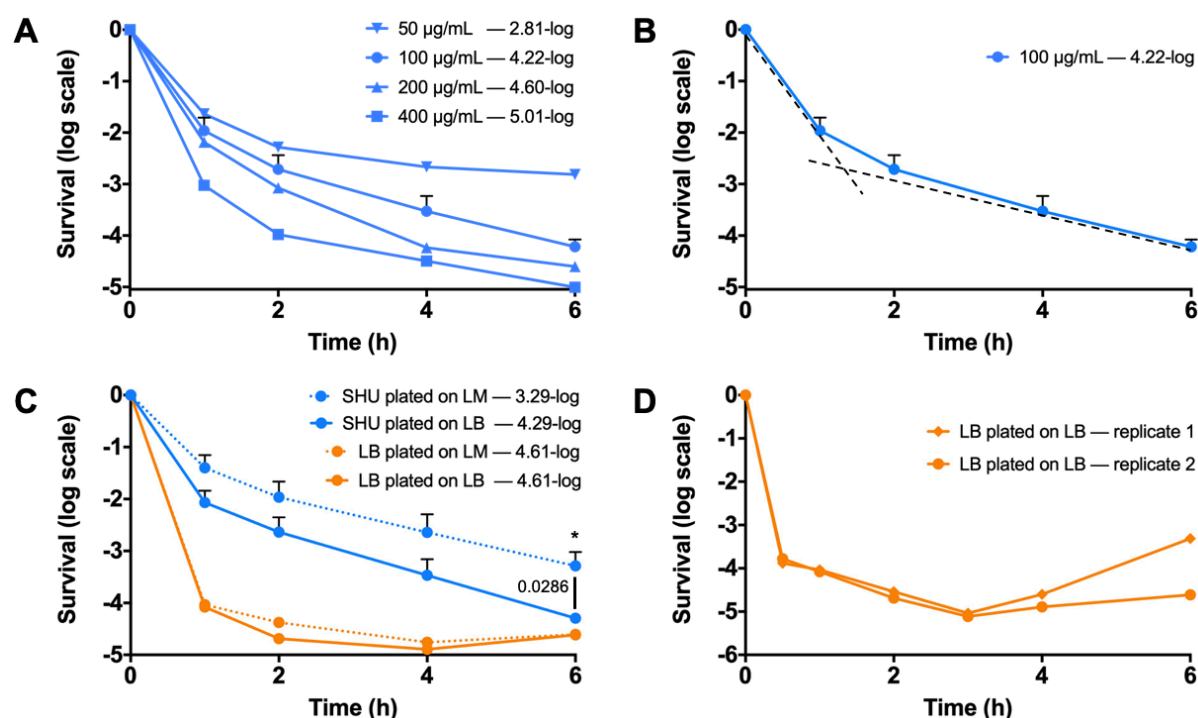


**Figure 4.5: SHU provides a good model for UPEC persistence to FOS treatment.** (A) Time-kill curves of the  $\Delta fliC$  parental strain in the presence of 2.5X FOS MIC (down-pointing triangles, 50  $\mu\text{g/mL}$  FOS), 5X FOS MIC (circles, 100  $\mu\text{g/mL}$  FOS), 10X FOS MIC (up-pointing triangles, 200  $\mu\text{g/mL}$  FOS) or 20X FOS MIC (squares, 400  $\mu\text{g/mL}$  FOS) in SHU, recorded by CFU plating on LB agar plates.  $n = 7$  independent experiments for 5X FOS MIC;  $n = 1$  for the other conditions; symbols indicate mean; error bars indicate standard deviation. (B) Dotted lines highlight biphasic killing of  $\Delta fliC$  in the presence of 5X FOS MIC in SHU. (C) Time-kill curves of  $\Delta fliC$  in the presence of 5X FOS MIC in either SHU (blue, 100  $\mu\text{g/mL}$  FOS) or LB (orange, 20  $\mu\text{g/mL}$  FOS), recorded by CFU plating on either LB agar plates (full lines) or L-form medium (LM) agar plates (dotted lines).  $n = 4$  independent experiments for SHU killing assays;  $n = 1$  for LB killing assays; symbols indicate mean; error bars indicate standard deviation;  $P$ -values were calculated using Welch's t-test comparing survival on LB and LM at each timepoint for SHU killing assays;  $P$ -values  $> 0.05$  are not shown. (D) Time-kill curves of  $\Delta fliC$  in the presence of 5X FOS MIC in LB (corresponding to 20  $\mu\text{g/mL}$  FOS), recorded by CFU plating on LB agar plates, shown for two independent experiments (circles and diamonds). In all panels, the values indicated next to each condition correspond to the extent of bacterial killing at 6 h.

CFU counts for SHU time-kill assays were initially recorded using dilution plating on LB agar plates. However, a recent study showed that clinical UPEC isolates treated

with FOS in real urine could readily convert to cell-wall-deficient forms, which were then able to proliferate on osmoprotective medium but would be lysed on medium without osmotic support (Mickiewicz et al., 2019). Considering that SHU and real urine have a comparably high osmolality (**Figure 4.4B**), we hypothesized that SHU might also support UPEC conversion to cell-wall-deficient forms and that these forms would most likely get killed when plated on low-osmolality LB agar plates. To test this hypothesis, we replicated SHU time-kill assays by recording CFU counts on osmoprotective L-form medium (LM), prepared as described by the same study (Mickiewicz et al., 2019). Remarkably, we observed a significant 10-fold increase in UPEC survival at 6 h on LM compared to LB (**Figure 4.5C**, blue curves), which seems to indicate the ability of UPEC to convert to cell-wall-deficient forms upon FOS treatment in SHU.

We then performed the same set of experiments treating CFT073 in LB liquid medium. In this case, no appreciable difference in survival was observed between LM and LB agar plates, and the overall survival was lower than in SHU (**Figure 4.5C**, orange curves). This seems to indicate that low-osmolality LB medium does not support conversion of UPEC to cell-wall-deficient forms, therefore resulting in increased killing by FOS. Yet, it is worth noting the appearance of FOS-resistant mutants after 4 h in LB time-kill assays (**Figure 4.5D**). Resistance to FOS has been shown to rapidly arise *in vitro* due to mutations in transport systems required for drug uptake and is thought to be an artifact of nutrient-rich media. Indeed, cases of clinical resistance to FOS are relatively rare, presumably because of the fitness cost associated with these mutations in nutrient-poor conditions (Silver, 2017). Accordingly, we did not observe the appearance of FOS-resistant clones in SHU time-kill assays (**Figure 4.5C**). Taken

together, these results clearly establish SHU as a better model than LB for the study of UPEC persistence to FOS, and highlight the importance of using osmolality-adapted media to accurately record survival of osmolality-sensitive bacterial forms.

#### 4.1.5. Time-lapse microscopy allows single-cell observation of UPEC persisters to FOS in SHU

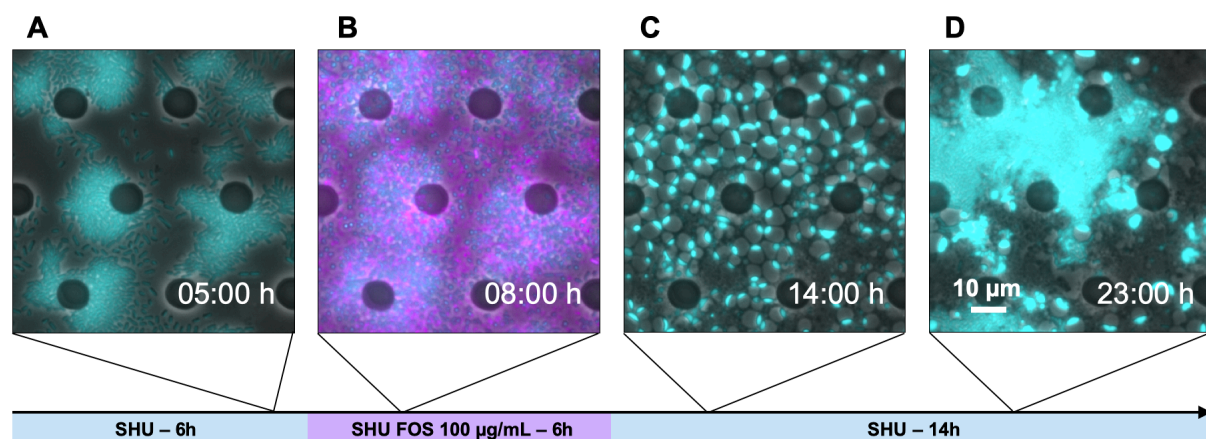


**Figure 4.6: FOS treatment dynamics of UPEC in SHU can be followed by time-lapse microscopy using the microfluidic screening platform.** Fluorescence time series of  $\Delta fliC$  (shown in cyan) during treatment with 5X FOS MIC in SHU (corresponding to 100  $\mu\text{g/mL}$  FOS). Medium switch is monitored through the addition of sulforhodamine (shown in magenta) to the medium containing FOS. Representative images were taken: **(A)** 5 h after device assembly, showing bacterial growth in SHU. **(B)** 2 h after addition of FOS, when bacteria start lysing. **(C)** 2 h after FOS washout, showing incomplete lysis due to conversion to cell-wall-deficient forms. **(D)** 11 h after FOS washout, showing a focus of bacterial regrowth. In all panels, microchambers were imaged on phase-contrast, green (shown in cyan) and red (shown in magenta) fluorescence channels. Scale bar: 10  $\mu\text{m}$  for all images.

To circumvent the need for solid media to visualize bacterial regrowth, we took advantage of the microfluidic platform presented in **Section 4.1.1** and monitored FOS-treated UPEC at the single-cell level during antibiotic-induced killing and subsequent recovery in SHU. The microfluidic sequence comprised three phases (**Figure 4.6**):

1. UPEC were first grown for 6 h in SHU, until forming sizeable microcolonies inside the microchambers of the device (**Figure 4.6A**)
2. for the next 6 h, UPEC were perfused with SHU supplemented with 100 µg/mL FOS, corresponding to 5X MIC for CFT073 (**Figure 4.6B**)
3. UPEC were then allowed to recover for 14 h in antibiotic-free SHU, until persister regrowth became evident (**Figure 4.6C-D**)

The duration of FOS treatment was set to 6 h based on results from time-kill assays (**Figure 4.5**). Likewise, the concentration of FOS was set to 5X MIC, in order to ensure killing of susceptible cells, while still enabling persisters to regrow within an acceptable time frame in the microfluidic device.

Inspection of time-lapse movies confirmed that UPEC were able to convert to cell-wall-deficient forms upon FOS treatment in SHU (**Figure 4.6C**), and that some of these forms were then able to revert back to rod-shaped bacteria upon FOS washout (**Figure 4.7A**). More precisely, rod-shaped bacteria (**Figure 4.7A**, white arrows) would first start bulging at mid-cell, presumably where FOS-induced inhibition of peptidoglycan assembly occurs (**Figure 4.7A**, magenta arrows). The periplasmic space would then dramatically expand, leading to almost complete dissociation of the outer and inner membranes, the latter of which could be unmistakably identified since it encases cytoplasmic sfGFP (**Figure 4.7A**, yellow circles). After FOS washout, cell-wall-deficient forms that were eventually able to resume cell division would invariably show a similar sequence of events, where the cytoplasm would first spread against the outer membrane, after which a protrusion would form and break down into a few newborn cells (**Figure 4.7A**, yellow arrows). These would initially show aberrant morphologies, until regular rod-shaped bacteria would form again after a few rounds of division



(Figure 4.7A, white arrows). The whole sequence is reminiscent of what was recently shown by [Mercier et al., 2014](#) and [Mickiewicz et al., 2019](#) for *E. coli* L-forms. On the contrary, inspection of time-lapse movies recorded in LB showed that UPEC would lyse very quickly in response to FOS treatment (Figure 4.7B), confirming the previous hypothesis that this medium does not support conversion to cell-wall-deficient forms.

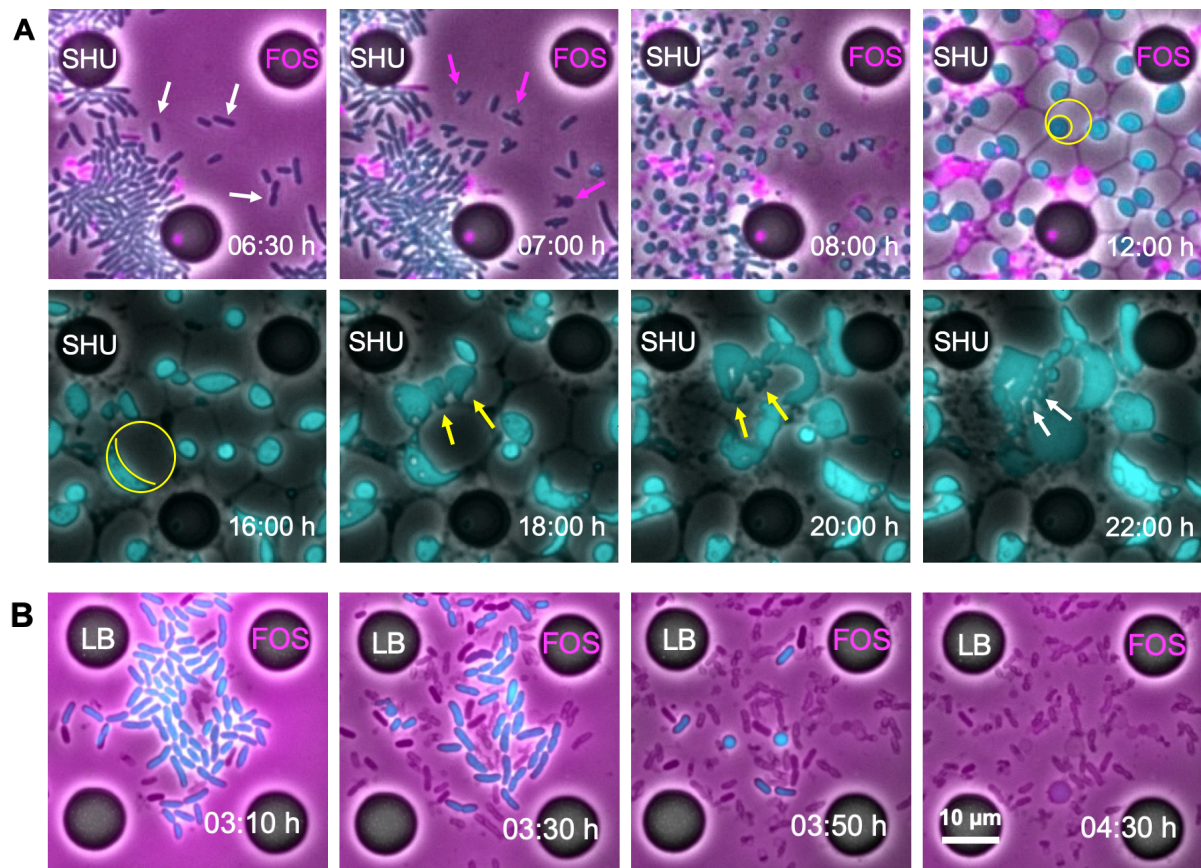


**Figure 4.7: UPEC can convert to cell-wall-deficient bacterial forms upon FOS treatment in SHU but not in LB.** (A) Fluorescence time series of  $\Delta fliC$  during treatment with 5X FOS MIC in SHU (corresponding to 100  $\mu\text{g/mL}$  FOS), showing that UPEC converts to cell-wall-deficient forms upon FOS treatment, and reverts back to rod-shaped bacteria upon FOS washout. White arrows indicate rod-shaped bacteria at the beginning and at the end of the experiment. Magenta arrows indicate bacteria that have started bulging due to FOS inhibition of cell-wall synthesis. Yellow circles indicate cell-wall-deficient forms, with the inner circle depicting the position of the inner membrane and the outer circle the position of the outer membrane. Yellow arrows indicate cell-wall-deficient forms that are able to resume cell

division after FOS washout. **(B)** Similar sequence of events during treatment of  $\Delta fliC$  with 5X FOS MIC in LB (corresponding to 20  $\mu\text{g/mL}$  FOS), showing that bacteria are unable to convert to cell-wall-deficient forms (note that in this case, medium switch was performed 3 h after initial growth in LB due to the shorter doubling time of UPEC in this medium). Microchambers were imaged on phase-contrast, green (shown in cyan) and red (shown in magenta) fluorescence channels. Images in **(B)** are a courtesy of lab colleague Frédéric Normandeau. Scale bar: 10  $\mu\text{m}$  for all images.

#### 4.1.6. High-content microfluidic screening identifies UPEC mutants with altered persistence to FOS in SHU

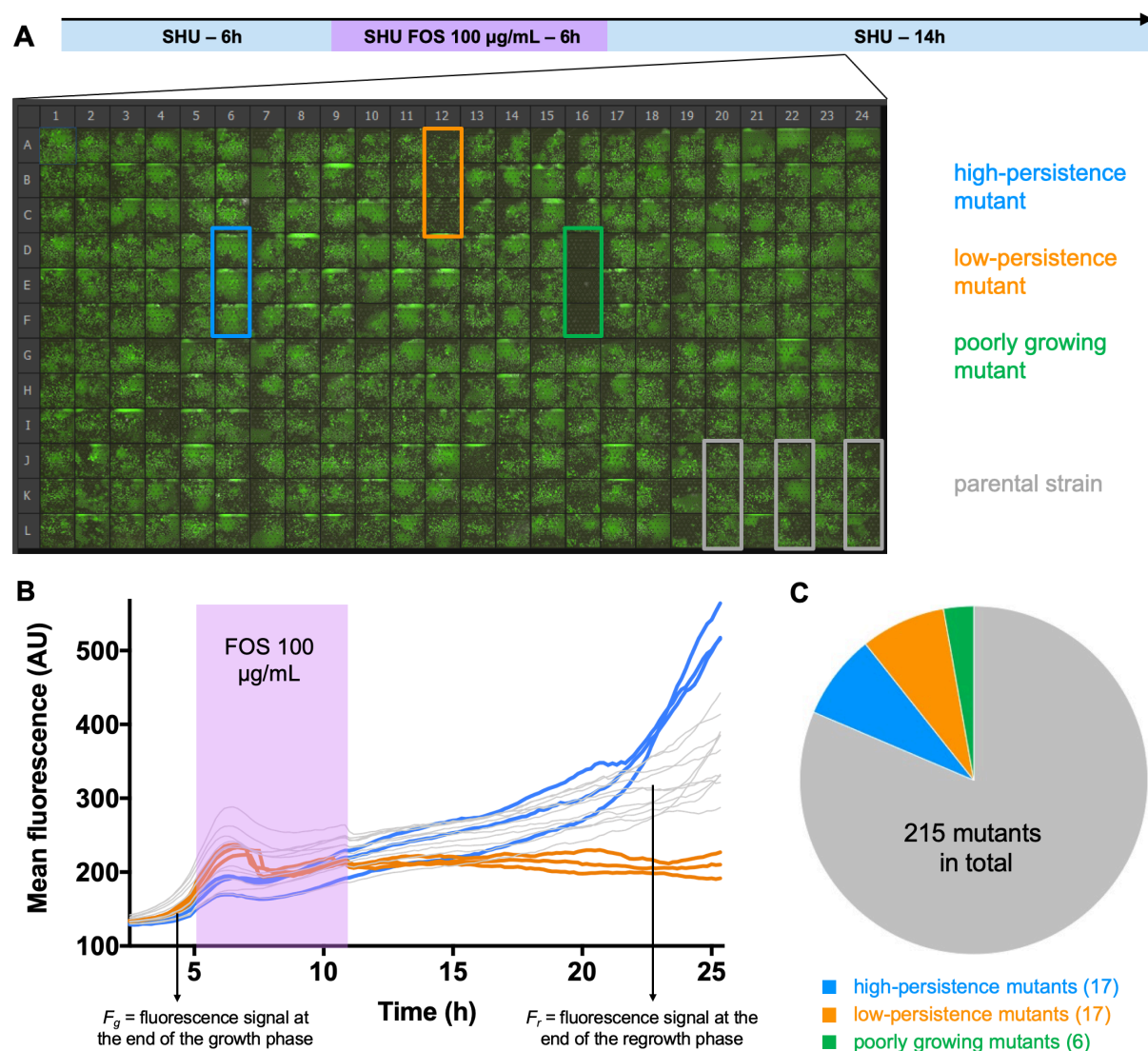


**Figure 4.8: Microfluidic high-content screening identifies UPEC mutants with altered persistence to FOS in SHU. (A)** Fluorescence snapshots taken 11 h after FOS washout,

showing regrowth of UPEC transposon mutants in microchambers. Blue: triplicate corresponding to a high-persistence mutant; orange: triplicate corresponding to a low-persistence mutant; green: triplicate corresponding to a poorly growing mutant; grey: triplicates corresponding to the  $\Delta fliC$  parental strain. **(B)** Individual traces of mean GFP fluorescence intensity in the corresponding microchambers. The regrowth ratio in each microchamber was calculated by dividing the fluorescence at regrowth  $F_r$  by the fluorescence at growth  $F_g$ . Mutants with altered persistence to FOS were then identified by running a Welch-adjusted t-test of their regrowth ratio values against those of the  $\Delta fliC$  parental strain. **(C)** Proportion of high-persistence (blue), low-persistence (orange) and poorly growing mutants (green) identified during primary screen.

Like in the adhesion screen presented in **Chapter 3**, the CFT073  $\Delta fliC$  sfGFP strain (referred to as  $\Delta fliC$ ) served as the parental strain for transposon mutagenesis. Due to recurrent technical issues with the microarrayer used for the spotting procedure, we were only able to screen a small-scale library corresponding to 215 transposon mutants. In this primary screen, mutants were arrayed in triplicates of microchambers along with three triplicates of the  $\Delta fliC$  parental strain, and time-lapse movies were recorded using the microfluidic sequence previously described (**Figure 4.8A**). Mutants that displayed decreased (**Figure 4.9C**) or increased (**Figure 4.9B**) persistence to FOS in SHU were identified by comparing their regrowth ratio to that of the  $\Delta fliC$  parental strain (**Figure 4.9A**), using the procedure explained in **Figure 4.8B**. This resulted in the identification of 17 low-persistence mutants, 17 high-persistence mutants (7.9 % of the total screened in both cases), and 6 mutants that grew poorly in SHU and were discarded at this step (**Figure 4.8C**). We visually inspected time-lapse movies corresponding to the identified mutants to confirm or infirm their altered persistence phenotype. This allowed for example the distinction of a mutant for which the low-persistence annotation was most likely due to increased lysis of cell-wall-deficient forms during FOS washout (**Figure 4.9D**), therefore resulting in lower GFP



fluorescence than the parental strain throughout the recovery phase. Yet, this mutant regrew at a level similar to the parental strain at the end of the sequence (**Figure 4.9A,D**) and is thus unlikely to have a *bona fide* low-persistence phenotype.

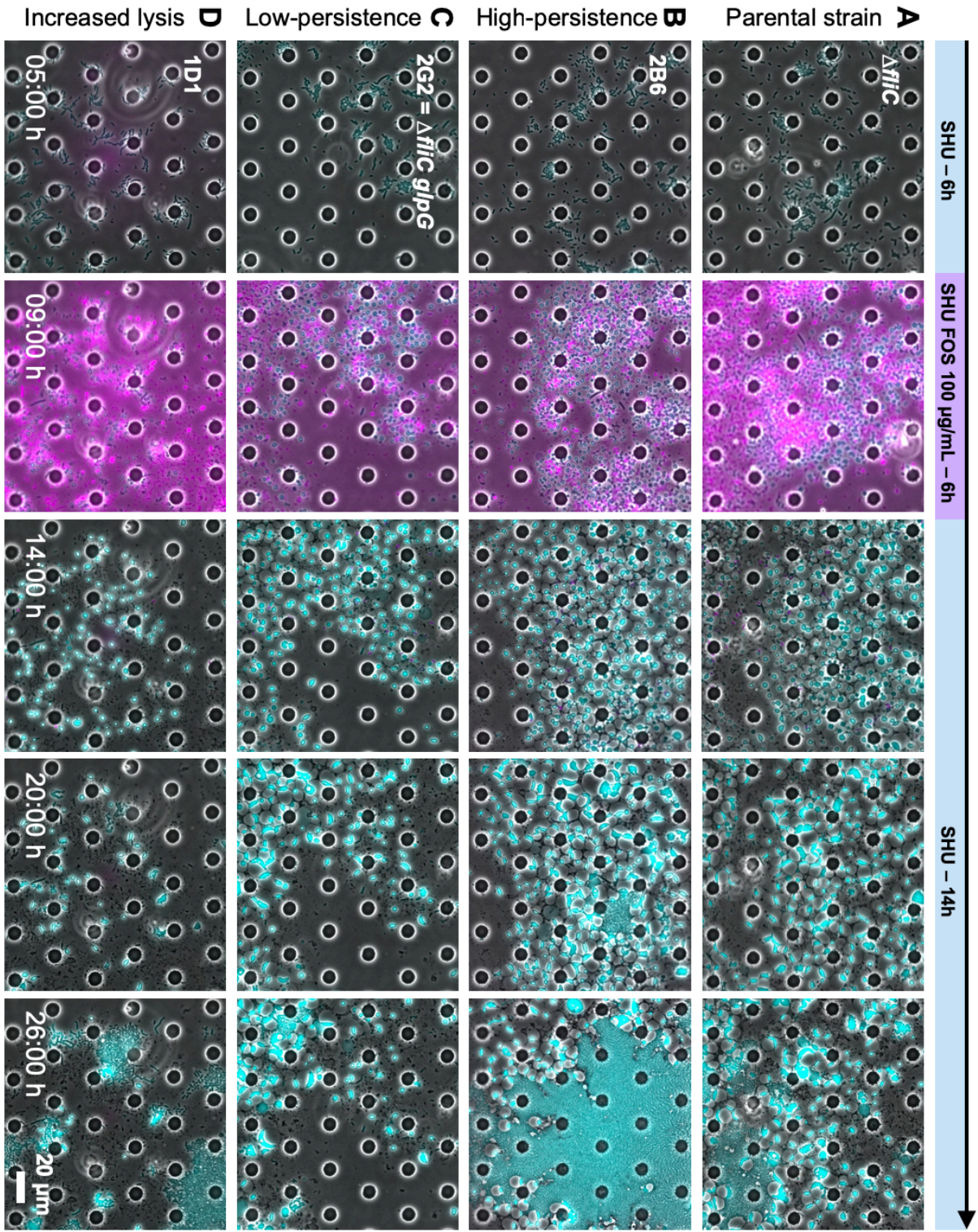


**Figure 4.9: Examples of UPEC mutants with altered persistence identified during primary screen.** Fluorescence time series of different UPEC mutants during treatment with 100 µg/mL FOS in SHU: **(A)**  $\Delta fliC$  parental strain; **(B)** example of a high-persistence mutant, eventually rejected during rescreening; **(C)** example of a low-persistence mutant, eventually confirmed during rescreening; **(D)** example of a mutant identified as low-persistence in the primary screen, that actually shows increased lysis during FOS washout but regrowth comparable to the  $\Delta fliC$  parental strain. In all panels, microchambers were imaged on phase-contrast, green (shown in cyan) and red (shown in magenta) fluorescence channels. Scale bar: 20 µm for all images.

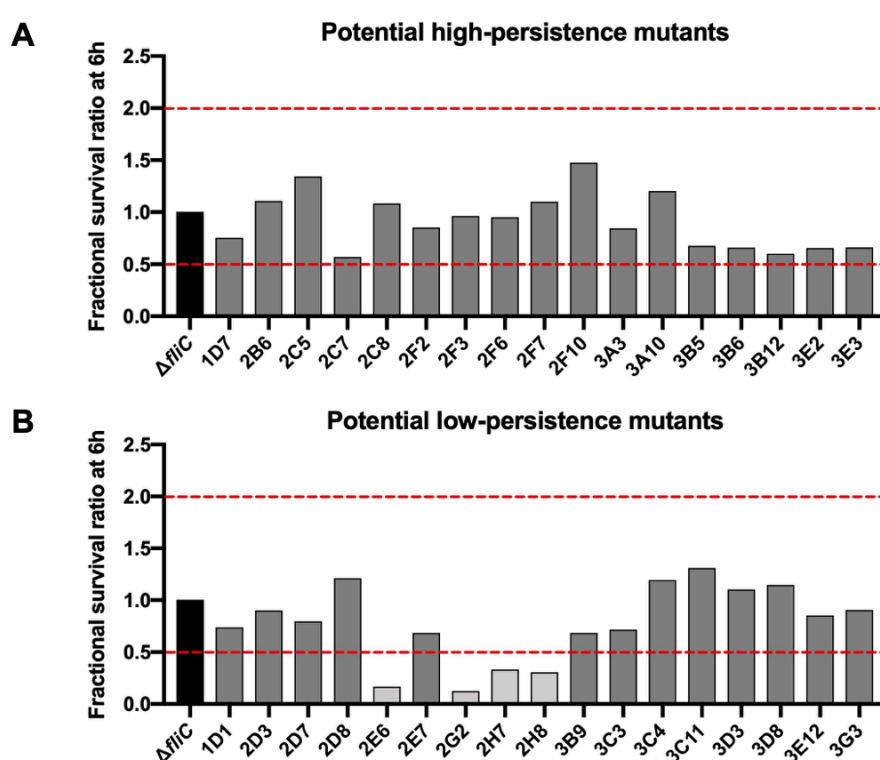


**Figure 4.10: Validation of UPEC mutants with altered persistence identified during primary screen.** Fractional survival ratio (FSR) at 6 h for potential high-persistence mutants **(A)** and low-persistence mutants **(B)** identified during primary screen, calculated as the normalized survival ratio after 6 h treatment with 100 µg/mL FOS in SHU compared to the  $\Delta fliC$  parental strain (black). Survival ratios were recorded by CFU plating on L-form medium (LM) agar plates at 0 and 6 h. Red dotted lines indicate a 2-fold increased or decreased FSR. Mutants with a  $\geq 2$ -fold decreased FSR (light grey) were selected for further analysis and disrupted genes were identified as described in **4.3. Materials and methods**. Other mutants (dark grey) were rejected at this step. Data in this figure was generated with the help of Master student Anouk Rossier.

Mutants identified in the primary screen were rescreened using a variation of the time-kill assay presented earlier: their survival after 6 h FOS treatment in SHU was assessed by CFU plating on L-form medium (LM), and compared to that of the parental strain to calculate their “fractional survival ratio” at 6 h (FSR, see **Figure 4.10**). Only mutants with a  $\geq 2$ -fold increased or decreased FSR were considered to have true altered persistence phenotypes. Using this criterion, none of the 17 previously identified high-persistence mutants were validated (**Figure 4.10A**). On the other hand, 4 out of 17 previously identified mutants were confirmed to have a low-persistence phenotype (**Figure 4.10B**) and were therefore selected for further analysis.

#### 4.1.7. Characterization of mutants with decreased persistence to FOS in SHU

To our surprise, three of the confirmed low-persistence “hits” mapped to the *waa* gene cluster, responsible for synthesis of the core oligosaccharide (core-OS) of the UPEC lipopolysaccharide (LPS) – more precisely to genes *waaV*, *waaY* and *waaJ* – while the remaining transposon insertion mapped to the gene *glpG* of poorly defined function (**Figure 4.11D**). The four transposon mutants had no growth defect in SHU compared to the parental strain (**Figure 4.11A,D**). Interestingly, the  $\Delta fliC$  *glpG*-Tn mutant had an approximately 3-fold lower FOS MIC than the parental strain (**Figure 4.11B,D**), indicative of a mutant with increased susceptibility to FOS rather than decreased persistence *per se*. Corroborating this hypothesis is the fact that *glpG* clusters in an operon upstream of *glpR*, the repressor of the glycerol-3-phosphate (G3P) regulon. The transposon insertion in *glpG* could therefore have a polar effect on the expression of *glpR*, resulting in derepression of the G3P regulon and increased synthesis of the G3P importer GlpT, which is also used for FOS uptake. As a consequence, the  $\Delta fliC$



*glpG*-Tn mutant would effectively “see” a higher cytoplasmic concentration of FOS than the parental strain, thus explaining its lower survival (**Figure 4.11C,D**).

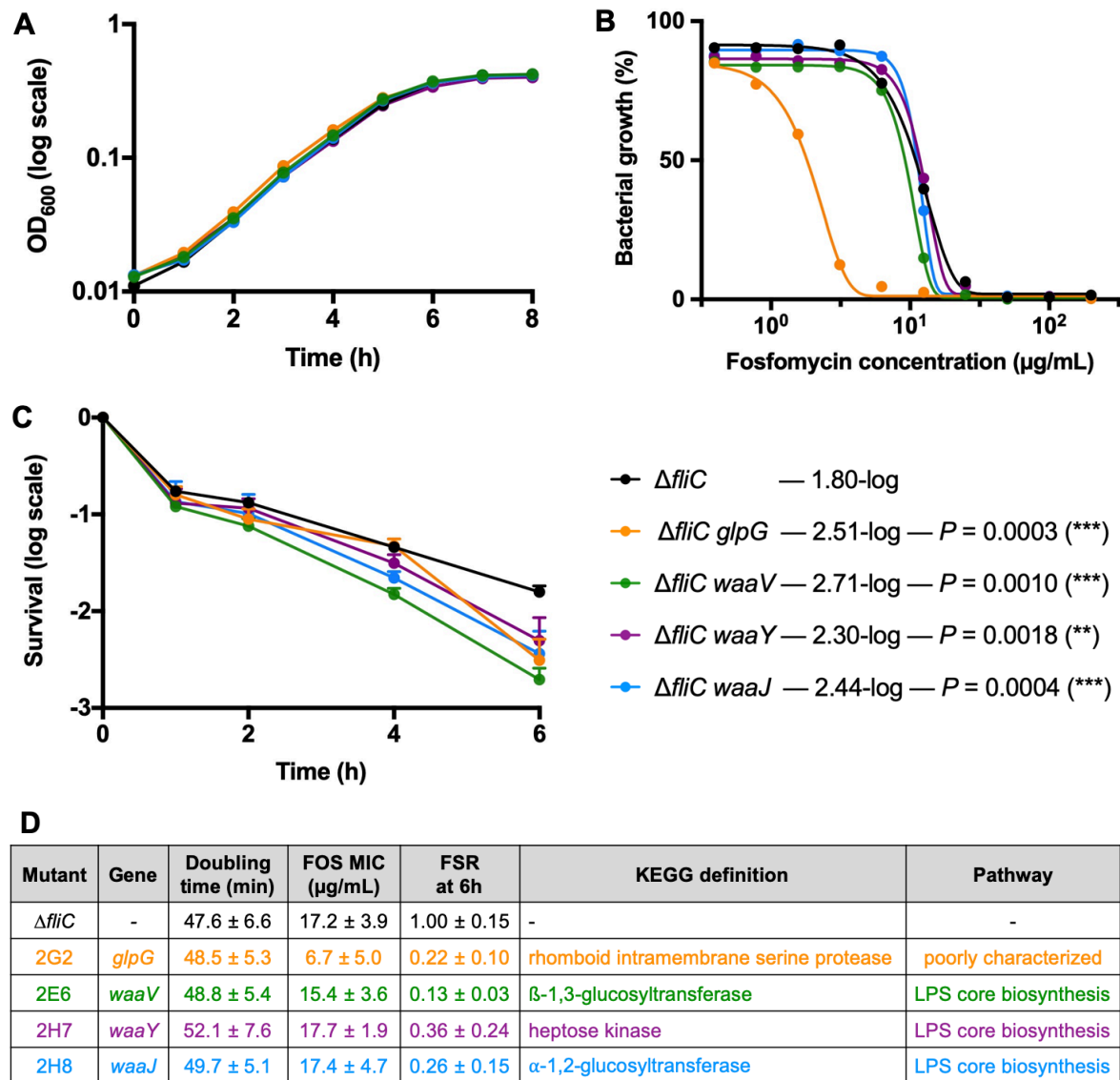


**Figure 4.11: Characterization of UPEC mutants with confirmed decreased persistence to FOS in SHU.** (A,B) Representative growth curves (A) and FOS MIC determination curves (B) in SHU for the  $\Delta fliC$  parental strain (black) and low-persistence mutants  $\Delta fliC glpG$ -Tn (orange),  $\Delta fliC waaV$ -Tn (green),  $\Delta fliC waaY$ -Tn (purple), and  $\Delta fliC waaJ$ -Tn (blue). (C) Time-kill curves of the indicated UPEC strains in the presence of 100  $\mu\text{g/mL}$  FOS in SHU, recorded by CFU plating on L-form medium (LM) agar plates.  $n = 3$  independent experiments; symbols indicate mean; error bars indicate standard deviation;  $P$ -values were calculated using Welch’s t-test comparing survival at 6 h to the  $\Delta fliC$  parental strain, and are indicated next to each

condition along with the extent of bacterial killing. Data in panel **(C)** was generated with the help of Master student Anouk Rossier. **(D = Table 4.2)** Corresponding doubling time in exponential phase, minimum inhibitory concentration of fosfomycin (FOS MIC) and fractional survival ratio (FSR) at 6 h, all measured in SHU for the indicated UPEC strains. Values are reported as the average  $\pm$  standard deviation of  $n \geq 3$  independent experiments. Also indicated are the disrupted genes in each mutant along with their KEGG annotation.

On the contrary, the  $\Delta fliC$  *waaV*-Tn,  $\Delta fliC$  *waaY*-Tn and  $\Delta fliC$  *waaJ*-Tn mutants all had a FOS MIC value similar to that of the parental strain (**Figure 4.11B,D**), indicating that they were indeed true low-persistence mutants. This was confirmed by recording their time-kill curves during FOS treatment in SHU, which showed clear biphasic killing with significantly lower survival at 6 h compared to the parental strain (**Figure 4.11C,D**). Of note, these time-kill assays were performed using a slightly different protocol from the one used in **Figure 4.5** (see details in **4.3. Materials and methods**). The absence of centrifugation and spreading steps in this second protocol presumably reduced mechanical stress on FOS-treated bacteria, which could explain why survival at 6 h for the parental strain was higher than in **Figure 4.5**.

Inspection of time-lapse movies corresponding to mutants  $\Delta fliC$  *waaV*-Tn (**Figure 4.12B**) and  $\Delta fliC$  *waaJ*-Tn (**Figure 4.12D**) showed a singular behavior during early recovery phase in SHU. For these mutants, the cytoplasm of cell-wall-deficient forms did not spread as much against the outer membrane as for the parental strain (**Figure 4.12A**), but rather remained round for an extended period of time after FOS washout, resulting in very few bacteria being eventually able to form cytoplasmic protrusions and reinitiate cell division. On the other hand, cell-wall-deficient forms corresponding to the mutant  $\Delta fliC$  *waaY*-Tn (**Figure 4.12C**) initially expanded their cytoplasm like the parental strain (**Figure 4.12A**) but then seemed to lyse more easily, leading here as

well to less bacterial regrowth. Taken together, the results from **Figure 4.11** and **Figure 4.12** indicate a link between defective LPS core synthesis and decreased persistence to FOS treatment in SHU.

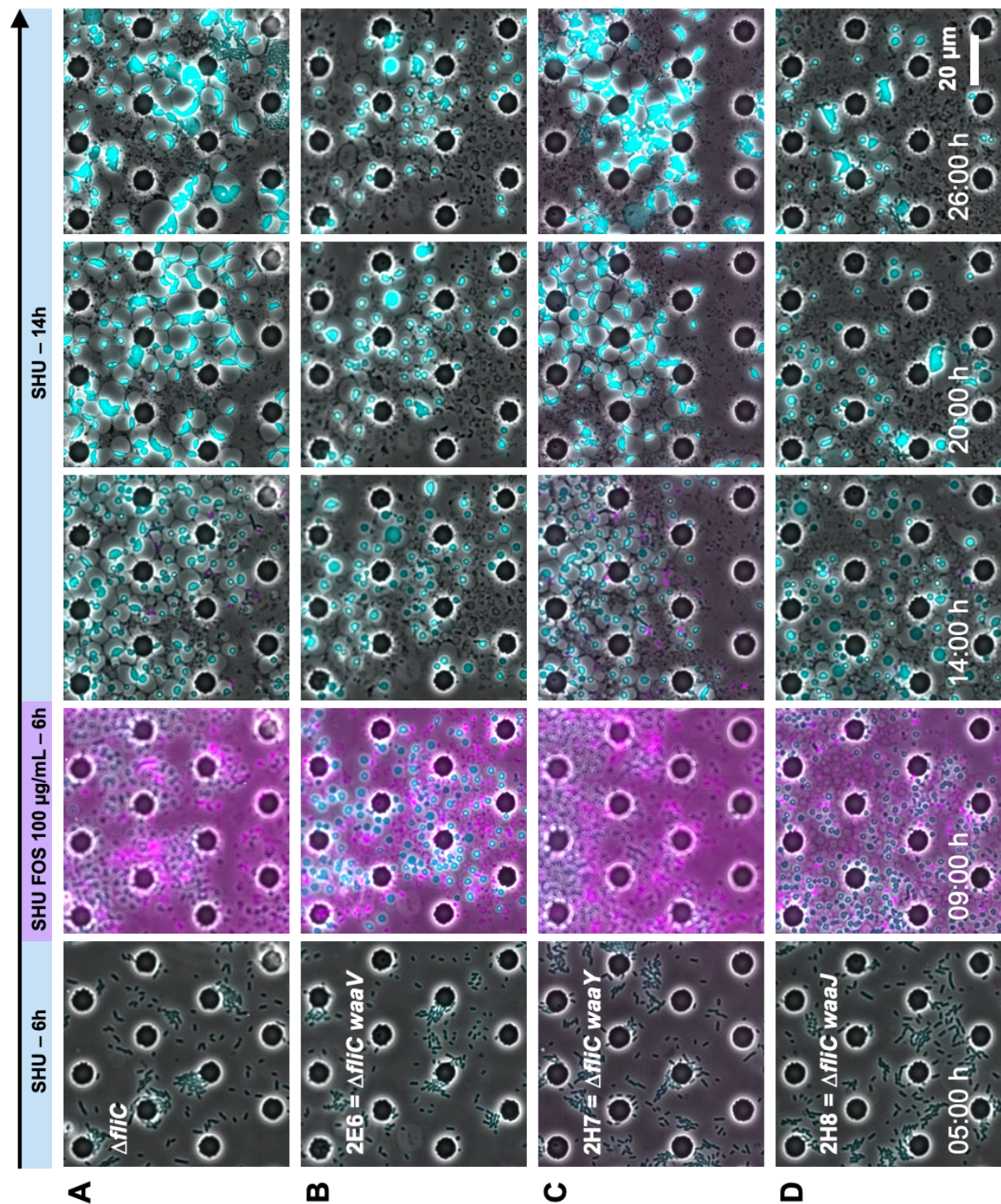


**Figure 4.12: FOS treatment dynamics of UPEC mutants with confirmed decreased persistence in SHU.** Fluorescence time series during FOS treatment in SHU shown for the  $\Delta fliC$  parental strain **(A)**, as well as low-persistence mutants  $\Delta fliC waaV$ -Tn **(B)**,  $\Delta fliC waaY$ -Tn **(C)**, and  $\Delta fliC waaJ$ -Tn **(D)**. In all panels, microchambers were imaged on phase-contrast, green (shown in cyan) and red (shown in magenta) fluorescence channels. Scale bar: 20  $\mu$ m for all images.

#### **4.1.8. LPS core synthesis plays a key role in UPEC persistence to FOS in SHU**

To confirm the connection between persistence and core-OS synthesis, we took advantage of the results from the adhesion screen performed in **Chapter 3**. Several transposon insertions corresponding to high-adhesion mutants were indeed identified in the *waa* gene cluster, as well as in the gene *rfaH* coding for a transcriptional antiterminator regulating the expression of *waa* genes (**Table 5.1**). We therefore assessed the persistence of these mutants to FOS in SHU using the simplified version of the time-kill assay presented earlier. Confirming our hypothesis, all *waa* mutants tested showed decreased persistence compared to the  $\Delta fliC$  parental strain, with a  $\geq$  2-fold decreased FSR for all but one of them (**Figure 4.13A**). Notably, some of these mutants have defects in the formation of side residues of the LPS core, while others are defective in synthesis of the main chain of the core (**Figure 4.13B,C**). The latter are therefore likely to have a truncated core, with no possibility to assemble the LPS O-antigen (**Figure 4.13C**). To further evaluate the impact of the O-antigen on persistence to FOS in SHU, we measured the survival of high-adhesion mutants with transposon insertions in genes related to O-antigen synthesis (**Table 5.1**). Mutants with defective O-antigen synthesis also had decreased persistence compared to the  $\Delta fliC$  parental strain, although the effect was less marked than for *waa* mutants (**Figure 4.13A**). We last measured the survival of high-adhesion mutants with transposon



insertions in genes linked to capsule synthesis (**Table 5.1**). Although these mutants showed a trend towards lower survival, none of them had a  $\geq 2$ -fold decreased FSR, indicating a somewhat less important role of the capsule in persistence to FOS in SHU (**Figure 4.13A**). Overall, these results identify the LPS, and the LPS core synthesis in particular, as a key component for UPEC survival to FOS treatment in SHU, presumably as the bacterial outer membrane allows cell-wall-deficient forms to maintain their integrity in the absence of peptidoglycan.

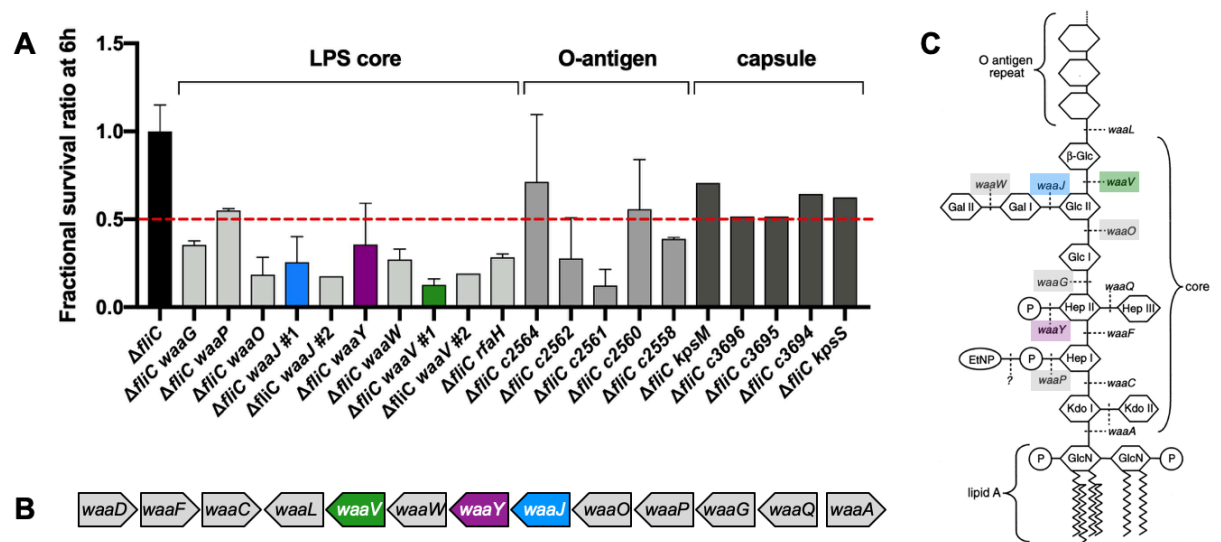


**Figure 4.13: Persistence phenotypes of transposon UPEC mutants with impaired LPS core, O-antigen or capsule synthesis.** **(A)** Fractional survival ratio (FSR) at 6 h for transposon mutants with impaired LPS core (light grey), O-antigen (grey) or capsule (dark grey) synthesis, calculated as the normalized survival ratio after 6 h treatment with 100  $\mu$ g/mL FOS in SHU compared to the  $\Delta fliC$  parental strain (black). Survival ratios were recorded by CFU plating on L-form medium (LM) agar plates at 0 and 6 h.  $n = 4$  for the  $\Delta fliC$  parental strain,  $n \geq 2$  for LPS core and O-antigen mutants;  $n = 1$  for capsule mutants; bars indicate mean; error bars indicate standard deviation; red dotted line indicates a 2-fold decreased FSR. **(B)** Genetic organization of the *waa* gene cluster in CFT073. **(C)** Structure of the LPS core of CFT073, showing the activity of the Waa enzymes. Genes with a transposon insertion catalogued in the library are colored. Blue: *waaJ*; purple: *waaY*; green: *waaV*; light grey: other *waa* genes. GlcN: D-glucosamine; Hep: L-glycero-D-mannoheptose; P: phosphate; EtNP: 2-aminoethyl phosphate; Glc: D-glucose; Gal: D-galactose. Panel **(C)** is adapted from [Yethon et al., 2000](#). Data in this figure was generated with the help of Master student Anouk Rossier.



#### 4.1.9. LPS synthesis is upregulated in UPEC upon FOS treatment in SHU

Considering the huge increase in periplasmic space observed during FOS treatment of UPEC in SHU (**Figure 4.7A**), we postulated that not only was the outer membrane required for persistence but that there was active outer membrane synthesis in response to FOS treatment. To verify this hypothesis, we treated the  $\Delta fliC$  parental strain with low doses of FOS (0.1X MIC and 1X MIC) in SHU and measured the expression levels of the following genes after 1 h incubation:

- two genes involved in peptidoglycan (PG) synthesis (**Figure 4.14C**):
  - *murA*, whose gene product catalyzes the first committed step in PG synthesis and is the target of FOS
  - *murG*, whose gene product is responsible for the last intracellular step of PG assembly
- four genes involved in lipopolysaccharide (LPS) synthesis (**Figure 4.14B**):
  - *lpxA*, whose gene product catalyzes the first reaction in synthesis of lipid A, which constitutes the innermost region of the LPS
  - *lpxB*, which encodes a glycosyltransferase responsible for generating an intermediate in lipid A synthesis
  - *msbA*, which codes for the flippase that translocates the lipid A-core from the inner to the outer leaflet of the inner membrane
  - *lptD*, whose gene product is involved in LPS assembly at the outer leaflet of the outer membrane

For all genes tested except *lpxA*, the trend was towards increased expression as the concentration of FOS increased (**Figure 4.14A**). More precisely, *murA* and *murG*

showed a mild increase in expression, although not reaching statistical significance, which could denote an attempt to upregulate PG synthesis in order to compensate for FOS-induced inhibition of the whole pathway. More importantly, we observed a significant upregulation of *lpxB* and *msbA* expression, as well as a clear but non-significant upregulation of *lptD* expression (**Figure 4.14A**). This suggests upregulation of LPS synthesis and therefore provides evidence of increased outer membrane synthesis in response to FOS treatment in SHU. Interestingly, both the PG and LPS synthesis pathways use UDP-N-acetylglucosamine (UDP-GlcNAc) as building block (**Figure 4.14B,C**). FOS inhibition of MurA could trigger accumulation of UDP-GlcNAc in the bacterial cytoplasm, thereby prompting its use by the LPS synthesis pathway, which could explain the observed upregulation. This hypothesis remains to be tested.

**Figure 4.14: LPS synthesis is upregulated in UPEC upon FOS treatment in SHU.** (A) Expression levels of genes involved in peptidoglycan synthesis (*murA*, *murG*) and outer membrane synthesis (*lpxA*, *lpxB*, *msbA*, *lptD*) measured by qRT-PCR for the  $\Delta fliC$  parental strain after 1 h incubation without (0X MIC, light grey) or with 2  $\mu\text{g/mL}$  (0.1X MIC, dark grey) and 20  $\mu\text{g/mL}$  (1X MIC, black) FOS in SHU. Relative expression was calculated by normalizing to the expression level of *gapA* and to the expression level of each gene in the

untreated condition.  $n = 3$  independent experiments; bars indicate mean; error bars indicate standard deviation;  $P$ -values were calculated using Student's  $t$ -test comparing treated to untreated conditions;  $P$ -values  $> 0.05$  are not shown. **(B)** Enzymes involved in *E. coli* outer membrane synthesis. Proteins of interest are highlighted in purple. Panel adapted from [Simpson and Trent, 2019](#). **(C)** Enzymes involved in *E. coli* peptidoglycan synthesis. Proteins of interest are highlighted in green. Panel adapted from [Egan et al., 2020](#). In panels **(B,C)**, UDP-N-acetylglucosamine (UDP-GlcNAc) is highlighted in red.

## 4.2. Discussion and outlook

Antibiotic persistence is increasingly viewed as a major cause of recalcitrance of UTIs to antibiotic treatment in the absence of underlying antibiotic resistance, since it allows a small fraction of susceptible bacteria to withstand antibiotic exposure for an extended period of time. Although studied extensively using lab-adapted strains of *E. coli*, there are currently few models to study antibiotic persistence of UPEC under physiologically and clinically relevant conditions. Here, we introduce such a model by looking at UPEC persistence to the cell-wall inhibitor fosfomycin in a recently developed formulation of Synthetic Human Urine. We show that SHU provides a good recapitulation of the physiology of UPEC in real urine, both in terms of growth and FOS susceptibility. The high osmolality of SHU allows UPEC to convert to cell-wall-deficient forms upon FOS exposure, a fraction of which is able to grow back as rod-shaped bacteria upon FOS washout. Using high-content microfluidic screening, we identify a key role for the LPS core in survival and regrowth of cell-wall-deficient forms, which we confirm through targeted analysis of UPEC mutants with defective core-OS synthesis. We further demonstrate that UPEC upregulate LPS synthesis in response to FOS exposure in SHU, which overall establishes the outer membrane as a key component for UPEC survival to FOS treatment.

Our results first highlight the importance of conducting antibiotic persistence studies in media that replicate the environment encountered by pathogenic bacteria during the course of *in vivo* infections. A recent study demonstrated the presence of cell-wall-deficient UPEC forms in fresh urine isolated from patients with recurrent UTIs, and postulated that they may contribute to the recalcitrance of these infections to treatment with antibiotics targeting the cell wall ([Mickiewicz et al., 2019](#)). Accordingly, we find that UPEC are able to convert to cell-wall-deficient forms upon FOS treatment in SHU but not in LB, and that this leads to a 10-fold increase in UPEC survival when treated in SHU rather than LB. These results clearly establish conversion to cell-wall-deficient forms as an important mechanism for surviving FOS exposure. Also supporting this claim is the fact that persistence in SHU drops to the level seen in LB when recovery of cell-wall-deficient forms is prevented by using agar medium without osmotic support. In this case, regrowth presumably stems exclusively from bacteria that remained rod-shaped during the entire duration of FOS treatment and were therefore non-growing at the time of FOS addition, since FOS only targets actively growing cells ([Silver, 2017](#)). Conversely, most of the persisters recovered on osmoprotective agar medium correspond to cells that were actively growing in SHU at the time of FOS addition. This in turn means that the majority of persisters are being overlooked when using media without osmoprotection, and that the mechanisms behind persistence in high-osmolality media are likely to be appreciably different. In particular, the contribution of dormancy to FOS persistence appears to be negligible in a physiologically relevant medium such as SHU.

On the contrary, we see that UPEC conversion to cell-wall-deficient forms upon FOS treatment in SHU is accompanied by active rewiring of the bacterial transcriptome,

with the LPS synthesis pathway being upregulated. Whether this upregulation is actually beneficial to the survival of individual UPEC cells remains to be tested. On one hand, it could have a negative impact on survival by increasing the overall size of cell-wall-deficient UPEC forms, which would result in increased surface tension in the cell envelope according to Laplace's law ([Cadart et al., 2019](#)). On the other hand, it could increase the overall stiffness of the outer membrane through accumulation of LPS molecules, thereby increasing the stability of cell-wall-deficient forms and helping them maintain their integrity in the absence of peptidoglycan. This second hypothesis is supported by a recent study by [Rojas et al., 2018](#), which established the outer membrane of *E. coli* as a major load-bearing element to counteract turgor pressure within the cytoplasm. Further promoting this hypothesis is the fact that UPEC mutants with defective LPS core synthesis — and therefore reduced stability of the outer membrane — have reduced survival to FOS exposure in SHU.

Overall, these results could lead to a model where heterogeneity in LPS synthesis provides an explanation as to why some cell-wall-deficient forms survive better to FOS treatment and are able to reinitiate growth upon FOS washout. This model could be easily validated by correlating UPEC survival at the single-cell level to the expression of transcriptional reporters of LPS synthesis using the microfluidic platform described in this work. Interestingly, this model could also inform the development of novel antibiotic regimens to curb the recurrence of UTIs. We could for example test the association of FOS with a recently developed compound targeting LPS synthesis ([Lemaître et al., 2017](#)). A potential synergistic effect with FOS might prove beneficial for patients at risk of developing recurrent UTI episodes.

## 4.3. Materials and methods

### 4.3.1. Plasmids and primers

Plasmids, primers and qRT-PCR primers used in this chapter are listed in **Tables 5.2, 5.3 and 5.5** respectively.

### 4.3.2. Bacterial culture conditions

CFT073 wild-type and mutant strains were inoculated from frozen glycerol stocks and cultured overnight for 16 h ( $\pm$  1 h) at 37°C with shaking at 170 rpm in either LB Luria medium (Sigma), synthetic human urine medium (see **4.3.3**), or pooled human female urine (Golden West Diagnostics). When required, media were supplemented with 100 µg/mL ampicillin (Sigma), 50 µg/mL kanamycin (Sigma) or 25 µg/mL chloramphenicol (Sigma) for selection. Antibiotic treatments were performed with fosfomycin (Sigma), nitrofurantoin (Sigma) or trimethoprim:sulfamethoxazole 1:5 (cotrimoxazole, Sigma).

### 4.3.3. Preparation of synthetic human urine (SHU) medium

Composite SHU was prepared following the protocol described by [Ipe et al., 2016](#). All compounds listed in **Table 4.3** were successively added to stirring double-distilled water, after which the pH was adjusted to 5.6, the volume was adjusted to 1L, and aliquots were filter-sterilized before storage at 4°C for up to 6 months.

Compound	Formula	Molar mass (g/mol)	Final conc. (mM)	Amount (g) for 1L SHU
Sodium chloride	NaCl	58.44	100	5.8440
Sodium sulfate	Na <sub>2</sub> SO <sub>4</sub>	142.04	17	2.4147
Urea	CH <sub>4</sub> N <sub>2</sub> O	60.06	280	16.8168
Potassium chloride	KCl	74.55	38	2.8329
Calcium chloride	CaCl <sub>2</sub>	110.98	4	0.4439
Creatinine	C <sub>4</sub> H <sub>7</sub> N <sub>3</sub> O	113.12	9	1.0181
Trisodium citrate	Na <sub>3</sub> C <sub>6</sub> H <sub>5</sub> O <sub>7</sub>	258.06	3.4	0.8774
Ammonium chloride	NH <sub>4</sub> Cl	53.49	20	1.0698
Magnesium sulfate	MgSO <sub>4</sub>	120.37	3.2	0.3852
Sodium oxalate	Na <sub>2</sub> C <sub>2</sub> O <sub>4</sub>	134	0.18	0.0241
Sodium phosphate monobasic	NaH <sub>2</sub> PO <sub>4</sub>	119.98	3.6	0.4319
Sodium phosphate dibasic	Na <sub>2</sub> HPO <sub>4</sub>	141.96	6.5	0.9227
Potassium phosphate monobasic	KH <sub>2</sub> PO <sub>4</sub>	136.09	16	2.1774
Uric acid	C <sub>5</sub> H <sub>4</sub> N <sub>4</sub> O <sub>3</sub>	168.11	0.6	0.1009
Sodium bicarbonate	NaHCO <sub>3</sub>	84.01	13.5	1.1341
Magnesium chloride hexahydrate	MgCl <sub>2</sub> · 6 H <sub>2</sub> O	203.30	3.2	0.6506
L-(+)-lactic acid	C <sub>3</sub> H <sub>6</sub> O <sub>3</sub>	90.08	1.1	0.0991
Iron (II) sulfate heptahydrate	FeSO <sub>4</sub> · 7 H <sub>2</sub> O	278.01	0.005	see below
Casamino acids	-	-	-	see below

Compound	Stock concentration	Final concentration	Amount (g) for 1L SHU
Iron (II) sulfate heptahydrate	13.90 g/L	0.001390 g/L	100 µL
Casamino acids	20%	0.1%	5 mL

**Table 4.3: Composition of Composite SHU medium** (adapted from [Ipe et al., 2016](#))

#### 4.3.4. Growth curve determination

Overnight cultures of CFT073 strains to be tested were diluted to  $OD_{600} = 0.005$  in corresponding pre-warmed medium and incubated at 37°C / 170 rpm for 8 hours with  $OD_{600}$  measurements taken every hour. Doubling times were calculated considering the exponential phase of growth.

#### 4.3.5. Minimum inhibitory concentration (MIC) determination

MICs were determined using the broth microdilution method, as described essentially by [Andrews, 2001](#). Briefly, overnight cultures of CFT073 strains to be tested were diluted to  $OD_{600} = 0.002$  in corresponding pre-warmed medium and grown at 37°C / 170 rpm to early exponential phase ( $OD_{600} > 0.01$ ).  $OD_{600}$  was then adjusted to 0.0005, corresponding to an inoculum size of approximately  $5.10^5$  CFU/mL, and suspensions were aliquoted in 4 rows of a 96-well plate, so as to have 4 technical replicates per strain. Antibiotics were added to the first column in a concentration corresponding to 20X the expected MIC and serial-diluted two-fold into the next columns. One column was left untreated, and one column was added with medium only, to provide 'no-drug' and 'no-cell' controls respectively. Well plates were incubated at 37°C / 170 rpm for 20 hours, after which  $OD_{600}$  was measured using a Tecan plate reader. MICs were calculated as described by [Lambert and Pearson, 2000](#). In the case of fosfomycin and LB, individual wells showing growth above the MIC (presumably due to the growth of resistant mutants at concentrations close to the MIC) were removed from the analysis if they occurred in only one out of four replicates.



#### 4.3.6. Fosfomycin (FOS) time-kill curve determination

Overnight cultures of CFT073 strains to be tested were diluted to  $OD_{600} = 0.002$  in corresponding pre-warmed medium and grown at 37°C / 170 rpm to early exponential phase ( $OD_{600} > 0.01$ ). FOS was added and bacterial survival was monitored by CFU plating at 0, 1, 2, 4 and 6 hours after FOS addition. More precisely, for **Figures 2.5B and 4.5**, aliquots were withdrawn at the indicated timepoints, centrifuged to remove the antibiotic and serial dilutions were spread on LB or LM agar plates. For **Figures 4.10, 4.11C and 4.13A**, aliquots were withdrawn at the indicated timepoints, directly serial-diluted and drops of the different dilutions were simply left to run on large LM agar plates. In all cases, LM was prepared as previously described ([Davison et al., 2020](#)) and CFUs were scored after overnight incubation at 37°C.

#### 4.3.7. Microfluidic device fabrication

The design of the microfluidic screening platform was done with AutoCAD (Autodesk), based on the previous design by [Verpoorte, 2017](#). The fabrication of the PDMS device required the production of two patterned silicon wafers to mold the flow and control layers of the device respectively. The production of these wafers in turn required the preparation of three photomasks: one for microchambers and one for flow channels of the flow layer, and one for control channels of the control layer. To circumvent PDMS shrinkage during curing steps, designs corresponding to the flow and control layers were scaled up by 100.5 % and 101.5 % respectively before writing on masks.

Masks and wafers were fabricated at the Center for MicroNanoTechnology (CMi) of EPFL using standard photolithography techniques. Briefly, AZ 1518-coated chrome masks (Nanofilm) were written with the different designs using a VPG200 laser writer (Heidelberg Instruments), and further processed with an HMR900 mask processor (Hamatech) for photoresist development, chrome etching and photoresist stripping. Masks were then used to pattern photoresist-coated silicon wafers on an MJB4 mask aligner (Süss Microtec), as detailed in **Table 4.4**. For the flow wafer, microchambers were first patterned using AZ nLof 2020 (MicroChemicals), and flow channels were then patterned on top using AZ 9260 (MicroChemicals). The choice of this second photoresist allowed the fabrication of structures with a round cross-section, which was necessary to ensure proper closing of the flow channels when actuating control valves (see **Figure 4.1C**). The control wafer was made of a single layer of SU8 GM1070 photoresist (Gersteltec), which allowed the patterning of 12  $\mu\text{m}$ -high control channels with a square cross-section. The height of the different structures was assessed with a DektakXT profilometer (Bruker).

Structure (photoresist)	Fabrication steps	Technical details		
Microchambers (AZ nLof 2020)  Height: 1.4 $\mu\text{m}$  Square cross-section	1. Wafer priming	HMDS	5 min	SSE oven
	2. Resist deposition + spin-coating	6,000 rpm	40 sec	SSE SB20 spin-coater
	3. Soft bake	110°C	1 min	SSE hot plate
	4. UV exposure	20 mW/cm <sup>2</sup>	3.5 sec	MJB4 mask aligner
	5. Post-exposure bake	110°C	1 min	SSE hot plate
	6. Development	MF CD26	20 sec	wet bench
	7. Hard bake	175°C	10 min	Ceram hot plate

Flow channels (AZ 9260)  Height: 12 $\mu\text{m}$  Rounded cross-section	1. Resist deposition + spin-coating	1,000 rpm	40 sec	SSE SB20 spin-coater
	2. Soft bake (reflow)	114°C	6 min	SSE hot plate
	3. Relaxation	25°C	20 h	black box
	4. UV exposure	20 mW/cm <sup>2</sup>	3 x 14 sec	MJB4 mask aligner
	5. Development	AZ400:H <sub>2</sub> O 1:3	10 min	wet bench
	6. Hard bake	175°C	10 min	Ceram hot plate

Control valves (SU8 GM1070)  Height: 12 $\mu\text{m}$  Square cross-section	1. Wafer cleaning	Plasma	7 min	Tepla 300
	2. Resist deposition + spin-coating	6,000 rpm	40 sec	LSM 250 spin-coater
	3. Relaxation	25°C	30 min	HP200 hot plate
	4. Soft bake	130°C	5 min	HP200 hot plate
	5. UV exposure	20 mW/cm <sup>2</sup>	10 sec	MJB4 mask aligner
	6. Post-exposure bake	90°C	40 min	HP200 hot plate
	7. Relaxation	25°C	20 h	black box
	8. Development	PGMEA	2 x 2 min	wet bench
	9. Hard bake	135°C	2 h	HP200 hot plate

**Table 4.4: Details of the flow (microchambers + flow channels) and control (valves) wafer fabrication steps**

Before first use, the flow and control wafers were treated with a vapor bath of trimethylchlorosilane (TMCS, Sigma) for 15 min to generate a hydrophobic surface. Sylgard 184 PDMS (Dow Corning) was prepared with two different elastomer to curing agent ratios: 5:1 for the control layer and 20:1 for the flow layer. Both mixtures were mixed and degassed using an ARE-250 mixer (Thinky). The 5:1 mixture was poured

on the control wafer and further degassed for 45 min in a vacuum desiccator. The 20:1 mixture was spin-coated on the flow wafer at 2,000 rpm for 35 sec with a LabSpin spin-coater (Süss Microtec) to obtain a thin PDMS film. Both layers were cured at 80°C for 32 min, after which devices were cut from the control wafer and holes for the valves were punched with a manual hole puncher (Schmidt Technology). Devices were manually aligned on the flow wafer using an M80 stereomicroscope (Leica) and cured at 80°C for 2 h to ensure strong bonding between the two layers. Devices were then peeled off the flow wafer, and holes for the flow inlets and outlets were punched.

#### 4.3.8. Coverslip fabrication

The fabrication of GPTES-coated glass coverslips was optimized from the protocol described by [Tang and Lee, 2010](#), using the iterative strategy presented in **Table 4.5**. The original protocol, which involves the chemical reaction between 3-glycidoxypropyltriethoxysilane (GPTES, Sigma) and 3-aminopropyltriethoxysilane (APTES, Sigma), was sequentially adjusted until reaching an acceptable compromise between too strong PDMS-to-glass bonding, which resulted in irreversible flow channel collapse when actuating control valves, and too weak bonding, which resulted in device leakage when perfusing it with culture medium. In the final protocol, PDMS was left untreated while glass coverslips (24 x 60 mm #1, Biosystems) were treated with a Zepto plasma cleaner (Diener Electronic) at 30 W for 1 min and coated with a 1% GPTES solution in water for 20 min before overnight relaxation for 20 h ( $\pm$  1 h).

**Table 4.5 (next page): Optimization of PDMS-to-glass bonding.** Successive modifications to the original protocol by [Tang and Lee, 2010](#) are indicated by red arrows.

Coverslip treatment	Timing	PDMS treatment	Timing	Extra treatment	Outcome
GPTES 1%	20 min	APTES 1%	20 min	-	Flow channel collapse
none	↓ -	APTES 1%	20 min	-	Flow channel collapse
none	-	APTES 1%	20 min	↓ Tape channels during APTES treatment	Flow channel collapse
none	-	APTES 1%	20 min	↓ Flow channels with medium early on	Flow channel collapse
none	-	APTES 1%	↓ 1 min	Flow channels with medium early on	Flow channel collapse
none	-	APTES 1%	1 min	↓ Wait overnight after APTES treatment	Device leakage
GPTES 1%	↓ 20 min	APTES 1%	1 min	Wait overnight after APTES treatment	Flow channel collapse
GPTES 1%	20 min	none	↓ -	-	Flow channel collapse
GPTES 1%	20 min	none	-	↓ Wait overnight after GPTES treatment	No collapse, no leakage

#### 4.3.9. Spotting of UPEC transposon mutants

Overnight UPEC cultures in 96-well plates were added with 0.5 M ectoine (Sigma), prior to spotting on a GPTES-coated coverslip using an XActII DNA microarrayer (LabNext) with Xtend pins (ø 0.14 mm, LabNext) and an ethanol pin washing time of

4 seconds. The humidity inside the arrayer was kept at 60% throughout the whole procedure to limit desiccation of bacterial spots. This resulted in an array of 1,152 spots of approximately 200  $\mu\text{m}$  in diameter, on top of which the microfluidic device was manually aligned using an SV6 stereomicroscope (Carl Zeiss). To ensure proper PDMS-to-glass bonding, the assembled device was then incubated for 20 min at 37°C before priming the microfluidic chip.

#### **4.3.10. Microfluidic chip priming and time-lapse movie acquisition**

The control layer was primed first by connecting control valves to water-filled Tygon® tubing (Cole-Parmer) using AISI 304 metal pins (Unimed). Water pressure was progressively increased from 200 to 1,200 mbar until proper closing of the underlying flow channels. The flow layer was then primed by injecting culture medium at 100 mbar through the medium inlets using a similar strategy. Medium outlets were initially left closed to purge air from the flow channels, and opened as soon as the chip was fully primed with medium. Eventually, the remaining inlets were connected with antibiotic-containing medium while controlling that the corresponding flow channels were properly closed to prevent untimely contact of UPEC with the antibiotic. The device was then kept at 37°C throughout the whole experiment.

UPEC mutants were first cultured in SHU for 6 h, then in SHU containing 100  $\mu\text{g/mL}$  FOS for 6 h, and then allowed to regrow in antibiotic-free SHU for another 14 h to assess bacterial survival. Medium switch was entirely performed by opening and closing control valves using an in-house-developed LabVIEW platform (National Instruments), and monitored by adding 0.5  $\mu\text{g/mL}$  sulforhodamine 101 (Thermo

Fisher) to the antibiotic-containing medium. Microchambers were imaged every 10 minutes using an automated epi-fluorescence microscope (Ti Eclipse, Nikon Instruments) equipped with a 60X air objective (NA = 0.95, #MRD30605) and a scientific CMOS camera (Prime BSI, Photometrics). Autofocus was performed with the hardware-based Perfect Focus System (PFS, Nikon instruments) and images were acquired on the phase-contrast, green (excitation 470/24 nm, emission 525/45 nm) and red (excitation 550/15 nm, emission 598/45 nm) fluorescence channels using a Spectra X light engine (Lumencor) combined with a Quad band filter set (Chroma).

#### **4.3.11. Screening for UPEC mutants with altered persistence: primary screen**

Time-lapse movie analysis was performed using a custom-made Fiji plugin to extract mean green and red fluorescence intensity values from microchambers over time. Red fluorescence traces were used to infer the timing of antibiotic treatment while green fluorescence traces were used to monitor the number of bacteria in each microchamber. Mutants that did not display a significant change in green fluorescence over the course of the experiment were considered poorly growing and removed from the analysis. For other mutants, the regrowth ratio in each microchamber was calculated by dividing the fluorescence value 11 h after FOS washout (chosen so that regrowth had started in most microchambers) by the fluorescence value 30 min before FOS addition, to normalize for the number of bacteria present before FOS treatment. For each mutant, the distribution of regrowth ratio values was then compared to the distribution for the  $\Delta fliC$  parental strain using Welch's t-test, and mutants with  $P < 0.05$  were selected for further analysis.

#### **4.3.12. Screening for UPEC mutants with altered persistence: rescreening**

Candidate mutants were rescreened using a simplified version of the time-kill curve protocol described in **Section 4.3.6**, where aliquots were withdrawn from the FOS-treated cultures at 0 and 6 h after FOS addition only. For each mutant, the fractional survival ratio (FSR) at 6 h was then calculated, corresponding to the normalized survival ratio after 6 h FOS treatment compared to the  $\Delta fliC$  parental strain, and mutants with a  $\geq 2$ -fold increased or decreased FSR were selected for further analysis.

#### **4.3.13. Identification of transposon insertion sites by RATE (rapid amplification of transposon ends)**

Tn5 insertion sites were identified as described in **Section 3.3.10**.

#### **4.3.14. Quantitative real-time PCR (qRT-PCR)**

qRT-PCR analyses were performed as described in **Section 3.3.13**.



## 5. Appendices

**Table 5.1: Genes that contribute positively or negatively to early adhesion of UPEC to bladder epithelial cells.** Genes corresponding to mutants with increased or decreased adhesion to bladder cells, along with their KEGG classification, KEGG definition, c accession number in the genome of CFT073, KO accession number in the KEGG database, and number of independent transposon “hits” in the screen. The individual chromosomal transposon insertion sites are also referenced. Genes that belong to the same operon are framed in black. Transposon insertions that occurred in intergenic regions are indicated in purple.

### (A) Genes corresponding to mutants with increased adhesion

Number	Gene	KEGG classification	Pathway	KEGG definition	c number	KO number	Gene size	Nb of hits	Mutant	Insertion site
1	<i>c2558</i>	9105 Metabolism 09107 Glycan biosynthesis and metabolism 00541 O-Antigen nucleotide sugar biosynthesis	glycan biosynthesis and metabolism	mannose-1-phosphate guanylyltransferase	c2558	<a href="#">K00971</a>	1452 bp	1	68F2	2,391,209
2	<i>c2560</i>	9105 Metabolism 09107 Glycan biosynthesis and metabolism 00541 O-Antigen nucleotide sugar biosynthesis	glycan biosynthesis and metabolism	UDP-glucose 4-epimerase	c2560	<a href="#">K01784</a>	1008 bp	2	66C9 63D3	2,393,895 2,394,112
3	<i>c2561</i>	9105 Metabolism 09107 Glycan biosynthesis and metabolism 00541 O-Antigen nucleotide sugar biosynthesis	glycan biosynthesis and metabolism	none	c2561	none	1146 bp	1	11E11	2,394,898
4	<i>c2562</i>	9105 Metabolism 09107 Glycan biosynthesis and metabolism 00541 O-Antigen nucleotide sugar biosynthesis	glycan biosynthesis and metabolism	none	c2562	none	1083 bp	4	20E7 64G8 46D4 6H1	2,396,073 2,396,086 2,396,248 2,396,608
5	<i>c2564</i>	9105 Metabolism 09107 Glycan biosynthesis and metabolism 00541 O-Antigen nucleotide sugar biosynthesis	glycan biosynthesis and metabolism	none	c2564	none	1362 bp	1	56C4	2,398,744
6	<i>waaV</i>	9104 Metabolism 09107 Glycan biosynthesis and metabolism 00540 Lipopolysaccharide biosynthesis	glycan biosynthesis and metabolism	UDP-glucose:(glucosyl)LPS beta-1,3-glucosyltransferase	c4449	<a href="#">K12983</a>	984 bp	3	71C4 46C6 62B6	4,231,676 4,231,937 4,232,036
7	<i>rfaI</i>	9103 Metabolism 09107 Glycan biosynthesis and metabolism 00540 Lipopolysaccharide biosynthesis	glycan biosynthesis and metabolism	UDP-glucose/galactose:(glucosyl)LPS alpha-1,2-glucosyl/galactosyltransferase	c4452	<a href="#">K03276</a>	996 bp	3	76A8 52D3 73C2	4,234,322 4,234,571 4,234,908
8	<i>rfaI</i>	9102 Metabolism 09107 Glycan biosynthesis and metabolism 00540 Lipopolysaccharide biosynthesis	glycan biosynthesis and metabolism	UDP-glucose:(glucosyl)LPS alpha-1,3-glucosyltransferase	c4453	<a href="#">K03275</a>	1017 bp	3	64G9 68H7 9B6	4,235,280 4,235,638 4,236,064
9	<i>rfaP</i>	9101 Metabolism 09107 Glycan biosynthesis and metabolism 00540 Lipopolysaccharide biosynthesis	glycan biosynthesis and metabolism	heptose 1 phosphotransferase	c4454	<a href="#">K02848</a>	807 bp	2	57D2 65D5	4,236,221 4,236,460
10	<i>rfaG</i>	9100 Metabolism 09107 Glycan biosynthesis and metabolism 00540 Lipopolysaccharide biosynthesis	glycan biosynthesis and metabolism	UDP-glucose:(heptosyl)LPS alpha-1,3-glucosyltransferase	c4455	<a href="#">K02844</a>	1125 bp	1	26D7	4,237,207
11	<i>rfe</i>	9105 Metabolism 09107 Glycan biosynthesis and metabolism 00542 O-Antigen repeat unit biosynthesis	glycan biosynthesis and metabolism	UDP-GlcNAc:undecaprenyl-phosphate/decaprenyl-phosphate GlcNAc-1-phosphate transferase	c4704	<a href="#">K02851</a>	1104 bp	1	63B5	4,469,099
12	<i>wecF</i>	9105 Metabolism 09107 Glycan biosynthesis and metabolism 01003 Glycosyltransferases	glycan biosynthesis and metabolism	enterobacterial common antigen polymerase	c4715	<a href="#">K02853</a>	1353 bp	1	70E4	4,479,691
13	<i>rfaH</i>	9105 Metabolism 09107 Glycan biosynthesis and metabolism 00540 Lipopolysaccharide biosynthesis	glycan biosynthesis and metabolism	transcriptional antiterminator RfaH	c4789	<a href="#">K05785</a>	489 bp	1	30F3	4,550,487
14	<i>kpsS</i>	09190 Not Included in Pathway 09193 Unclassified: signaling and cellular processes 99992 Structural proteins	capsule biosynthesis	capsular polysaccharide export protein	c3691	<a href="#">K07265</a>	1239 bp	1	46B7	3,519,449
15	<i>c3694</i>	09190 Not Included in Pathway 09193 Unclassified: signaling and cellular processes 99992 Structural proteins	capsule biosynthesis	CDP-glycerol glycerophosphotransferase	c3694	<a href="#">K09809</a>	3801 bp	4	30D6 69G6 16E6 57B9	3,523,189 3,523,932 3,524,799 3,524,991
16	<i>c3695</i>	09190 Not Included in Pathway 09193 Unclassified: signaling and cellular processes 99992 Structural proteins	capsule biosynthesis	none	c3695	none	1236 bp	2	63G7 61E1	3,526,586 3,527,388
17	<i>c3696</i>	09190 Not Included in Pathway 09193 Unclassified: signaling and cellular processes 99992 Structural proteins	capsule biosynthesis	glycerol-3-phosphate cytidyllyltransferase	c3696	<a href="#">K00980</a>	408 bp	3	65D7 15B1 54E2	3,527,542 3,527,666 3,527,793
18	<i>kpsM</i>	09190 Not Included in Pathway 09193 Unclassified: signaling and cellular processes 99992 Structural proteins	capsule biosynthesis	capsular polysaccharide transport system permease	c3698	<a href="#">K09688</a>	777 bp	2	72D8 65G7	3,528,681 3,528,850
	region between <i>kpsM</i> and <i>yghD</i>		capsule biosynthesis					2	21F6 51C4	3,529,501 3,529,923

19	<i>caiF</i>	09120 Genetic Information Processing 03000 Transcription factors	transcription factors	transcriptional activator CaiF	c0043	K08277	396 bp	1	40E12	37,383
	<i>caiE</i>	09190 Not Included in Pathway 09194 Poorly characterized 99996 General function prediction only		carnitine operon protein CaiE	c0044	K08279	612 bp			
20	<i>truB</i>	09120 Genetic Information Processing 03016 Transfer RNA biogenesis	transfer RNA biogenesis	tRNA pseudouridine55 synthase	c3922	K03177	945 bp	1	45C12	3,746,048
21	<i>pnp</i>	09120 Genetic Information Processing 09123 Folding, sorting and degradation 03018 RNA degradation	RNA degradation	polyribonucleotide nucleotidyltransferase	c3920	K00962	2223 bp	1	16F4	3,744,721
22	<i>c0322</i>	09130 Environmental Information Processing 09131 Membrane transport 02000 Transporters	membrane transport	oligogalacturonide transporter	c0322	K16210	1515 bp	1	69B7	292,839
23	<i>kefB</i>	09130 Environmental Information Processing 09131 Membrane transport 02000 Transporters	membrane transport	glutathione-regulated potassium-efflux system protein	c4125	K11747	1806 bp	1	64D6	3,911,910
24	<i>cadB</i>	09130 Environmental Information Processing 09131 Membrane transport 02000 Transporters	membrane transport	cadaverine:lysine antiporter	c5141	K03757	1335 bp	1	69E6	4,916,165
25	<i>citA</i>	09130 Environmental Information Processing 09132 Signal transduction 02020 Two-component system	signal transduction	two-component system, CitB family, cit operon sensor histidine kinase CitA	c0710	K07700	1719 bp	1	61F6	693,633
26	<i>sfaB</i>	09183 Signaling and cellular processes 02044 Secretion system	secretion system	putative F1C and S fimbrial switch regulatory protein	c1238	none	330 bp	1	7D7	1,187,761
27	<i>focA</i>	09183 Signaling and cellular processes 02044 Secretion system	secretion system	major type 1 subunit fimbria (pilin)	c1239	K07345	543 bp	1	46D7	1,188,691
28	<i>sfaD / focB</i>	09183 Signaling and cellular processes 02044 Secretion system	secretion system	fimbrial protein	c1240	K07351	525 bp	2	73G2 79B3	1,189,291 1,189,338
29	<i>focC</i>	09183 Signaling and cellular processes 02044 Secretion system	secretion system	fimbrial chaperone protein	c1241	K07346	696 bp	1	61B5	1,189,703
30	<i>focD</i>	09183 Signaling and cellular processes 02044 Secretion system	secretion system	outer membrane usher protein	c1242	K07347	2679 bp	1	78E5	1,192,492
31	<i>c2470</i>	none	other	putative peptide/polyketide synthase	c2470	none	5628 bp	1	48B8	2,313,329
32	<i>c4537</i>	none	other	none	c4537	none	2553 bp	1	47G8	4,315,978

## (B) Genes corresponding to mutants with decreased adhesion

Number	Gene	KEGG classification	Pathway	KEGG definition	c number	KO number	Gene size	Nb of hits	Mutant	Insertion site
1	<i>acnB</i>	09100 Metabolism 09101 Carbohydrate metabolism 00020 Citrate cycle (TCA cycle)	carbohydrate metabolism	aconitate hydratase 2 / 2-methylisocitrate dehydratase	c0147	K01682	2598 bp	1	36H5	143,872
2	<i>tdcE</i>	09100 Metabolism 09101 Carbohydrate metabolism 00620 Pyruvate metabolism	carbohydrate metabolism	formate C-acetyltransferase	c3872	K00656	2295 bp	1	26C8	3,701,763
3	<i>cydA</i>	09100 Metabolism 09102 Energy metabolism 00190 Oxidative phosphorylation	energy metabolism	cytochrome bd ubiquinol oxidase subunit I	c0811	K00425	1572 bp	2	22E3 84F1	795,156 795,413
4	<i>cydB</i>	09100 Metabolism 09102 Energy metabolism 00190 Oxidative phosphorylation	energy metabolism	cytochrome bd ubiquinol oxidase subunit II	c0812	K00426	1140 bp	1	27F8	796,419
5	<i>atpD</i>	09100 Metabolism 09102 Energy metabolism 00190 Oxidative phosphorylation	energy metabolism	F-type H <sup>+</sup> /Na <sup>+</sup> -transporting ATPase subunit beta	c4658	K02112	1383 bp	1	11H1	4,418,337
6	<i>atpG</i>	09100 Metabolism 09102 Energy metabolism 00190 Oxidative phosphorylation	energy metabolism	F-type H <sup>+</sup> /Na <sup>+</sup> -transporting ATPase subunit gamma	c4659	K02115	864 bp	2	26H5 27A1	4,419,075 4,419,107
7	<i>atpA</i>	09100 Metabolism 09102 Energy metabolism 00190 Oxidative phosphorylation	energy metabolism	F-type H <sup>+</sup> /Na <sup>+</sup> -transporting ATPase subunit alpha	c4660	K02111	1542 bp	4	23E5 19H5 57B11 63A4	4,419,425 4,419,795 4,419,806 4,420,436
8	<i>atpB</i>	09100 Metabolism 09102 Energy metabolism 00190 Oxidative phosphorylation	energy metabolism	F-type H <sup>+</sup> /Na <sup>+</sup> -transporting ATPase subunit A	c4666	K02108	816 bp	2	72B2 63D10	4,422,667 4,422,897
9	<i>cmk</i>	09100 Metabolism 09104 Nucleotide metabolism 00240 Pyrimidine metabolism	nucleotide metabolism	CMP/dCMP kinase	c1048	K00945	684 bp	1	50H3	1,012,636
10	<i>purB</i>	09100 Metabolism 09104 Nucleotide metabolism 00230 Purine metabolism	nucleotide metabolism	adenylosuccinate lyase	c1510	K01756	1371 bp	1	24D3	1,392,015
11	<i>pyrB</i>	09100 Metabolism 09104 Nucleotide metabolism 00240 Pyrimidine metabolism	nucleotide metabolism	aspartate carbamoyltransferase catalytic subunit	c5345	K00609	936 bp	1	45G11	5,089,008
12	<i>dapA</i>	09100 Metabolism 09105 Amino acid metabolism 00300 Lysine biosynthesis	amino acid metabolism	4-hydroxy-tetrahydrodipicolinate synthase	c3006	K01714	897 bp	1	569	2,870,535
(most likely in the promoter of <i>dapA</i> )	<i>gcvR</i>	09120 Genetic Information Processing 03000 Transcription factors		glycine cleavage system transcriptional repressor	c3007	K03567	573 bp			
13	<i>lpxC</i>	09100 Metabolism 09107 Glycan biosynthesis and metabolism 00540 Lipopolysaccharide biosynthesis	glycan biosynthesis and metabolism	UDP-3-O-[3-hydroxymyristoyl] N-acetylglucosamine deacetylase	c0114	K02535	918 bp	1	63B11	111,242
14	<i>c3800</i>	09100 Metabolism 09107 Glycan biosynthesis and metabolism 00540 Lipopolysaccharide biosynthesis	glycan biosynthesis and metabolism	D-beta-D-heptose 7-phosphate kinase / D-beta-D-heptose 1-phosphate adenylyltransferase	c3800	K03272	1434 bp	1	11B3	3,634,904
15	<i>waaW</i>	09100 Metabolism 09107 Glycan biosynthesis and metabolism 00540 Lipopolysaccharide biosynthesis	glycan biosynthesis and metabolism	(galactosyl)LPS 1,2-glucosyltransferase	c4450	K12985	1029 bp	1	88E6	4,233,066
16	<i>yaeL</i>	09100 Metabolism 01002 Peptidases and inhibitors	peptidases and inhibitors	regulator of sigma E protease	c0213	K11749	1398 bp	1	12A11	207,927
17	<i>lon</i>	09100 Metabolism 01002 Peptidases and inhibitors	peptidases and inhibitors	ATP-dependent Lon protease	c0555	K01338	2400 bp	1	64D9	535,074
18	<i>aksA</i>	09120 Genetic Information Processing 03000 Transcription factors	transcription factors	DnaK suppressor protein	c0178	K06204	456 bp	1	3D5	170,772
19	<i>lrp</i>	09120 Genetic Information Processing 03000 Transcription factors	transcription factors	Lrp/AsnC family transcriptional regulator, leucine-responsive regulatory protein	c1026	K03719	495 bp	1	86E12	986,958

20	<i>crp</i>	09120 Genetic Information Processing 03000 Transcription factors	transcription factors	CRP/FNR family transcriptional regulator, cyclic AMP receptor protein	c4132	K10914	633 bp	1	23A10	3,917,627
21	<i>yhhG</i>	09120 Genetic Information Processing 03000 Transcription factors	transcription factors	CopG family transcriptional regulator, nickel-responsive regulator	c4274	K07722	402 bp	1	4D2	4,057,448
22	<i>rnc</i>	09120 Genetic Information Processing 03019 Messenger RNA biogenesis	messenger RNA biogenesis	ribonuclease III	c3091	K03685	681 bp	1	8F9	2,966,959
(most likely in the promoter of <i>rnc</i> )	<i>lepB</i>	09120 Genetic Information Processing 09123 Folding, sorting and degradation 03060 Protein export		signal peptidase I	c3092	K03100	975 bp			
	<i>tgt</i>	09120 Genetic Information Processing 03016 Transfer RNA biogenesis	transfer RNA biogenesis	queuine tRNA-ribosyltransferase	c0516	K00773	1128 bp	1	58D1	501,414
	<i>mnmA</i>	09120 Genetic Information Processing 03016 Transfer RNA biogenesis	transfer RNA biogenesis	tRNA-uridine 2-sulfurtransferase	c1512	K00566	1107 bp	1	24B2	1,394,309
	<i>rmt</i>	09120 Genetic Information Processing 03016 Transfer RNA biogenesis	transfer RNA biogenesis	ribonuclease T	c2045	K03683	648 bp	2	82G1 13E10	1,889,301 1,889,395
26	<i>yheN</i>	09120 Genetic Information Processing 03016 Transfer RNA biogenesis	transfer RNA biogenesis	tRNA 2-thiouridine synthesizing protein D	c4119	K07235	387 bp	1	23B12	3,906,726
27	<i>gidA</i>	09120 Genetic Information Processing 03016 Transfer RNA biogenesis	transfer RNA biogenesis	tRNA 5-cmmn uridine modification enzyme	c4669	K03495	1890 bp	3	56H3 71F5 75A1	4,425,011 4,425,480 4,426,235
28	<i>glxX</i>	09120 Genetic Information Processing 09122 Translation 00970 Aminoacyl-tRNA biosynthesis	translation	glutamyl-tRNA synthetase	c2936	K01885	1416 bp	1	15H8	2,800,289
29	<i>selB</i>	09120 Genetic Information Processing 03012 Translation factors	translation factors	selenocysteine-specific elongation factor	c4411	K03833	1845 bp	1	26D1	4,193,829
30	<i>dsbA</i>	09120 Genetic Information Processing 03110 Chaperones and folding catalysts	chaperones and folding catalysts	protein dithiol oxidoreductase (disulfide-forming)	c4804	K03673	627 bp	4	33G3 87G9 17E10 27H7	4,569,080 4,569,398 4,569,459
31	<i>hslU</i>	09120 Genetic Information Processing 03110 Chaperones and folding catalysts	chaperones and folding catalysts	ATP-dependent HslUV protease ATP-binding subunit HslU	c4884	K03667	1332 bp	1	5A3	4,640,252
32	<i>dam</i>	09120 Genetic Information Processing 09124 Replication and repair 03430 Mismatch repair	replication and repair	DNA adenine methylase	c4157	K06223	837 bp	2	59F10 16F2	3,941,210 3,941,470
33	<i>rep</i>	09120 Genetic Information Processing 09124 Replication and repair 03400 DNA repair and recombination	replication and repair	ATP-dependent DNA helicase	c4698	K03656	2022 bp	1	36A9	4,460,898
34	<i>acrA</i>	09130 Environmental Information Processing 09131 Membrane transport 02000 Transporters	membrane transport	membrane fusion protein, multidrug efflux system	c0581	K03585	1230 bp	1	11E9	559,519
35	<i>tolB</i>	09130 Environmental Information Processing 09131 Membrane transport 02010 ABC transporters	membrane transport	TolB protein	c0819	K03641	1296 bp	2	22D8 3G10	800,456 801,010
36	<i>cydD</i>	09130 Environmental Information Processing 09131 Membrane transport 02010 ABC transporters	membrane transport	ATP-binding cassette, subfamily C, bacterial CydD	c1024	K16013	1767 bp	1	50G10	984,009
37	<i>mppA</i>	09130 Environmental Information Processing 09131 Membrane transport 02010 ABC transporters	membrane transport	oligopeptide transport system substrate-binding protein	c1803	K15580	1635 bp	1	48C4	1,637,826
38	<i>yddA</i>	09130 Environmental Information Processing 09131 Membrane transport 02010 ABC transporters	membrane transport	vitamin B12/bleomycin/antimicrobial peptide transport system ATP-binding/permease protein	c1925	K02471	1686 bp	1	65F3	1,763,863
39	<i>yeiO</i>	09130 Environmental Information Processing 09131 Membrane transport 02000 Transporters	membrane transport	MFS transporter, SET family, sugar efflux transporter	c2706	K03291	1182 bp	1	3B1	2,554,501
40	<i>c3774</i>	09130 Environmental Information Processing 09131 Membrane transport 02000 Transporters	membrane transport	iron complex transport system ATP-binding protein	c3774	K02013	810 bp	1	86H5	3,607,124
41	<i>yheF</i>	09130 Environmental Information Processing 09131 Membrane transport 03070 Bacterial secretion system	membrane transport	general secretion pathway protein D	c4096	K02453	1965 bp	1	80B12	3,888,658
42	<i>xylF</i>	09130 Environmental Information Processing 09131 Membrane transport 02010 ABC transporters	membrane transport	D-xylose transport system substrate-binding protein	c4386	K10543	1071 bp	1	50D6	4,169,252
43	<i>pstB</i>	09130 Environmental Information Processing 09131 Membrane transport 02010 ABC transporters	membrane transport	phosphate transport system ATP-binding protein	c4649	K02036	774 bp	1	53A5	4,409,481
44	<i>pstS</i>	09130 Environmental Information Processing 09131 Membrane transport 02010 ABC transporters	membrane transport	phosphate transport system substrate-binding protein	c4653	K02040	1041 bp	1	60D1	4,411,908
45	<i>trkD</i>	09130 Environmental Information Processing 09131 Membrane transport 02000 Transporters	membrane transport	KUP system potassium uptake protein	c4675	K03549	1869 bp	1	2H9	4,432,923
46	<i>rbxB</i>	09130 Environmental Information Processing 09131 Membrane transport 02010 ABC transporters	membrane transport	ribose transport system substrate-binding protein	c4679	K10439	897 bp	1	2G12	4,438,165
47	<i>papG</i>	09183 Signaling and cellular processes 02044 Secretion system	secretion system	adhesin PapG	c3583	K12522	1011 bp	2	36E5 56A10	3,429,660 3,430,433
48	<i>papF</i>	09183 Signaling and cellular processes 02044 Secretion system	secretion system	minor pilin subunit PapF	c3584	K12521	531 bp	2	88C12 32B8	3,430,758 3,430,972
49	<i>papE</i>	09183 Signaling and cellular processes 02044 Secretion system	secretion system	minor pilin subunit PapE	c3585	K12520	540 bp	2	25C10 62H7	3,431,408 3,431,422
50	<i>papD</i>	09183 Signaling and cellular processes 02044 Secretion system	secretion system	chaperone protein PapD	c3589	K12519	606 bp	1	33H2	3,433,424
51	<i>papC</i>	09183 Signaling and cellular processes 02044 Secretion system	secretion system	outer membrane usher protein PapC	c3590	K12518	2523 bp	1	59A10	3,435,852
52	<i>papF_2</i>	09183 Signaling and cellular processes 02044 Secretion system	secretion system	minor pilin subunit PapF	c5180	K12521	531 bp	1	12B1	4,942,170
53	<i>yadL</i>	09183 Signaling and cellular processes 02044 Secretion system	secretion system	hypothetical protein yadL precursor	c0168	none	615 bp	1	37H5	162,314
54	<i>c0417</i>	none	other	2,5-diketo-D-gluconic acid reductase A	c0417	none	885 bp	1	69D1	401,760
55	<i>yqC</i>	09190 Not Included in Pathway 09194 Poorly characterized 99996 General function prediction only	other	high frequency lysogenization protein	c1511	K07153	648 bp	1	62E11	1,393,451
56	<i>yciE</i>	none	other	none	c1723	none	507 bp	1	64B6	1,559,124
57	<i>ydcA</i>	none	other	none	c1845	none	174 bp	1	81A11	1,685,888
58	<i>c2406</i>	none	other	none	c2406	none	963 bp	1	33A2	2,209,870
	<i>c2407</i>	none	other	none	c2407	none	153 bp			
59	<i>yehL</i>	none	other	none	c2649	none	1155 bp	1	30G12	2,496,111
(most likely in the promoter region)										
	<i>c5021</i>	none	other	putative oxidoreductase	c5021	none	2166 bp	1	32F9	4,795,295

**Table 5.2: Plasmids used in this work**

Plasmid name	Description	Reference
pCP20	temperature-sensitive expression of FLP recombinase	<a href="#">Datsenko and Wanner, 2000</a>
pKD4	<i>kan<sup>R</sup></i> template for gene deletion	<a href="#">Datsenko and Wanner, 2000</a>
pKD46	$\lambda$ Red recombinase expression under control of P <sub>BAD</sub>	<a href="#">Datsenko and Wanner, 2000</a>
pRSET-AT3.10	sequence of AT3.10 ATeam biosensor	<a href="#">Imamura et al., 2009</a>
pRSET-AT3.10 <sup>MGK</sup>	sequence of AT3.10 <sup>MGK</sup> ATeam biosensor	<a href="#">Imamura et al., 2009</a>
pRSET-AT1.03 <sup>YEMK</sup>	sequence of AT1.03 <sup>YEMK</sup> ATeam biosensor	<a href="#">Imamura et al., 2009</a>
pRSET-AT1.03	sequence of AT1.03 ATeam biosensor	<a href="#">Imamura et al., 2009</a>
pRSET-AT1.03 <sup>KK</sup>	sequence of AT1.03 <sup>KK</sup> ATeam biosensor	<a href="#">Imamura et al., 2009</a>
pSLC217	RelE toxin expression under control of P <sub>RhaB</sub>	<a href="#">Khetrapal et al., 2015</a>
pSLC293	template for sfGFP expression under control of P <sub><math>\sigma</math>70</sub>	<a href="#">Eshaghi et al., 2016</a>
pZA32-AT3.10	constitutive expression of AT3.10 ATeam biosensor	This study
pZA32-AT3.10 <sup>MGK</sup>	constitutive expression of AT3.10 <sup>MGK</sup> ATeam biosensor	This study
pZA32-AT1.03 <sup>YEMK</sup>	constitutive expression of AT1.03 <sup>YEMK</sup> ATeam biosensor	This study
pZA32-AT1.03	constitutive expression of AT1.03 ATeam biosensor	This study
pZA32-AT1.03 <sup>KK</sup>	constitutive expression of AT1.03 <sup>KK</sup> ATeam biosensor	This study
pZA32-YFP	constitutive YFP expression	Lab stocks

**Table 5.3: Primers used in this work**

Primer name	Nucleotide sequence (5' to 3')	Reference
attHK_F	GCTGATAAAGCGCAGGTTG	This study
attHK_R	GCGCAACAGGTTATCAGC	This study
AT_F	CGGCATGCGTGATCCGAGCTCGAGTAT	This study
AT_R	GCCATAGATTGCAGCCGGATCAAGCTT	This study
fimB_KO_F	GCACAGCTAGTGCGCGTCTGTAATTATAAGGGAAAACGATGAAGT GTGTAGGCTGGAGCTGCTTCG	This study
fimB_F	GAAGAACTGGTCCACTTACGTTAG	This study
fimH_KO_F	GATTAGCATCACCTATACCTACAGCTGAACCCAAAGAGATGATTTG TGTAGGCTGGAGCTGCTTCG	This study
fimH_KO_R	GTAATATTGCGTACCTGCATTAGCAATGCCCTGTGATTTCTTTATTG CATATGAATATCCTCCTTAG	This study
fimH_F	GATGATTCTCACAATCAGCG	This study
fimH_R	GAACAGACCAGCAAAGTGC	This study
fliC_KO_F	TAATCAACGACTTGCAATATAGGATAACGAATCATGGCACAATGTG TAGGCTGGAGCTGCTTCG	This study
fliC_KO_R	TGCCGTCAGTCTCAGTTAATCAGGTTACGGCGATTAACCCTGCATA TGAATATCCTCCTTAG	This study
fliC_F	CAGACGATAACAGGGTTGACGGC	This study
fliC_R	TTGCAATTCCCCTTGTAGGCCTG	This study
focA_KO_F	GTGCGTAGTTCAATTAACCAAGGAATTAATATGAAGTTAAATGT GTAGGCTGGAGCTGCTTCG	This study
focA_F	TCATAAATGCTGCCTGAGTG	This study
focH_KO_R	AAGAGCAGTAATATCATTACCGCCACAACCTGCATTCTAGTTGTAGC TCATATGAATATCCTCCTTAG	This study
focH_R	TATGACAGACTCGTTCCGTC	This study
GenIsland_F	GCGCAGACTACGCAATGACA	This study
GenIsland_R	TGCTGAATGCGCTCACTTTTG	This study
P4	GCGCCATCAGGGCAAAGCCCATCCAGAGTCTTCGGGTCAGGGTTA AATTCACGGTCGGTGCGTGTAGGCTGGAGCTGCTTC	<a href="#">Eshaghi et al., 2016</a>
P5	ATAATAAGGCTTTATGCTAGATGCATTCTGCTTTGCGACTCAACCTT TTTCACCTAAAGTCATATGAATATCCTCCTTAG	<a href="#">Eshaghi et al., 2016</a>
P6	GCGCCATCAGGGCAAAGCCCATCCAGAGTCTTCGGGTCAGGGTTA AATTCACGGTCGGTGCTTGACGGCTAGCTCAGTCCTA	<a href="#">Eshaghi et al., 2016</a>
P7	ATAATAAGGCTTTATGCTAGATGCATTCTGCTTTGCGACTCAACCTT TTTCACCTAAAGTTTAATGATGATGATGATGATG	<a href="#">Eshaghi et al., 2016</a>
papA_KO_F	ATCGGGTCATTTTAAATTGCCAGATATCTCTGGTGTGTTCAAGTATGT GTAGGCTGGAGCTGCTTCG	This study
papA_F	TAAAAAAGCTGCTGGCGGTG	This study
papA2_F	GGGGCAGCTAAAAAAGGTAC	This study
papG_KO_R	ATCCACAACACTCTATCCGGCTCCGGATAAACCATTTATGGCAATA TCATATGAATATCCTCCTTAG	This study
papG_R	AATCGCGGATCATTACACAG	This study

papG2_R	ACATGGACGTAACCTCAGTGC	This study
papI_F	GCCATGCAGTAAATCCAGAC	This study
papI2_F	GCGCCGGTTCAGTAAATTAG	This study
R6K_inv1	ATGGCTCATAACACCCCTTGATTA	<a href="#">Ducey et al., 2002</a>
R6K_FP1	ACCTACAACAAAGCTCTCATCAACC	<a href="#">Ducey et al., 2002</a>
R6K_RP1	CTACCCTGTGGAACACCTACATCT	<a href="#">Ducey et al., 2002</a>

**Table 5.4: Primer pairs used for assignment of P pili transposon insertions to the *pap1* or *pap2* operon**

Insertion	First primer	Second primer	Expected size	Extension time	Extension temperature
<i>papC</i>	R6K_FP1	papA_F or papA2_F	1.4 kbp	40 sec	66°C
<i>papD</i>	R6K_RP1	papA_F or papA2_F	3.8 kbp	105 sec	66°C
<i>papE</i> #1	R6K_FP1	papG_R or papG2_R	1.9 kbp	50 sec	66°C
<i>papE</i> #2	R6K_RP1	papG_R or papG2_R	1.9 kbp	50 sec	66°C
<i>papF</i> #1	R6K_RP1	papG_R or papG2_R	1.5 kbp	40 sec	66°C
<i>papF</i> #2	R6K_FP1	papG_R or papG2_R	1.3 kbp	40 sec	66°C
<i>papG</i> #1	R6K_FP1	papG_R or papG2_R	900 bp	25 sec	66°C
<i>papG</i> #2	R6K_RP1	papG_R or papG2_R	200 bp	15 sec	66°C
<i>papF_2</i>	R6K_RP1	papG_R or papG2_R	1.4 kbp	40 sec	66°C

**Table 5.5: qRT-PCR primers used in this work**

<b>Primer name</b>	<b>Nucleotide sequence (5' to 3')</b>	<b>Reference</b>
q_fimA_F	GGCAATCGTTGTTCTGTCCG	This study
q_fimA_R	AACGGTCCCACCATTAACCG	This study
q_gapA_F	CATCGTTTCCAACGCATCCT	<a href="#">Snyder et al., 2004</a>
q_gapA_R	ACCTTCGATGATGCCGAAGTT	<a href="#">Snyder et al., 2004</a>
q_lptD_F	GGAGAGGTAGCGGAATTCGTT	This study
q_lptD_R	TCACGCCGCATTATATGCA	This study
q_lpxA_F	GCCGTTCCGGTGTCATATCG	This study
q_lpxA_R	AATCGCCTCACGGCTGAA	This study
q_lpxB_F	GTGCCGCTGGTGAATGC	This study
q_lpxB_R	GGCGCGACTGCAGCTTT	This study
q_msbA_F	CGCTGAAATCGCTGACCAA	This study
q_msbA_R	CGTCTGACAAGCCGCCATA	This study
q_murA_F	TAGTGCGGCAAAAAGGATAGG	This study
q_murA_R	AGCTCCAGGGCGAAGTCA	This study
q_murG_F	GCATCAGAGCGGCAAAGGT	This study
q_murG_R	TTGTCCCGCTTCGGCATA	This study
q_papA_F	TTTTCGGGTGTCCTCAAGTG	This study
q_papA_R	GTTTTCCATGTGGATCGGTG	This study
q_papA2_F	GTGCCTGCAGAAAATGCAGAT	<a href="#">Snyder et al., 2004</a>
q_papA2_R	CCCGTTTTCCACTCGAATCA	<a href="#">Snyder et al., 2004</a>

## 6. References

- Agata, N. *et al.* Serological response to P-fimbriae of *Escherichia coli* in patients with urinary tract infections. *Eur J Clin Microbiol Infect Dis* **8**(2), 156–159 (1989).
- Anderson, G. G. *et al.* Intracellular Bacterial Biofilm-Like Pods in Urinary Tract Infections. *Science* **301**, 105–107 (2003).
- Andersson, H. & van den Berg, A. Microfluidic devices for cellomics: a review. *Sensors and Actuators B: Chemical* **92**, 315–325 (2003).
- Andrews, J. M. Determination of minimum inhibitory concentrations. *J Antimicrob Chemother* **48**, 5–16 (2001).
- Balaban, N. Q., Gerdes, K., Lewis, K. & McKinney, J. D. A problem of persistence: still more questions than answers? *Nat Rev Microbiol* **11**, 587–591 (2013).
- Balaban, N. Q., Merrin, J., Chait, R., Kowalik, L. & Leibler, S. Bacterial persistence as a phenotypic switch. *Science* **305**, 1622–1625 (2004).
- Balaban, N. Q. *et al.* Definitions and guidelines for research on antibiotic persistence. *Nat Rev Microbiol* **17**, 441–448 (2019).
- Barber, A. E., Norton, J. P., Wiles, T. J. & Mulvey, M. A. Strengths and Limitations of Model Systems for the Study of Urinary Tract Infections and Related Pathologies. *Microbiol. Mol. Biol. Rev.* **80**, 351–367 (2016).
- Bates, J. M. *et al.* Tamm-Horsfall protein knockout mice are more prone to urinary tract infection. *Kidney International* **65**, 791–797 (2004).
- Bien, J., Sokolova, O. & Bozko, P. Role of Uropathogenic *Escherichia coli* Virulence Factors in Development of Urinary Tract Infection and Kidney Damage. *International Journal of Nephrology* **2012**, 1–15 (2012).
- Bigger, Joseph W. TREATMENT OF STAPHYLOCOCCAL INFECTIONS WITH PENICILLIN BY INTERMITTENT STERILISATION. *The Lancet* **244**, 497–500 (1944).



Blango, M. G. & Mulvey, M. A. Persistence of Uropathogenic *Escherichia coli* in the Face of Multiple Antibiotics. *Antimicrob Agents Chemother* **54**, 1855–1863 (2010).

Boutros, M., Heigwer, F. & Laufer, C. Microscopy-Based High-Content Screening. *Cell* **163**, 1314–1325 (2015).

Cleary, J. *et al.* Enteropathogenic *Escherichia coli* (EPEC) adhesion to intestinal epithelial cells: role of bundle-forming pili (BFP), EspA filaments and intimin. *Microbiology* **150**, 527–538 (2004).

Conlon, B. P. *et al.* Persister formation in *Staphylococcus aureus* is associated with ATP depletion. *Nat Microbiol* **1**, 16051 (2016).

Conover, M. S. *et al.* Inflammation-Induced Adhesin-Receptor Interaction Provides a Fitness Advantage to Uropathogenic *E. coli* during Chronic Infection. *Cell Host & Microbe* **20**, 482–492 (2016).

Cox, J. *et al.* Accurate proteome-wide label-free quantification by delayed normalization and maximal peptide ratio extraction, termed MaxLFQ. *Mol Cell Proteomics*. **13(9)**, 2513–26 (2014).

Cox, J. & Mann, M. MaxQuant enables high peptide identification rates, individualized p.p.b.-range mass accuracies and proteome-wide protein quantification. *Nat Biotechnol* **26**, 1367–1372 (2008).

Crépin, S. *et al.* Decreased Expression of Type 1 Fimbriae by a *pst* Mutant of Uropathogenic *Escherichia coli* Reduces Urinary Tract Infection. *Infect. Immun.* **80**, 2802–2815 (2012).

Darling, A. C. E., Mau, B., Blattner, F. R. & Perna, N. T. Mauve: Multiple Alignment of Conserved Genomic Sequence With Rearrangements. *Genome Res.* **14**, 1394–1403 (2004).

Datsenko, K. A. & Wanner, B. L. One-step inactivation of chromosomal genes in *Escherichia coli* K-12 using PCR products. *Proceedings of the National Academy of Sciences* **97**, 6640–6645 (2000).

- Davison, F., Chapman, J. & Mickiewicz, K. Isolation of L-form Bacteria from Urine using Filtration Method. 11 (2020).
- Dénervaud, N. *et al.* A chemostat array enables the spatio-temporal analysis of the yeast proteome. *Proceedings of the National Academy of Sciences* **110**, 15842–15847 (2013).
- de Ree, J. M. & van den Bosch, J. F. Serological response to the P fimbriae of uropathogenic *Escherichia coli* in pyelonephritis. *Infect Immun* **55**, 2204–2207 (1987).
- Dhar, N. & McKinney, J. D. Microbial phenotypic heterogeneity and antibiotic tolerance. *Current Opinion in Microbiology* **10**, 30–38 (2007).
- Dodson, K. W. *et al.* Structural Basis of the Interaction of the Pyelonephritic *E. coli* Adhesin to Its Human Kidney Receptor. *Cell* **105**, 733–743 (2001).
- Dörr, T., Vulić, M. & Lewis, K. Ciprofloxacin Causes Persister Formation by Inducing the TisB toxin in *Escherichia coli*. *PLoS Biol* **8**, e1000317 (2010).
- Ducey, T. F. & Dyer, D. W. Rapid identification of EZ::TN transposon insertion sites in the genome of *Neisseria gonorrhoeae*. *Epicentre Forum* **9**, 6-7 (2002).
- Duraiswamy, S. *et al.* Purification of Intracellular Bacterial Communities during Experimental Urinary Tract Infection Reveals an Abundant and Viable Bacterial Reservoir. *Infection and Immunity* **86**, 15 (2018).
- Egan, A. J. F., Errington, J. & Vollmer, W. Regulation of peptidoglycan synthesis and remodelling. *Nat Rev Microbiol* **18**, 446–460 (2020).
- Ejrnaes, K. *et al.* Pulsed-Field Gel Electrophoresis Typing of *Escherichia coli* Strains from Samples Collected before and after Pivmecillinam or Placebo Treatment of Uncomplicated Community-Acquired Urinary Tract Infection in Women. *J Clin Microbiol* **44**, 1776–1781 (2006).
- Eshaghi, M., Mehershahi, K. S. & Chen, S. L. Brighter Fluorescent Derivatives of UTI89 Utilizing a Monomeric vGFP. *Pathogens* **5**, (2016).

Fisher, R. A., Gollan, B. & Helaine, S. Persistent bacterial infections and persister cells. *Nat Rev Microbiol* **15**, 453–464 (2017).

Flores-Mireles, A. L., Walker, J. N., Caparon, M. & Hultgren, S. J. Urinary tract infections: epidemiology, mechanisms of infection and treatment options. *Nat Rev Microbiol* **13**, 269–284 (2015).

Foxman, B. Epidemiology of urinary tract infections: incidence, morbidity, and economic costs. *The American Journal of Medicine* **113**, 5–13 (2002).

Foxman, B. The epidemiology of urinary tract infection. *Nat Rev Urol* **7**, 653–660 (2010).

Foxman, B. Urinary Tract Infection Syndromes. *Infectious Disease Clinics of North America* **28**, 1–13 (2014).

Foxman, B., Barlow, R., D'Arcy, H., Gillespie, B. & Sobel, J. D. Urinary Tract Infection: Self-Reported Incidence and Associated Costs. **10**, 7 (2000).

Franssila S., Introduction to Microfabrication, 2nd ed., John Wiley & Sons Ltd (2010)

Fridman, O., Goldberg, A., Ronin, I., Shores, N. & Balaban, N. Q. Optimization of lag time underlies antibiotic tolerance in evolved bacterial populations. *Nature* **513**, 418–421 (2014).

García Méndez, K. B., Bragagnolo, G., O'Callaghan, D., Lavigne, J.-P. & Kerié, A. A high-throughput assay for the measurement of uropathogenic *Escherichia coli* attachment to urinary bladder cells. *Int. J. Exp. Path.* **97**, 194–201 (2016).

Gardiner, B. J., Stewardson, A. J., Abbott, I. J. & Peleg, A. Y. Nitrofurantoin and fosfomycin for resistant urinary tract infections: old drugs for emerging problems. *Aust Prescr* **42**, 14 (2019).

Gerdes, K. & Maisonneuve, E. Bacterial Persistence and Toxin-Antitoxin Loci. *Annu. Rev. Microbiol.* **66**, 103–123 (2012).

Goormaghtigh, F. *et al.* Reassessing the Role of Type II Toxin-Antitoxin Systems in Formation of *Escherichia coli* Type II Persister Cells. *mBio* **9**, e00640-18 (2018).

- Goormaghtigh, F. & Van Melderren, L. Single-cell imaging and characterization of *E. coli* persister cells to ofloxacin in exponential cultures. *Sci. Adv.* **5**, eaav9462 (2019).
- Greene, S. E., Hibbing, M. E., Janetka, J., Chen, S. L. & Hultgren, S. J. Human Urine Decreases Function and Expression of Type 1 Pili in Uropathogenic *Escherichia coli*. *mBio* **6**, (2015).
- Gupta, K. *et al.* Increasing Antimicrobial Resistance and the Management of Uncomplicated Community-Acquired Urinary Tract Infections. *Ann. Int. Med.* **135** (1), 41–50 (2001)
- Gupta, K. *et al.* International Clinical Practice Guidelines for the Treatment of Acute Uncomplicated Cystitis and Pyelonephritis in Women: A 2010 Update by the Infectious Diseases Society of America and the European Society for Microbiology and Infectious Diseases. *Clinical Infectious Diseases* **52**, e103–e120 (2011).
- Hagan, E. C., Lloyd, A. L., Rasko, D. A., Faerber, G. J. & Mobley, H. L. T. *Escherichia coli* Global Gene Expression in Urine from Women with Urinary Tract Infection. *PLoS Pathog* **6**, e1001187 (2010).
- Hannan, T. J. *et al.* Host-pathogen checkpoints and population bottlenecks in persistent and intracellular uropathogenic *Escherichia coli* bladder infection. *FEMS Microbiol Rev* **36**, 616–648 (2012).
- Hansen, S., Lewis, K. & Vulić, M. Role of Global Regulators and Nucleotide Metabolism in Antibiotic Tolerance in *Escherichia coli*. *AAC* **52**, 2718–2726 (2008).
- Harms, A., Maisonneuve, E. & Gerdes, K. Mechanisms of bacterial persistence during stress and antibiotic exposure. *Science* **354**, aaf4268 (2016).
- Harms, A., Fino, C., Sørensen, M. A., Semsey, S. & Gerdes, K. Prophages and Growth Dynamics Confound Experimental Results with Antibiotic-Tolerant Persister Cells. *mBio* **8**, e01964-17 (2017).
- Holden, N. J. & Gally, D. L. Switches, cross-talk and memory in *Escherichia coli* adherence. *Journal of Medical Microbiology* **53**, 585–593 (2004).

Hung, C.-S. *et al.* Structural basis of tropism of *Escherichia coli* to the bladder during urinary tract infection: FimH mannose-binding pocket. *Molecular Microbiology* **44**, 903–915 (2002).

Imamura, H. *et al.* Visualization of ATP levels inside single living cells with fluorescence resonance energy transfer-based genetically encoded indicators. *PNAS* **106**, 15651–15656 (2009).

Iosifidis, G. & Duggin, I. G. Distinct Morphological Fates of Uropathogenic *Escherichia coli* Intracellular Bacterial Communities: Dependency on Urine Composition and pH. *Infect Immun* **88**, (2020).

Ipe, D. S., Horton, E. & Ulett, G. C. The Basics of Bacteriuria: Strategies of Microbes for Persistence in Urine. *Front Cell Infect Microbiol* **6**, 14 (2016).

Jacob-Dubuisson, F. *et al.* PapD chaperone function in pilus biogenesis depends on oxidant and chaperone-like activities of DsbA. *Proceedings of the National Academy of Sciences* **91**, 11552–11556 (1994).

Johnson, J. R., Owens, K., Gajewski, A. & Kuskowski, M. A. Bacterial Characteristics in Relation to Clinical Source of *Escherichia coli* Isolates from Women with Acute Cystitis or Pyelonephritis and Uninfected Women. *J Clin Microbiol* **43**, 6064–6072 (2005).

Justice, S. S. *et al.* Differentiation and developmental pathways of uropathogenic *Escherichia coli* in urinary tract pathogenesis. *Proceedings of the National Academy of Sciences* **101**, 1333–1338 (2004).

Kalas, V. *et al.* Evolutionary fine-tuning of conformational ensembles in FimH during host-pathogen interactions. *Sci. Adv.* **3**, e1601944 (2017).

Kaper, J. B., Nataro, J. P. & Mobley, H. L. T. Pathogenic *Escherichia coli*. *Nat Rev Microbiol* **2**, 123–140 (2004).

Katchman, E. A. *et al.* Three-day vs longer duration of antibiotic treatment for cystitis in women: Systematic review and meta-analysis. *The American Journal of Medicine* **118**, 1196–1207 (2005).

- Khetrapal, V. *et al.* A set of powerful negative selection systems for unmodified *Enterobacteriaceae*. *Nucleic Acids Res* **43**, (2015).
- Klein, R. D. & Hultgren, S. J. Urinary tract infections: microbial pathogenesis, host–pathogen interactions and new treatment strategies. *Nat Rev Microbiol* **18**, 211–226 (2020).
- Kline, K. A., Fälker, S., Dahlberg, S., Normark, S. & Henriques-Normark, B. Bacterial Adhesins in Host-Microbe Interactions. *Cell Host & Microbe* **5**, 580–592 (2009).
- Lacerda Mariano, L. & Ingersoll, M. A. The immune response to infection in the bladder. *Nat Rev Urol* **17**, 439–458 (2020).
- Lambert, R. J. W. & Pearson, J. Susceptibility testing: accurate and reproducible minimum inhibitory concentration (MIC) and non-inhibitory concentration (NIC) values. *J Appl Microbiol* **88**, 784–790 (2000).
- Lane, M. C. Role of P-fimbrial-mediated adherence in pyelonephritis and persistence of uropathogenic *Escherichia coli* (UPEC) in the mammalian kidney. *Kidney International* **7** (2007).
- Lane, M. C. *et al.* Role of motility in the colonization of uropathogenic *Escherichia coli* in the urinary tract. *Infect. Immun.* **73**, 7644–7656 (2005).
- Lewis, A. J., Richards, A. C. & Mulvey, M. A. Invasion of Host Cells and Tissues by Uropathogenic Bacteria. *Microbiol Spectr* **4** (2016).
- Lewis, K. Persister Cells. *Annu. Rev. Microbiol.* **64**, 357–372 (2010).
- Lillington, J. Biogenesis and adhesion of type 1 and P pili. *Biochimica et Biophysica Acta* **11** (2014).
- Lloyd, A. L., Rasko, D. A. & Mobley, H. L. T. Defining Genomic Islands and Uropathogen-Specific Genes in Uropathogenic *Escherichia coli*. *J Bacteriol* **189**, 3532–3546 (2007).
- Lutz, R. Independent and tight regulation of transcriptional units in *Escherichia coli* via the LacR/O, the TetR/O and AraC/I1-I2 regulatory elements. *Nucleic Acids Research* **25**, 1203–1210 (1997).

Maerkl, S. J. Integration column: Microfluidic high-throughput screening. *Integr. Biol.* **1**, 19–29 (2009).

7.

Maglica, Ž., Özdemir, E. & McKinney, J. D. Single-Cell Tracking Reveals Antibiotic-Induced Changes in Mycobacterial Energy Metabolism. *mBio* **6**, e02236-14 (2015).

Martinez, J. J. Type 1 pilus-mediated bacterial invasion of bladder epithelial cells. *The EMBO Journal* **19**, 2803–2812 (2000).

Martínez-Figueroa, C. *et al.* Observation of intracellular bacterial communities in urinary sediment using brightfield microscopy; a case report. *BMC Urol* **20**, 89 (2020).

Mattiazzi Usaj, M. *et al.* High-Content Screening for Quantitative Cell Biology. *Trends in Cell Biology* **26**, 598–611 (2016).

Melamed, S. *et al.* A printed nanolitre-scale bacterial sensor array. *Lab Chip* **11**, 139–146 (2011).

Mempin, R. *et al.* Release of extracellular ATP by bacteria during growth. *BMC Microbiol* **13**, 301 (2013).

Mercier, R., Kawai, Y. & Errington, J. General principles for the formation and proliferation of a wall-free (L-form) state in bacteria. *eLife* **3**, e04629 (2014).

Michiels, J. E., Van den Bergh, B., Verstraeten, N. & Michiels, J. Molecular mechanisms and clinical implications of bacterial persistence. *Drug Resistance Updates* **29**, 76–89 (2016).

Mickiewicz, K. M. *et al.* Possible role of L-form switching in recurrent urinary tract infection. *Nat Commun* **10**, 1–9 (2019).

Mobley, H. L. *et al.* Pyelonephritogenic *Escherichia coli* and killing of cultured human renal proximal tubular epithelial cells: role of hemolysin in some strains. *Infection and Immunity* **58**, 1281–1289 (1990).

Molina-Quiroz, R. C., Lazinski, D. W., Camilli, A. & Levy, S. B. Transposon-Sequencing Analysis Unveils Novel Genes Involved in the Generation of Persister Cells in Uropathogenic *Escherichia coli*. *Antimicrob. Agents Chemother.* **60**, 6907–6910 (2016).

- Monteiro, R. *et al.* Differential biotin labelling of the cell envelope proteins in lipopolysaccharidic diderm bacteria: Exploring the proteosurfaceome of *Escherichia coli* using sulfo-NHS-SS-biotin and sulfo-NHS-PEG4-bismannose-SS-biotin. *Journal of Proteomics* **181**, 16–23 (2018).
- Mulvey, M. A. *et al.* Induction and Evasion of Host Defenses by Type 1-Piliated Uropathogenic *Escherichia coli*. *Science* **282**, 1494–1497 (1998).
- Mundt, L. A., Shanahan, K. and Graff, L., Graff's Textbook of Urinalysis and Body Fluids. Third edition. Philadelphia: Wolters Kluwer/Lippincott Williams & Wilkins Health (2016).
- Murray, B. O. *et al.* Recurrent Urinary Tract Infection: A Mystery in Search of Better Model Systems. *Front. Cell. Infect. Microbiol.* **11**, 691210 (2021).
- Mysorekar, I. U. & Hultgren, S. J. Mechanisms of uropathogenic *Escherichia coli* persistence and eradication from the urinary tract. *Proceedings of the National Academy of Sciences* **103**, 14170–14175 (2006).
- Neumann, B. *et al.* Phenotypic profiling of the human genome by time-lapse microscopy reveals cell division genes. *Nature* **464**, 721–727 (2010).
- Nicolle, L. E. Uncomplicated Urinary Tract Infection in Adults Including Uncomplicated Pyelonephritis. *Urologic Clinics of North America* **35**, 1–12 (2008).
- Orman, M. A. & Brynildsen, M. P. Inhibition of stationary phase respiration impairs persister formation in *E. coli*. *Nat Commun* **6**, 7983 (2015).
- Pak, J., Pu, Y., Zhang, Z.-T., Hasty, D. L. & Wu, X.-R. Tamm-Horsfall Protein Binds to Type 1 Fimbriated *Escherichia coli* and Prevents *E. coli* from Binding to Uroplakin Ia and Ib Receptors. *Journal of Biological Chemistry* **276**, 9924–9930 (2001).
- Pizarro-Cerdá, J. & Cossart, P. Bacterial Adhesion and Entry into Host Cells. *Cell* **124**, 715–727 (2006).
- Rappsilber, J., Mann, M. & Ishihama, Y. Protocol for micro-purification, enrichment, pre-fractionation and storage of peptides for proteomics using StageTips. *Nat Protoc* **2**, 1896–1906 (2007).



- Roberts, J. A. *et al.* The Gal(al-4)Gal-specific tip adhesin of *Escherichia coli* P-fimbriae is needed for pyelonephritis to occur in the normal urinary tract. *Proc. Natl. Acad. Sci. USA* **5** (1994).
- Robino, L. *et al.* Intracellular Bacteria in the Pathogenesis of *Escherichia coli* Urinary Tract Infection in Children. *Clinical Infectious Diseases* **59**, e158–e164 (2014).
- Ronneau, S. & Helaine, S. Clarifying the Link between Toxin–Antitoxin Modules and Bacterial Persistence. *Journal of Molecular Biology* S0022283619301500 (2019)
- Rosen, D. A., Hooton, T. M., Stamm, W. E., Humphrey, P. A. & Hultgren, S. J. Detection of Intracellular Bacterial Communities in Human Urinary Tract Infection. *PLoS Med* **4**, e329 (2007).
- Sarshar, M. *et al.* FimH and Anti-Adhesive Therapeutics: A Disarming Strategy Against Uropathogens. *Antibiotics* **9**, 397 (2020).
- Sauer, M. M. *et al.* Catch-bond mechanism of the bacterial adhesin FimH. *Nat Commun* **7**, 10738 (2016).
- Scholes, D. *et al.* Risk Factors Associated with Acute Pyelonephritis in Healthy Women. *Ann Intern Med* **142**, 20–27 (2005)
- Schwartz, D. J., Chen, S. L., Hultgren, S. J. & Seed, P. C. Population Dynamics and Niche Distribution of Uropathogenic *Escherichia coli* during Acute and Chronic Urinary Tract Infection. *Infect Immun* **79**, 4250–4259 (2011).
- Sharma, K. *et al.* Early invasion of the bladder wall by solitary bacteria protects UPEC from antibiotics and neutrophil swarms in an organoid model. *Cell Reports* **36**, 109351 (2021).
- Sharma, K. *et al.* Dynamic persistence of UPEC intracellular bacterial communities in a human bladder-chip model of urinary tract infection. *eLife* **10**, e66481 (2021).
- Silver, L. L. Fosfomycin: Mechanism and Resistance. *Cold Spring Harb Perspect Med* **7**, a025262 (2017).

- Simmering, J. E., Tang, F., Cavanaugh, J. E., Polgreen, L. A. & Polgreen, P. M. The Increase in Hospitalizations for Urinary Tract Infections and the Associated Costs in the United States, 1998–2011. *Open Forum Infectious Diseases* **4** (2017).
- Simpson, B. W. & Trent, M. S. Pushing the envelope: LPS modifications and their consequences. *Nat Rev Microbiol* **17**, 403–416 (2019).
- Snyder, J. A. *et al.* Transcriptome of Uropathogenic *Escherichia coli* during Urinary Tract Infection. *Infect Immun* **72**, 9 (2004).
- Spaulding, C. N. *et al.* Selective depletion of uropathogenic *E. coli* from the gut by a FimH antagonist. *Nature* **546**, 528–532 (2017).
- Spoering, A. L., Vulic, M. & Lewis, K. GlpD and PlsB Participate in Persister Cell Formation in *Escherichia coli*. *Journal of Bacteriology* **188**, 5136–5144 (2006).
- Spurbeck, R. R. *et al.* Fimbrial Profiles Predict Virulence of Uropathogenic *Escherichia coli* Strains: Contribution of Ygi and Yad Fimbriae. *Infect. Immun.* **79**, 4753–4763 (2011).
- Subashchandrabose, S. *et al.* Host-specific induction of *Escherichia coli* fitness genes during human urinary tract infection. *Proc Natl Acad Sci USA* **111**, 18327–18332 (2014).
- Tang, L. & Lee, N. Y. A facile route for irreversible bonding of plastic-PDMS hybrid microdevices at room temperature. *Lab Chip* **10**, 1274–1280 (2010).
- Terlizzi, M. E., Gribaudo, G. & Maffei, M. E. UroPathogenic *Escherichia coli* (UPEC) Infections: Virulence Factors, Bladder Responses, Antibiotic, and Non-antibiotic Antimicrobial Strategies. *Front. Microbiol.* **8**, 1566 (2017).
- Thanassi, D. G., Bliska, J. B. & Christie, P. J. Surface organelles assembled by secretion systems of Gram-negative bacteria: diversity in structure and function. *FEMS Microbiol Rev* **36**, 1046–1082 (2012).
- Thomas, W. E., Trintchina, E., Forero, M., Vogel, V. & Sokurenko, E. V. Bacterial Adhesion to Target Cells Enhanced by Shear Force. *Cell* **109**, 913–923 (2002).

- Thumbikat, P. *et al.* Bacteria-Induced Uroplakin Signaling Mediates Bladder Response to Infection. *PLoS Pathog* **5**, e1000415 (2009).
- Totsika, M., Beatson, S. A., Holden, N. & Gally, D. L. Regulatory interplay between pap operons in uropathogenic *Escherichia coli*. *Mol Microbiol* **67**, 996–1011 (2008).
- Tyanova, S. *et al.* The Perseus computational platform for comprehensive analysis of (prote)omics data. *Nat Methods* **13**, 731–740 (2016).
- Unger, M. A. Monolithic Microfabricated Valves and Pumps by Multilayer Soft Lithography. *Science* **288**, 113–116 (2000).
- van der Woude, M. W. & Bäuml, A. J. Phase and Antigenic Variation in Bacteria. *Clin Microbiol Rev* **17**, 581–611 (2004).
- van Melder, L. Toxin–antitoxin systems: why so many, what for? *Current Opinion in Microbiology* **13**, 781–785 (2010).
- Verderosa, A. D. *et al.* A high-throughput cell-based assay pipeline for the preclinical development of bacterial DsbA inhibitors as antivirulence therapeutics. *Sci Rep* **11**, 1569 (2021).
- Verpoorte, A. A Microfluidic Platform Enables Large-Scale Single-Cell Screening to Identify Genes Involved in Bacterial Persistence. *EPFL Infoscience* (2017)
- Verstraeten, N. *et al.* Opg and Membrane Depolarization Are Part of a Microbial Bet-Hedging Strategy that Leads to Antibiotic Tolerance. *Molecular Cell* **59**, 9–21 (2015).
- Vejborg, R. M., Hancock, V., Schembri, M. A. & Klemm, P. Comparative Genomics of *Escherichia coli* Strains Causing Urinary Tract Infections. *Appl Environ Microbiol* **77**, 3268–3278 (2011).
- Virkola, R. *et al.* Binding characteristics of *Escherichia coli* adhesins in human urinary bladder. *Infect Immun* **56**, 2615–2622 (1988).
- Waksman, G. & Hultgren, S. J. Structural biology of the chaperone–usher pathway of pilus biogenesis. *Nat Rev Microbiol* **7**, 765–774 (2009).

- Weiss, G. L. *et al.* Architecture and function of human uromodulin filaments in urinary tract infections. *Science* **369**, 1005–1010 (2020).
- Welch, R. A. *et al.* Extensive mosaic structure revealed by the complete genome sequence of uropathogenic *Escherichia coli*. *Proc. Natl. Acad. Sci. U.S.A.* **99**, 17020–17024 (2002).
- Wiles, T. J. *et al.* A phyletically rare gene promotes the niche-specific fitness of an *E. coli* pathogen during bacteremia. *PLoS Pathog.* **9**, e1003175 (2013).
- Wiles, T. J., Kulesus, R. R. & Mulvey, M. A. Origins and virulence mechanisms of uropathogenic *Escherichia coli*. *Experimental and Molecular Pathology* **85**, 11–19 (2008).
- Windels, E. M. *et al.* Bacterial persistence promotes the evolution of antibiotic resistance by increasing survival and mutation rates. *ISME J* **13**, 1239–1251 (2019).
- Wright, K. J., Seed, P. C. & Hultgren, S. J. Development of intracellular bacterial communities of uropathogenic *Escherichia coli* depends on type 1 pili. *Cellular Microbiology* **9**, 2230–2241 (2007).
- Wu, X.-R. In vitro binding of type 1-fimbriated *Escherichia coli* to uroplakins Ia and Ib: Relation to urinary tract infections. *Cell Biology* **6** (1996).
- Wurpel, D. J., Beatson, S. A., Totsika, M., Petty, N. K. & Schembri, M. A. Chaperone-Usher Fimbriae of *Escherichia coli*. *PLoS ONE* **8**, e52835 (2013).
- Wurpel, D. J. *et al.* F9 Fimbriae of Uropathogenic *Escherichia coli* Are Expressed at Low Temperature and Recognise Gal $\beta$ 1-3GlcNAc-Containing Glycans. *PLoS ONE* **9**, e93177 (2014).
- Yakovenko, O. *et al.* FimH Forms Catch Bonds That Are Enhanced by Mechanical Force Due to Allosteric Regulation. *Journal of Biological Chemistry* **283**, 11596–11605 (2008).
- Yethon, J. A., Vinogradov, E., Perry, M. B. & Whitfield, C. Mutation of the Lipopolysaccharide Core Glycosyltransferase Encoded by *waaG* Destabilizes the Outer Membrane of *Escherichia coli* by Interfering with Core Phosphorylation. *J Bacteriol* **182**, 5620–5623 (2000).

Zhou, G. *et al.* Uroplakin Ia is the urothelial receptor for uropathogenic *Escherichia coli*: evidence from in vitro FimH binding. *Journal of Cell Science* **114**, 4095–4103 (2001).

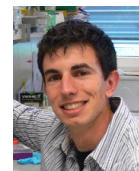
Zilsel, J., Ma, P. H. & Beatty, J. T. Derivation of a mathematical expression useful for the construction of complete genomic libraries. *Gene* **120**, 89–92 (1992).

## 7. Curriculum vitae

### Thomas M. Simonet

Address: Chemin du Chasseron 4, 1004 Lausanne  
Phone: +41 78 612 13 70  
Email: [thms.simonet@gmail.com](mailto:thms.simonet@gmail.com)

Born July 16, 1991  
French citizenship  
Swiss C permit



### Education

- 2016-2022 **PhD in Biotechnology and Bioengineering, Laboratory of Microbiology and Microtechnology, Global Health Institute, Swiss Federal Institute of Technology in Lausanne (EPFL)**
- Thesis advisor: Prof. John McKinney
  - Thesis title: Identification of genes required for host-cell adhesion and antibiotic persistence of uropathogenic *Escherichia coli* (UPEC) via high-content screening
- 2013-2015 **MSc in Life Sciences and Technologies, Swiss Federal Institute of Technology in Lausanne (EPFL), awarded with a Mention of Excellence**
- Specialization in Molecular Medicine
  - Best grade point average in the MSc program: 5.81/6
  - Master thesis conducted in the Swedish Medical Nanoscience Center at the Karolinska Institute (Stockholm, Sweden) under the supervision of Prof. Agneta Richter-Dahlfors
  - Thesis title: Development of a biomimetic *in vitro* model to study host-pathogen interactions in the context of pyelonephritis
- 2010-2013 **Advanced Master in Science and Technology, Higher Educational School of Industrial Physics and Chemistry of the City of Paris (ESPCI ParisTech, France)**
- Specialization in Chemistry/Biochemistry
  - Best grade point average among the students specialized in Chemistry/Biochemistry: 15.03/20
  - Research project conducted in the Laboratory of Biochemistry at ESPCI under the supervision of Prof. Andrew Griffiths
  - Project title: Reagentless fluorescent biosensors for protein quantitation in microfluidic droplets
- 2008-2010 **University-level preparation** in maths, physics and chemistry for the competitive admission exams to the French “Grandes Écoles” at **Lycée Kléber (Strasbourg, France)**

### Scientific background

- Technical skills    **Microbiology/Infection biology:** bacterial culture, minimum inhibitory concentration (MIC) assays, time-kill curves, mammalian cell culture, infection assays, immunostaining, working in a BSL (Bio Safety Level) 2 environment
- Microscopy:** fluorescence microscopy, time-lapse microscopy, high-content microscopy screening
- Microfabrication/Microfluidics:** soft lithography, multi-layered PDMS device fabrication, droplet microfluidics, live-cell imaging using microfluidics
- Molecular biology:** transposon mutagenesis, standard cloning, recombineering, primer design, PCR, gDNA and RNA extraction, RT-qPCR, protein purification

Computing	MS Office, Prism, AutoCAD, ImageJ, Matlab, Snapgene
Teaching	<b>Exercise sessions in general and organic chemistry</b> , first year Bachelor in Life Sciences <b>Practical sessions in molecular biology</b> , second year Bachelor in Life Sciences <b>Exercise sessions in microbiology</b> , third year Bachelor in Life Sciences
Projects	<b>Member of the 2014 EPFL iGEM (international Genetically Engineered Machines) team</b> → awarded a gold medal at the final competition in Boston

## Conference contributions and Publications

Poster presentations	<b>High-throughput microscopy for systems biology course</b> , Heidelberg, Germany, 2016 <b>NanoBioTech conference</b> , Montreux, Switzerland, 2016 <b>New approaches and concepts in microbiology</b> , Heidelberg, Germany, 2017 <b>Challenges and new concepts in antibiotic research</b> , Paris, France, 2018 <b>Bacterial persistence and antimicrobial therapy</b> , Ascona, Switzerland, 2018 <b>20<sup>th</sup> EMBL PhD symposium</b> , Heidelberg, Germany, 2018 <b>Annual congress of the Swiss Society for Microbiology</b> , Zürich, Switzerland, 2019 <b>Annual congress of the Swiss Society for Microbiology</b> , online event, 2021 → awarded the 3 <sup>rd</sup> prize for best poster presentation
Oral presentations	<b>Annual retreat of the Global Health Institute of EPFL</b> , Zermatt, Switzerland, 2018 <b>Annual meeting of the LS2 Society</b> , Zürich, Switzerland, 2020
Publications	<b>The outer membrane of uropathogenic <i>Escherichia coli</i> plays a crucial role for survival to treatment with the cell wall synthesis inhibitor fosfomycin</b> , Simonet TM, Normandeau F, Rossier A, Dhar N, McKinney JD. <i>Manuscript in preparation</i> .  <b>High-content screening identifies a critical role for P pili in early adhesion of uropathogenic <i>Escherichia coli</i> to bladder cells</b> , Simonet TM, Rutschmann O, Sharma K, Nass T, Pavlou MP, Dubois A, Knott GW, McKinney JD. <i>Manuscript in preparation</i> .  <b>Dynamic persistence of uropathogenic <i>Escherichia coli</i> intracellular bacterial communities in a human bladder-chip model of urinary tract infection</b> , Sharma K, Dhar N, Thacker VV, Simonet TM, Signorino-Gelo F, Knott GW, McKinney JD, eLife. 2021 Jul 5;10:e66481.

## Language skills

English	Fluent (C2)
German	Professional working proficiency (C1)
Spanish	Fair working knowledge (B1)

## Extracurricular activities

Music	25 years of practice of violin and viola in amateur orchestras and string quartets, with regular playing at concerts and events, such as the EPFL Master diploma ceremonies in 2018, 2019 and 2021
Sports	Swimming in a club for 15 years, running, biking, skiing
Projects	- Treasurer of the Culture Club at ESPCI ParisTech, in charge of negotiating tickets for cultural events in Paris at an affordable price for the student community - Member of the boards of two student orchestras in Lausanne, in charge of establishing the musical programs and organizing the concerts - Voluntary teaching in English to 10-year old kids in Peru

Vrillés par le vacarme, tes tympanes s'estompent  
Imposent le calme, qu'aucun ennui ne trompe  
Concentré, décidé, tu refais tous tes gestes  
Taisant tes pensées pour que seule l'envie reste  
Où étais-tu passé dans les moments de doute ?  
Inquiet puis terrifié, tu sais ce qu'il en coûte  
Réussir est entier quand la lutte est écrite  
Endosse ta fierté car, oui, tu la mérites !

Beethoven, *Eroica*, *Finale*

Andrés Orozco-Estrada